Contents

1 Introduction **1**
  1.1 Correlated systems: minimal models 1
  1.2 Methodology 3
    1.2.1 The adiabatic limit 4
    1.2.2 Monte Carlo methods 4
    1.2.3 Transport theory 5
  1.3 Thesis problems 5
    1.3.1 Double exchange models 5
    1.3.2 Metal-insulator transitions 6
    1.3.3 Disordered magnets 6
    1.3.4 Phase coexistence 6
  1.4 Further work 6

2 Electronic Transport with Structural and Magnetic Disorder **9**
  2.1 Introduction 9
  2.2 Computational scheme 11
    2.2.1 The spin distribution 11
    2.2.2 Conductivity calculation 12
  2.3 Transport in the Anderson model 14
    2.3.1 Global features 14
    2.3.2 Transport regimes 16
    2.3.3 Optical conductivity 18
    2.3.4 Large L extrapolation 19
    2.3.5 Effect of the transverse dimension 21
  2.4 Scattering from magnetic disorder 21
    2.4.1 Global features 21
    2.4.2 Transport regimes 23
    2.4.3 Optical conductivity 25
  2.5 Combined structural and magnetic disorder 26
    2.5.1 Global features 26
    2.5.2 Transport Regimes 28
  2.6 Concluding remarks 33

3 Effective Spin Hamiltonian for Double Exchange Models **37**
  3.1 Introduction 37
    3.1.1 Theoretical approaches 39
  3.2 Method 41
    3.2.1 The $J_H/t \to \infty$ limit 41

3.2.2 Effective Hamiltonian for spins . . . 42
3.2.3 Analytic limits . . . 43
3.2.4 Monte Carlo implementation . . . 44
3.2.5 Physical properties at equilibrium . . . 45
3.3 Results . . . 45
3.3.1 Magnetism and thermodynamics . . . 46
3.3.2 Density of states . . . 49
3.3.3 Optical properties . . . 49
3.3.4 Resistivity . . . 49
3.4 Conclusion . . . 52

4 Anderson-Mott Transition in a-GdSi **55**
4.1 Introduction . . . 55
4.2 Experiments on a-GdSi . . . 57
4.2.1 Conductivity: . . . 57
4.2.2 Tunneling DOS: . . . 59
4.2.3 Specific heat: . . . 59
4.2.4 Magnetism: . . . 61
4.2.5 Optical response . . . 61
4.2.6 Summary . . . 61
4.3 Model for a-GdSi . . . 63
4.4 Method . . . 64
4.4.1 The magnetic problem . . . 64
4.4.2 Handling the phonons . . . 65
4.4.3 Transport . . . 66
4.5 Results . . . 66
4.5.1 Spin glass phase . . . 66
4.5.2 Insulator-metal transition . . . 66
4.5.3 Spectral features . . . 69
4.5.4 Magneto-optical Response . . . 69
4.6 Coulomb effects . . . 69
4.7 Concluding remarks . . . 69

5 Disordered Double Exchange Magnets **73**
5.1 Introduction . . . 73
5.1.1 Earlier work . . . 74
5.2 Model and Method . . . 75
5.2.1 Effective Hamiltonian for spins . . . 75
5.2.2 Monte Carlo implementation . . . 76
5.3 Results . . . 77
5.3.1 Benchmarking H_{eff} against ED-MC . . . 77
5.3.2 Phase diagram . . . 78
5.3.3 Magnetism . . . 80
5.3.4 Spatial inhomogeneity . . . 80
5.3.5 Transport and metal-insulator transitions . . . 81
5.3.6 Optical response . . . 83
5.4 Conclusions . . . 84

6 Nanoscale Phase Coexistence 87
- 6.1 Introduction 87
  - 6.1.1 Scenario 88
  - 6.1.2 Microscopic approach 89
- 6.2 Model and method 89
- 6.3 Benchmarking H_{eff} against ED-MC 90
- 6.4 Results at zero field 92
  - 6.4.1 Spatial structures and cluster size 92
  - 6.4.2 Magnetic properties 94
  - 6.4.3 Spectral features 94
  - 6.4.4 Results on Transport 96
- 6.5 Response to a magnetic field 98
  - 6.5.1 Effect on spatial structures 99
  - 6.5.2 Magnetism and transport 99
- 6.6 Connection with manganites 101
- 6.7 Conclusions 101

7 Thesis Summary 105

Chapter 1

Introduction

Chapter Summary: This chapter serves as the introduction to the thesis, and also to the overall problem of electrons strongly coupled to classical degrees of freedom. First we quickly touch upon the correlated electron problems that emerge from materials physics and outline the difficulty in solving them accurately. We then indicate how the 'adiabatic' approach, viewing some of these problems in terms of electrons coupled to annealed classical degrees of freedom, allows some advance. We motivate our key innovation, within the adiabatic framework, that allows us to provide detailed solutions to a family of double exchange based magnetic models. Following this we briefly introduce the problems studied in this thesis. We end with a discussion of how the adiabatic approach can be extended to handle phonons and orbital degrees of freedom.

1.1 Correlated systems: minimal models

The study of electron correlations define a frontier in condensed matter physics and encompasses materials like high T_c superconductors, heavy fermions, the manganites, and the two dimensional electron gas. The underlying models involve electrons directly interacting via Coulomb (or Hubbard) interactions, or coupled to local moments via Kondo coupling, or to phonon degrees of freedom (as in the Holstein model). The strong coupling many body problems that arise in these models are rarely 'exactly solvable', except possibly in one dimension, and are beyond the reach of standard perturbative techniques. The tools to handle such systems include finite size numerical techniques like exact diagonalisation or quantum Mote Carlo, or methods like dynamical mean field theory. The presence of strong correlations itself presents a formidable problem, and disorder, which often has a non trivial effects in a correlated system, further complicates it. Let us take a look at some models where correlations and disorder are both relevant. Each of the following models, and areas of phenomenology, have a vast literature, and we provide only the briefest introduction to these subjects.

Hubbard model

The 'clean' version of this model was proposed originally for studying band ferromagnetism (as in Fe). The recent focus is more on the Mott transition in the model, and the properties of doped Mott insulators, because of its possible relevance to the high T_c materials.

$$H = -t \sum_{\langle ij \rangle, \sigma} c^{\dagger}_{i\sigma} c_{j\sigma} + \sum_{i} \epsilon_i n_i + U \sum_{i} n_{i\uparrow} n_{i\downarrow}$$

If $\langle \epsilon_i^2 \rangle = \Delta^2$, then depending on Δ/t, U/t and electron density (n) a variety of phenomena can arise. In the clean limit there can be various magnetic phases, a Mott insulating phase at strong coupling and half-filling, and (possibly) non Fermi liquid signatures in the doped Mott insulator. The interplay of disorder with correlation effects is not well understood, and leads to the area of "Anderson-Mott" phenomena, where interactions and disorder mutually enhance the tendency towards electron localisation. Despite intensive work on the Hubbard model over the last four decades there is no consensus on the detailed phase diagram, or the nature of the metallic phase at strong coupling.

Kondo lattice

This model serves as the starting point for heavy fermion physics, and involves localised (f) electrons coupled to itinerant $s-p-d$ electrons. The physical effects involve the interplay of Kondo quenching of the local moments, tending to generate a non magnetic 'heavy fermion' liquid, and conduction electron mediated RKKY interaction between local moments which prefers a magnetically ordered state.

$$H = -t \sum_{\langle ij \rangle, \sigma} c^{\dagger}_{i\sigma} c_{j\sigma} + \sum_i \epsilon_i n_i + J \sum_i \mathbf{S}_i . \vec{\sigma}_i$$

In the clean limit there is a competetion between the Kondo effect, and the RKKY magnetism. Tuning this competetion, for example by pressure or a magnetic field, can lead to a quantum critical point (QCP) and associated non Fermi liquid (NFL) behaviour. There are also many instances of an unconventional superconducting state at low temperature.

The presence of disorder in these systems can generate NFL behaviour even away from the QCP, presumably because a fraction of the local moments 'survive' to low temperature and lead to anomalous fluctuations.

Holstein model

The coupling of electrons to phonon degrees of freedom is the origin of pairing in the 'traditional' superconductors. At commensurate fillings, electron-phonon pairing can also lead to charge order/charge density waves (CDW). The most dramatic strong coupling effect, however, is the polaronic instability (or self trapping). In that case the presence of an electron at a site creates a large lattice distortion, trapping the electron, which self-consistently sustains the distortion.

$$H = -t \sum_{\langle ij \rangle, \sigma} c^{\dagger}_{i\sigma} c_{j\sigma} + \sum_i \epsilon_i n_i - \lambda \sum_i n_i x_i + \frac{1}{2M} \sum_i p_i^2 + \frac{K}{2} \sum_i x_i^2$$

For "quantum" phonons, with $\omega_{ph} = \sqrt{K/M}$, the last three terms in H can be written as: $-\lambda_Q \sum_i n_i (b_i^{\dagger} + b_i) + \omega_{ph} \sum_i b_i^{\dagger} b_i$, using $x_i = (b_i + b_i^{\dagger})/\sqrt{2M\omega_{ph}}$, and $\lambda_Q = \lambda \sqrt{\omega_{ph}/(2K)}$. At finite ω_{ph} and strong coupling the electrons do not remain spatially localised but form a narrow band polaronic 'metal' with large effective mass. In the adiabatic, $\omega_{ph} = 0$, case, however, the particles are indeed spatially localised, leading to an insulating phase. Disorder in these systems strongly enhances the localising tendency, and also disrupts the charge order (by acting like a random field).

Two dimensional electron gas

The two dimensional electron gas (2DEG) is a vital problem involving the interplay of disorder and electron-electron interactions, in particular because disorder has a singular effect in two dimension (leading to the absence of a metallic state) while some recent experiments indicate that interaction effects can actually lead to a metallic regime. The model for such a system, in the continuum limit, is:

$$H = \sum_{\mathbf{k}\sigma} \frac{k^2}{2m} c^{\dagger}_{\mathbf{k}\sigma} c_{\mathbf{k}\sigma} + \int d\mathbf{r} V_{imp}(\mathbf{r})\hat{\rho}(\mathbf{r}) + \int d\mathbf{r} d\mathbf{r}' V_{coul}(\mathbf{r}-\mathbf{r}')\hat{\rho}(\mathbf{r})\hat{\rho}(\mathbf{r}')$$

V_{imp} is the disorder potential arising from impurities randomly located in the plane, V_{coul} is the two body coulomb interaction and $\hat{\rho}((\mathbf{r}) = \sum_i \delta(\mathbf{r} - \mathbf{r}_i)$. The phases in this model include the clean correlated electron liquid, an Wigner crystal, a Wigner glass, and, possibly, a disordered metallic phase.

Manganites

A minimal model for the manganites needs to involve strong electron-spin coupling as well as strong electron-phonon coupling, in addition to disorder. Such a model combines features of some of the problems described above.

$$H = -t \sum_{\langle ij \rangle \sigma} c^{\dagger}_{i\sigma} c_{j\sigma} + \sum_i (\epsilon_i - \mu) n_i - \lambda \sum_i n_i x_i - J_H \sum_i \mathbf{S}_i . \sigma_i + \frac{K}{2} \sum_i x_i^2 + \frac{1}{2M} \sum_i p_i^2$$

The phases in the model above include ferromagnetic metal, paramagnetic metal/insulator, as well as charge order. In the real materials the electron-phonon coupling is of the Jahn-Teller type, so there is an associated angular degree of freedom in the phonon distortion, and an associated orbital variable for the electrons. There are several metal-insulator transitions in the model above, driven by varying temperature, electron density, or couplings. There is the possibility of large magnetoresistance close to the ferromagnet to paramagnet transition. In addition, parts of the parameter regime involve cluster coexistence, arising from the interplay of competing ordering tendencies and the presence of disorder.

Summary

The problems above define the 'agenda' in correlated electron theory and the materials that they describe are at the focus of intense experimental study. While much insight has been gained from efforts over the last couple of decades, none of these problems can be considered to be 'solved'. The problems and models that we consider in the thesis are related to the models above but have a simplifying feature which makes them more tractable and allows us to study the interplay of interaction effects and disorder in a controlled manner.

1.2 Methodology

What are the tools to handle the problems that we listed out? All the problems above involve strong coupling and, sometimes, the presence of disorder, and are well beyond the perturbative regime. In the absence of analytical tools, or an inspired guess, the only recourse is to use numerical methods. A correlated lattice model can be 'solved' on a finite lattice by exact diagonalisation (ED), or simulated using quantum Monte Carlo (QMC) techniques. ED, although exact, is severely size limited due to the exponential growth of the Hilbert space with system size, while fermion QMC comes up against a 'sign problem' at low temperature. These methods provide a valuable benchmark for approximate methods but by themselves are rarely able to provide insight on the thermodynamic limit. New tools like density matrix renormalisation group [1] (DMRG) and dynamical mean field theory [2] (DMFT) have been developed over the last two decades to handle correlated systems, and have allowed significant advance. DMRG, however, is restricted mostly to one dimension, while DMFT formally takes the 'infinite dimension' limit mapping on a lattice model to a quantum impurity problem. Unfortunately, some physical effects which may be specific to two or three dimension, and also the presence of disorder, remain inaccessible within these schemes. This leaves room for an alternate, "real space", approach that we explore.

1.2.1 The adiabatic limit

Problems where the fermions are coupled to 'classical fields', *e.g*, large S spins, or 'adiabatic' phonons, are at an intermediate level of difficulty between purely classical systems and quantum many body problems. In such a situation the quantum degrees of freedom are not directly interacting, so the difficulty with an exponentially growing Hilbert space is absent, but "annealing" the classical variables is much more difficult compared to purely classical systems. We use this approach as our entry point into models of disordered correlated electrons.

This "adiabatic approximation", whereby some degrees of freedom are treated as classical, is not novel. Several problems have been solved in the past by making this approximation, *e.g*, in electron-phonon systems [3], or, in a different context, in the Car-Parrinello method [4], handling coupled electronic and ionic degrees of freedom. The recent interest lies in the application of this approach to several strong coupling lattice fermion models, and some degree of success in understanding complex materials. Millis and coworkers [5] studied electrons coupled to classical spin and lattice ('phonon') degrees of freedom, to construct an initial theory of the manganites using DMFT. The approach was taken much further by Dagotto and coworkers [6] using 'real space' Monte Carlo techniques to study ordering phenomena, phase coexistence, and disorder effects in a large family of correlation models pertinent to the manganites. The method has been used extensively also to explore magnetism in double exchange (DE) based models [7]. For diluted magnetic semiconductors (DMS) too, much of the physics has been clarified by methods which treat the doped magnetic moment as classical [8].

1.2.2 Monte Carlo methods

Although the adiabatic limit simplifies the many body problem by casting it in the form of "non interacting" fermions in the background of classical variables, $\{x\}$ say, determining the distribution $P\{x\}$ involves an expensive computation. In the absence of any small parameter to further simplify the problem, computing $P\{x\}$ requires iterative diagonalisation [6] of the fermion Hamiltonian and, for an N site system, the computation time, τ_N, increases as N^4. We will discuss the standard exact diagonalisation based Monte Carlo (ED-MC) in chapter 3, here we just note that the accessible sizes, $N \sim 100$, within ED-MC, severely limits the ability of the method to resolve the outstanding issues relating to transport, metal-insulator transitions, and the effect of disorder in correlated systems.

There have been some attempts at overcoming the severe finite size constraint in ED-MC. (i) Instead of exact diagonalisation, it has been proposed that the energy of fermions in the classical background can be estimated by moment expansion of the density of states [9, 10]. This, in principle, allows access to $N \gtrsim 10^3$, although there seems to have been no exploration of the method beyond the simple double exchange model. (ii) A 'hybrid' Monte Carlo method, using dynamical evolution of the classical variables, has been tried out [11] for a model of competing DE and superexchange, but no results have been reported beyond the magnetic phases.

This is where our method allows an advance. We have proposed a scheme [12], in the context of double exchange based models, where the energy associated with the spin configuration can be approximated by an *explicit* classical Hamiltonian with couplings determined from a solution of the fermion problem. This not only allows us to reasonably reproduce the "exact" results in the clean double exchange model, it goes far beyond, in handling strong disorder, as well as the problem of nanoscale phase coexistence - quite beyond the reach of "exact" methods.

1.2.3 Transport theory

Once the annealing problem is solved, and generates the relevant equilibrium classical configurations, the electronic response functions have to be computed by solving the Schrodinger equation in these backgrounds. The backgrounds are typically 'disordered', but unlike the canonical Anderson disorder problem, there are non trivial spatial correlations between the annealed variables. This implies that standard analytic methods of disorder average, employed in localisation studies, are not useful. We use the Kubo formula, including an extrapolation scheme described in chapter 2, to compute transport coefficients, and explicitly average over the annealed disorder configurations. Chapter 2 sets out the scheme in detail, and a short paper [13] provides some results of the method in the context of simple quenched disorder.

1.3 Thesis problems

The transport calculation method, chapter 2, and our Monte Carlo strategy, have been used to study the following problems in the thesis.

1.3.1 Double exchange models

While the Kondo lattice model (KLM) with antiferromagnetic coupling between conduction electrons and the (quantum) local moment is the starting point for heavy fermion physics, the ferromagnetic version, with large J/t, defines the double exchange (DE) model. The coupling arises from Hunds rule in real materials and is the origin of ferromagnetism in several transition metal oxides. If the Kondo effect is not relevant, as for a ferromagnetic coupling or a large S spin, the local moment can be treated as classical. Incorporating a possible direct AF superexchange, these systems can be modelled by:

$$H = -t \sum_{\langle ij \rangle, \sigma} c^{\dagger}_{i\sigma} c_{j\sigma} - J_H \sum_i \mathbf{S}_i . \vec{\sigma}_i + J_{AF} \sum_{\langle ij \rangle} \mathbf{S}_i . \mathbf{S}_j$$

It is usual to assume $J_H/t \to \infty$. The ferromagnetism in this model arises from the minimisation of the carrier kinetic energy in a fully spin polarised state. An estimate of the transition temperature, or transport properties, however, is non trivial since it involves the 'excited states' of the magnetic system, which do not have any translational order (and make the electron problem difficult to solve). In the presence of J_{AF} several new phases can arise depending on the AF coupling and electron density. Our basic strategy is discussed in detail in chapter 3, and also appears in the associated preprint [12].

1.3.2 Metal-insulator transitions

An amorphous system, with strong structural disorder enhanced by electron-phonon coupling. would have an insulator-metal transition with increasing carrier density, as the Fermi level moves past the mobility edge. If, additionally, there were magnetic degrees of freedom in the problem which freeze into a random (spin glass) state, the effective disorder seen by the electrons would be further enhanced, leading to stronger localisation. However, unlike structural disorder, spin disorder can be 'tuned' by an applied magnetic field, leading to a possible field driven insulator-metal transition.

Although such a possibility may seem artificial, recent experiments on amorphous a-GdSi demonstrate a magnetically tuned IMT in a strongly disordered electron system. We discuss this in chapter 4, and the related paper is [14].

1.3.3 Disordered magnets

The double exchange model incorporating the effect of structural disorder serves as the simplest model for studying the interplay of quenched and annealed disorder. In contrast the to clean DE model, the disordered model has a thermally driven metal-insulator transition, a coherent to incoherent crossover in its optical response, and also serves as a simple example of inhomogeneous 'freezing' into a magnetic state, chapter 5 and [15].

1.3.4 Phase coexistence

The presence of competing interactions can lead two a first order phase transition between two ordered phases, with the possibility of both the phases coexisting over a parameter regime. For electron systems this implies phase separation into regimes with different electron density and differing kinds of long range order (ferro and antiferro, say). In the presence of disorder the 'macroscopic' phase separation is converted to meso/nanoscale spatial coexistence of the two kinds of phases. If one of the phase is 'metallic' and the other 'insulating', then the coexistence phase would involve percolative transport. If, additionally, the phases respond to a magnetic field, then there is the possibility of large magnetoresistance. This is discussed in chapter 6 and [16].

1.4 Further work

While the adiabatic approach allows an entry point for a class of disordered interacting problems, and the Monte Carlo strategy devised by us allows detailed solution of double exchange based models, a number of theoretically interesting and experimentally relevant models still remain beyond reach. The most prominent example is that of phonon physics and lattice polarons (and its interplay with magnetism, as in the manganites). Our efforts to find an explicit classical Hamiltonian for these models was not successful. However, we could devise another strategy, essentially simplifying the fermion energy calculation during the Monte Carlo, and this forms the basis of a 'travelling cluster approximation' [17]. We have extensively explored this method in the recent past [18, 19, 20] but these problems are outside the scope of this thesis.

We feel that a combination of the strategies already developed by us with an approximate handling of non adiabatic corrections should make the presnt approach useful for a wide range of experimentally relevant systems.

Bibliography

[1] S. R. White, Phys. Rev. Lett. **69**, 2863 (1992), see Karen Hallberg, cond-mat 0303557, for a recent review.

[2] Antoine Georges, Gabriel Kotliar, Werner Krauth and Marcelo J. Rozenberg, Rev. Mod. Phys. **68**, 13 (1996). For recent reviews see, Tudor Stanescu and Gabriel Kotliar, cond-mat 0404722, Antoine Georges, cond-mat 0403123.

[3] A.B. Migdal, Sov. Phys. JETP **7**, 996 (1958), V.V. Kabanov and O.Y. Mashtakov, Phys. Rev. **B 47**, 6060 (1993).

[4] R. Car and M. Parrinello, Phys. Rev. Lett. **55**, 2471 (1985).

[5] A. J. Millis, B. I. Shraiman, and R. Mueller, Phys. Rev. Lett. **77**, 175 (1996).

[6] See *e.g*, S. Yunoki, *et al*, Phys. Rev. Lett. **80**, 845 (1998), S. Yunoki, T. Hotta, and E. Dagotto, Phys. Rev. Lett. **84**, 3714 (2000).

[7] M. J. Calderon and L. Brey, Phys. Rev. **B 58**, 3286 (1998), Y. Motome and N. Furukawa, J. Phys. Soc. Jpn. **68**, 3853 (1999).

[8] G. Alvarez, M. Mayr, and E. Dagotto, Phys. Rev. Lett. **89**, 277202 (2002).

[9] Yukitoshi Motome and Nobuo Furukawa, J. Phys. Soc. Jpn. **72**, 2126 (2003).

[10] Y. Motome and N. Furukawa, J. Phys. Chem. Solids, **63**, 1357 (2002).

[11] J. L. Alonso, *et al.*, Nucl.Phys. **B 596**, (2001) 587-610

[12] Sanjeev Kumar and Pinaki Majumdar, cond-mat 0305345.

[13] Sanjeev Kumar and Pinaki Majumdar, Europhys. Lett. **65**, 75 (2004)

[14] Pinaki Majumdar and Sanjeev Kumar, Phys. Rev. Lett. **90**, 237202 (2003)

[15] Sanjeev Kumar and Pinaki Majumdar, Phys. Rev. Lett. **91**, 246602-1 (2003)

[16] Sanjeev Kumar and Pinaki Majumdar, Phys. Rev. Lett. **92**, 126602 (2004)

[17] Sanjeev Kumar and Pinaki Majumdar, cond-mat 0406082.

[18] B. Poornachandra Sekhar, Sanjeev Kumar and Pinaki Majumdar, cond-mat 0406083.

[19] Sanjeev Kumar and Pinaki Majumdar, cond-mat 0406084.

[20] Sanjeev Kumar and Pinaki Majumdar, cond-mat 0406085.

Chapter 2

Electronic Transport with Structural and Magnetic Disorder

Chapter Summary: In this chapter we establish our basic transport calculation methodology. We employ the Kubo formula, based on the exact eigenfunctions and eigenvalues of the disordered electron problem, to compute the low frequency conductivity on the scale of the typical finite size gap in the problem. Systematic exploration of the size dependence of the response allows us to obtain the 'd. c. conductivity' by extrapolation. We try out the method on (i) the standard 'Anderson disorder' problem, to benchmark our method, and then map out the transport regimes and metal-insulator transitions in (ii) a model of magnetic scattering and (iii) the combined effect of structural and magnetic disorder. The method developed in this chapter is used in all the following chapters when considering electron motion in the presence of quenched or annealed disorder. Some of the results in this chapter have been published in Europhys. Lett. **65**, 75 (2004).

2.1 Introduction

The most commonly studied case of localisation pertains to non interacting electrons in the background of structural disorder. There is a large body of work [1, 2, 3, 4], analytical and numerical, as well as experimental studies, that have focused on this problem. The principal qualitative result of these investigations is that in one and two dimension all electronic eigenstates are localised for arbitrarily weak disorder, while in three dimension we need a critical disorder for complete localisation. In three dimension, at a given disorder, all states *beyond* an energy ϵ_c of the band center are localised and the system is metallic or insulating depending on whether the Fermi level, ϵ_F, lies in the region of extended states or localised states. The 'mobility edge', ϵ_c, collapses to the band center as the disorder is increased, driving the Anderson metal-insulator transition (MIT).

The presence of magnetic moments in a metal brings in several new effects, depending on the strength of electron-spin coupling (J'), the concentration of moments (n_{mag}), the extent of disorder, and the 'character' (small or large S) of the moment.

In the 'quantum limit', $2S \sim 1$, and for antiferromagnetic coupling, the basic physics is contained in the Kondo effect. For $n_{mag} \ll 1$, the magnetic moments act as 'Kondo impurities' whose effects [5] are now well understood. For $n_{mag} \sim 1$, *i.e*, the concentrated Kondo limit, there can be various phases depending on electron-spin coupling and disorder. The ground state could be a non magnetic ‘heavy Fermi liquid’ [6], or a spin glass[7], or a magnetically ordered state [8]. The physics of these Kondo lattice, with quantum spins, is a vast area of research. In this chapter, however, we will avoid the issues of heavy fermion physics and focus instead on electron-spin systems involving “large S”, *i.e*, effectively ‘classical’ moments.

For classical moments also, the physical effects vary depending on n_{mag}, electron density, J' and the extent of disorder. A wide variety of magnetic systems [9, 10, 11, 12, 13, 14, 15, 16, 17] are described, to a first approximation, by electrons locally coupled to d or f moments, with $2S \gg 1$, and moving in a structurally disordered background. The magnetic ground state could be ferromagnetic, or a more complicated ordered state, or a spin glass. Transport often involves insulator-metal transitions and colossal magnetoresistance. The simplest Hamiltonian capturing these effects is:

$$H = -t \sum_{\langle ij \rangle, \sigma} c^{\dagger}_{i\sigma} c_{j\sigma} + \sum_{i\sigma} (\epsilon_i - \mu) n_{i\sigma} - J' \sum_{\nu} \sigma_{\nu}.\mathbf{S}_{\nu} \tag{2.1}$$

For simplicity we consider a one band tight binding model, with nearest neighbour hopping on a simple cubic lattice. The random on site potential, ϵ_i, is uniformly distributed between $\pm\Delta/2$. The sites $\mathbf{R}_\nu$ are a subset of the cubic lattice sites, $\mathbf{R}_i$, and correspond to the magnetic ‘dopant’ locations. Even with this simple model there are four dimensionless parameters in the problem. These are disorder Δ/t, magnetic coupling $J'S/t$, electron density n (controlled by μ), and the ‘density’ of moments n_{mag}. We will eventually study the $n_{mag} = 1$ case, but retain a more general structure right now. We absorb S in our magnetic coupling J', assuming $|\mathbf{S}_i| = 1$.

Real materials have band degeneracy and additional interactions but the basic physics of several currently interesting materials arise as limiting cases of the model above.

- The II-VI diluted magnetic semiconductor [9, 10, 11] (DMS) $Ga_{1-x}Mn_xAs$, exhibiting high ferromagnetic T_c, correspond to $n_{mag} \ll 1$, $J'/t \sim 1$, weak disorder, and low electron density, $n < n_{mag}$.
- The Eu based magnetic semiconductors [12, 13], EuB_6 etc, involve $n_{mag} = 1$, since every Eu atom has a moment, $J'/t \gg 1$, low carrier density, and possibly weak disorder.
- The ‘colossal magnetoresistance’ (CMR) manganites [14], specifically $La_{1-x}Sr_xMnO_3$, involve $n_{mag} = 1$, $J'/t \gg 1$, high electron density, and moderate ‘effective disorder’. To describe the more strongly resistive manganites, the Ca doped systems, say, one requires additional electron-phonon interactions.
- The amorphous magnetic semiconductor [15, 16], a-Gd_xSi_{1-x}, corresponds to $J'/t \gg 1$, $\Delta/t \gg 1$, and $n_{mag} \sim n \sim \mathcal{O}(0.1)$.
- Finally, the traditional metallic f electron magnets [17], correspond to $n_{mag} = 1$, and moderate to strong J'.

The focus in the materials above is often on magnetism rather than localisation effects. However, many of them have rather large resistivity in the paramagnetic phase, and a-GdSi, for example, shows a metal-insulator transition at $T = 0$ itself, on lowering carrier density. Since there is no direct spin-spin interaction in these systems, *the local electron-spin coupling controls both the magnetic properties and the character of the electronic state.*

The intimate coupling between charge transport, localisation effects, and magnetism in these systems suggest that we need to look beyond the traditional boundaries separating 'magnetism' from transport and localisation studies. A complete study of electronic resistivity as a function of temperature, for any of the materials above, requires a solution of the magnetic problem first. Since the moments are assumed to be classical, the electrons can be imagined to move in a *static* background comprising the (quenched) structural disorder and *annealed* spin disorder. Evaluating the distribution of the annealed disorder is a non trivial problem, particularly in the strong coupling (large J') context that is experimentally relevant. We will touch upon this in the next section, but this chapter is concerned with transport and localisation effects in the fully spin disordered phase. In this limit, we will present a comprehensive discussion of the resistivity arising from the interplay of structural disorder and 'paramagnetic' scattering, and map out the metal-insulator phase diagram in terms of electron density, disorder and magnetic coupling.

There have been some studies of electronic transport in the background of random spins and structural disorder, acting independently or together. Among these, the Anderson localisation problem itself has been extensively studied, via perturbation theory [18], self-consistent schemes [19], numerical techniques [20], and mapping to a field theory [21]. Most of the qualitative issues in this context are essentially settled. *Weak* magnetic scattering in a structurally disordered system has been studied [22, 23] in the early days of weak localisation (WL) theory to clarify the 'dephasing' effect of electron spin flip on quantum interference. In the opposite limit of strong coupling, corresponding to double exchange, localisation effects have been studied [24] considering both magnetic and structural disorder.

These efforts still leave a large and interesting part of $\Delta - J'$ space unexplored. To give a few examples, there is no discussion of the following:

- the resistivity from purely magnetic scattering, as J' rises through the perturbative regime to double exchange: this is the classic problem of paramagnetic scattering in 'clean' magnets, studied earlier at weak coupling [25, 27].
- the effect of spin disorder on the Anderson transition, *i.e*, how the 'anti-localising' effect of spin flip scattering, at weak disorder, evolves into an insulator-metal transition (IMT). This is an instance of Anderson transition with broken time reversal symmetry, and
- the wide 'middle', where the effect of neither Δ nor J' is perturbative and their contribution to the resistivity is not additive (*i.e*, violates Mathiessens rule). This is the regime relevant to DMS, CMR materials, and amorphous magnetic semiconductors.

The next section describes the transport calculation in detail. Following that we present results on transport, successively, in the structural disorder problem, the magnetic disorder problem, and the simultaneous effect of both.

2.2 Computational scheme

Although we will work with random uncorrelated spins, viewing the magnetic disorder as quenched, let us highlight how the 'true' spin distribution can be evaluated, and the limit where the background can be considered random. Following that we describe our transport calculation method.

2.2.1 The spin distribution

The 'structural' variables ϵ_i are quenched, and have a specified distribution, but the spin orientations $\mathbf{S}_i$ are not known *a priori*. The system chooses a spin configuration, at $T = 0$, to optimise the total energy. To calculate the 'true' ground state properties, or finite temperature transport, we need to solve for the spin distribution first and then evaluate electronic properties in these spin background. Denoting the full spin configuration as $\{\mathbf{S}_i\}$, the spin distribution $P\{\mathbf{S}_i\}$ is given by:

$$\begin{aligned} P\{\mathbf{S}_i\} &= Z^{-1}\mathrm{Tr}e^{-\beta H} \\ Z &= \int \mathcal{D}\mathbf{S}_i \mathrm{Tr}e^{-\beta H} \end{aligned} \tag{2.2}$$

where Z is the full partition function of the system, and the 'trace' is over fermionic variables. Equivalently, the effective classical 'Hamiltonian' controlling the Boltzmann weight for spins is:

$$H_{eff}\{\mathbf{S}_i\} = -\frac{1}{\beta}\log \mathrm{Tr}e^{-\beta H} \tag{2.3}$$

H_{eff} is the fermion (free) energy F_{el} *in the background* $\{\mathbf{S}_i\}$.

To make more sense of the formal expression above, consider $J'/t \ll 1$. In this case we can expand the fermion (free) energy in powers of J'. For a non disordered system this leads to the standard RKKY coupling [27] between the classical spins, while the presence of structural disorder, leads to a 'bond disordered' RKKY model: $H_{eff} \sim \sum_{ij} J_{ij}\mathbf{S}_i.\mathbf{S}_j$, where the exchange J_{ij} are $\sim J'^2\chi_{ij}$ the χ_{ij} being the non local spin response function of the disordered, $J' = 0$, electron system. Having obtained the effective spin Hamiltonian, the transport properties are to be calculated by considering electron motion in the backgrounds $\{\epsilon_i, \mathbf{S}_i\}$ where the $\{\mathbf{S}_i\}$ are equilibrium configurations of H_{eff} for a specified realisation of disorder $\{\epsilon_i\}$.

At strong coupling, *i.e*, large J', the fermion trace cannot be analytically evaluated, and it is no longer possible to write an explicit spin Hamiltonian. We need special techniques to anneal the spins. The magnetic order and the complete transport properties in such (disordered) Kondo lattice models will be discussed in the following chapters.

Uncorrelated spins: The complications of the magnetic problem can be avoided if we *assume* a spin distribution. The simplest distribution one can assume corresponds to uncorrelated random spins. This is physically relevant in two limits.

(i) At sufficiently high temperature, compared to the magnetic ordering scales in the problem, the spins are essentially randomly fluctuating, with only short range correlation. The magnetic ordering scale for $J'/t \ll 1$ is $\sim f_1(n)J'^2/t$, while for $J'/t \gg 1$ the ordering scale is $\sim f_2(n)t$, where f_1 and f_2 are electron density dependent dimensionless coefficients and $f_2^{max} \sim 0.1$. Compared to the typical Fermi energy, $\sim zt$, where z is the coordination number of the lattice, these scales are all small. We use a $T = 0$ formulation for transport, *i.e*, we do not use Fermi factors, but given the smallness of T_c/ϵ_F, our results would be relevant even in the 'real' paramagnetic phase.

(ii) Another situation in which a random spin configuration is appropriate is a 'spin glass', likely to occur in strongly disordered systems [28]. There are always short range correlations in a spin glass but if we ignore their effect on transport then at all temperature the transport in such a system can be described, approximately, in terms of a random spin background.

2.2.2 Conductivity calculation

In the linear response regime, the Kubo formula can be used to calculate the conductivity of a system. The general expression [29], involving matrix elements between many body states, simplifies significantly for non-interacting systems. This 'Kubo-Greenwood' result can be computed purely in terms of single particle eigenfunctions and energies.

The numerical difficulty with this result lies in implementing it for a finite size system, where the spectrum is discrete, with gaps $\mathcal{O}(1/N)$, with N being the number of sites in the system. Since the 'd.c' conductivity involves transitions between essentially degenerate states at ϵ_F, it cannot be calculated with control on small systems. As a result, instead of computing the 'Kubo conductivity' it is more usual to compute the 'Landauer conductance', G, of a finite system coupled to leads [30], and infer the conductivity from the length dependence of G.

We pursue the Kubo approach, indirectly, through a calculation of the low frequency optical conductivity for a $L_T \times L_T \times L$ geometry. The advantage of calculating the conductivity this way is, (i) it ties in with diagonalisation that one may have to do for the magnetic problem, and (ii) it allows access to the optical conductivity, without added effort, and can reveal the significantly non Drude nature of $\sigma(\omega)$ at strong disorder. The principal disadvantage is, this scheme cannot be pushed beyond $N \sim 10^3 - 10^4$, in contrast to the Landauer approach, and is therefore not useful for accessing critical properties.

For disordered non interacting systems, the Kubo formula, at $T = 0$, is:

$$\sigma(\omega) = \frac{A}{N} \sum_{\alpha,\beta} (n_\alpha - n_\beta) \frac{|f_{\alpha\beta}|^2}{\epsilon_\beta - \epsilon_\alpha} \delta(\omega - (\epsilon_\beta - \epsilon_\alpha)) \tag{2.4}$$

with $A = \pi e^2/\hbar a_0$, a_0 being the lattice spacing, and $n_\alpha = \theta(\mu - \epsilon_\alpha)$. The $f_{\alpha\beta}$ are matrix elements of the current operator $j_x = it \sum_{i,\sigma}(c^\dagger_{i+xa_0,\sigma} c_{i,\sigma} - h.c)$, between exact single particle eigenstates $|\psi_\alpha\rangle$, $|\psi_\beta\rangle$ etc and ϵ_α, ϵ_β are the corresponding eigenvalues.

The conductivity above is prior to disorder averaging. Notice that the δ function constraint cannot be satisfied for arbitrary frequency in a finite system. So we can neither calculate the d.c conductivity, σ_{dc}, directly, nor estimate $\sigma(\omega)$ at some arbitrary externally specified frequency. However, we can still calculate the 'average' conductivity over a frequency interval $\Delta\omega$, defined below, and we use the following strategy to extract the d.c conductivity.

1. The average of $\sigma(\omega)$ over the interval $[0, \Delta\omega]$ is defined as

   $$\sigma_{av}(\Delta\omega, \mu, N) = \frac{1}{\Delta\omega} \int_0^{\Delta\omega} \sigma(\omega, \mu, N) d\omega \tag{2.5}$$

   $\Delta\omega$ can be set independent of N, but we will relate them by fixing: $\Delta\omega = B/N$. We fix B by setting $\Delta\omega = 0.04$ for $N = 1000$, in 3d. Notice, the mean finite size gap is $12/1000 \sim 0.01$ much smaller than $\Delta\omega$.

2. σ_{av} is averaged over N_r realisations of disorder, to generate $\bar{\sigma}_{av}(\Delta\omega, \mu, L)$. The 'noise' in $\bar{\sigma}_{av}(\Delta\omega, \mu, L)$ falls slowly, as $1/\sqrt{N_r}$. We use $N_r \sim 100$ for the largest sizes, to keep the computation reasonable, and use a filter to smooth the $\sigma(\mu, L)$ data over a small window $\delta\mu$ at each μ.

3. We study the $\bar{\sigma}_{av}(\Delta\omega, \mu, L)$ for $L_T = 6$ and the sequence $L = 24$ to $L = 64$ in increments of 8 and extrapolate:

   $$\sigma_{calc}(\mu) = \lim_{L\to\infty} \bar{\sigma}_{av}(\Delta\omega, \mu, L) \tag{2.6}$$

   As specified before, $\Delta\omega = B/N$. We calculate the conductivity in units of $(\pi e^2/\hbar a_0)$.

To calculate the full, disorder averaged, optical conductivity we use the inversion:

$$\sigma(\omega) = \bar{\sigma}_{av}(\omega) + \omega \frac{d\bar{\sigma}_{av}}{d\omega} \tag{2.7}$$

The $\sigma(\omega)$ results in this chapter are mostly based on a $6 \times 6 \times 32$ geometry.

2.3 Transport in the Anderson model

The metal-insulator phase boundary and the critical properties near the transition have been been extensively studied [18, 19, 20, 21] in the Anderson model. However, the actual resistivity seems to have received much less attention. As recently pointed out by Nikolic and Allen [31], there is a wide regime in Δ, between the Born-Boltzmann end and the scaling regime, where there are no analytic theories of transport. We study this 'old problem' in some detail because the wealth of existing results provides a benchmark for our method. There are very few exact results with which we will be able to compare our data in the magnetic scattering problems.

2.3.1 Global features

The 'global features' of transport and localisation in the Anderson model are contained in Figs.1-3. The data is obtained via the extrapolation procedure described earlier. Fig.1.(a) highlights the suppression in conductivity with increasing disorder, across the entire band. The 'weakest' disorder in this case, $\Delta = 4$, is probably already outside the semiclassical Boltzmann regime. A naive Δ^2 scaling of the resistivity still works, at the band center, between $\Delta = 4$ and $\Delta = 8$, but the same extrapolated to $\Delta = 16$, would imply $\rho(16)/\rho(4) \sim 16$, while the ratio is actually $\sim 10^3$. This figure captures the expected crossover from moderate scattering, roughly following Boltzmann scaling, to localisation as $\Delta \to \Delta_c \sim 16.5$, the critical disorder [32] at the band center. It also provides a glimpse of how the 'mobility edge' moves with increasing disorder, better quantified in Fig.3. Note that for data at a specified system size, $L = 16, 32$ etc, shown later, the notion of a 'mobility edge' does not make sense, and all we observe is a crossover from small to large conductivity as μ is varied. *The change in* $\sigma(\mu, L)$ *with* L*, and the* $L \to \infty$ *extrapolation, is crucial for identifying the mobility edge.*

The DOS plot, Fig.1.(b), illustrates the band broadening, and in Fig.3.(b) we have compared our band edge energy with earlier CPA results [33]. The (algebraic) average DOS is featureless and non critical and does not play an interesting role in the problem.

Since the band broadens significantly with disorder, $\sigma(\mu)$ by itself does not provide the *density* dependence of the conductivity. Fig.2 takes into account the shift in μ required to maintain constant density (with increasing disorder) and shows $\sigma(n)$. Our density is defined as average number of electrons per site, so $n_{max} = 2$. Since the model is particle-hole symmetric we show only the regime $n = [0, 1]$.

To get a feel for the magnitude of the conductivity, which we measure in units of $\pi e^2/(\hbar a_0)$, note that the Mott 'minimum metallic conductivity', σ_{Mott}, at the band center [4], is roughly $\sim 0.03 e^2/(\hbar a_0)$. Our dimensionless conductivity σ_{calc}, shown in the figures, can be converted to real units, σ_{actual}, by using

$$\sigma_{actual} \sim 100 * \sigma_{Mott} * \sigma_{calc}$$

where we use $\sigma_{Mott} = 0.03 e^2/(\hbar a_0)$. The results we show in the present spin degenerate problem includes a factor of 2 to account for the two spin channels. This is important to compare with the magnetic scattering problems later. The conductivity per spin channel falls below $\approx 10^{-2}$ for $\Delta \gtrsim 8$. This implies that beyond $\Delta \approx 8$, $\sigma < \sigma_{Mott}$ in the Anderson model.

The main panel in Fig.3 shows the variation in mobility edge with increasing disorder. Our error estimates are based on the shift in ϵ_c as we change from moderate to zero filtering of the $\bar{\sigma}(\mu, L)$ data. We show the data of Economou and Soukoulis [33], for comparison. The best current result on Δ_c is 16.5, our method yields $\Delta_c \sim 17$. Our results on the band edge, Fig.3.(b), match reasonably with earlier CPA based results. Note that while the mobility edge

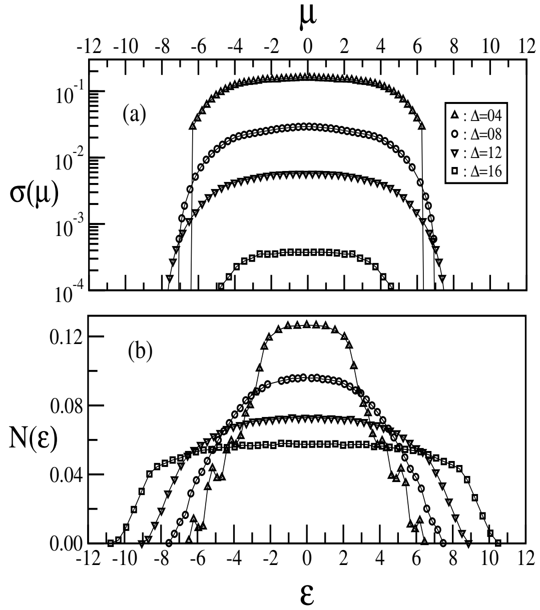

Figure 2.1: Panel (a). Variation of conductivity with Fermi energy, and panel (b). density of states, for several values of disorder, Δ.

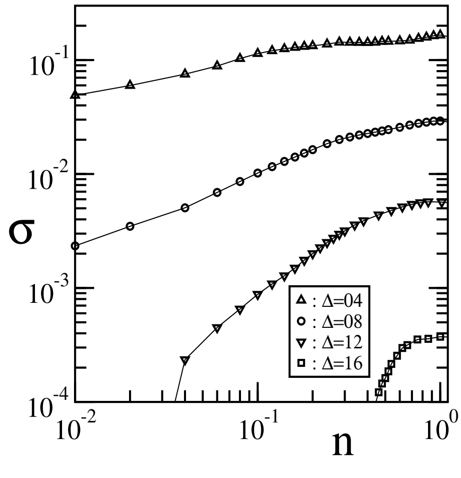

Figure 2.2: Variation of conductivity with carrier density, for several Δ, constructed from the $\sigma(\mu)$ and $N(\epsilon)$ data in Fig.1

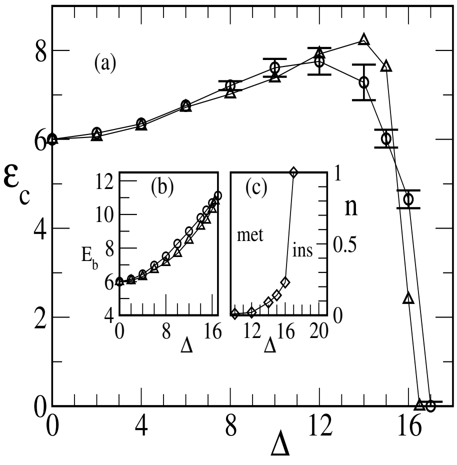

Figure 2.3: Main panel, (a), shows the variation in mobility edge with disorder. We compare our results, circles, with earlier work [33], triangles. Inset (b) shows the 'band edge', and (c) the fraction of localised states at large Δ.

has a 're-entrant' behaviour, the fraction of localised states in the band, Fig.3.(c), increases monotonically with disorder.

2.3.2 Transport regimes

There are tentatively three transport regimes in the Anderson model. These are (i) the perturbative Born scattering regime, described by the Boltzmann transport equation and the low order corrections in $(k_F l)^{-1}$. This corresponds to $\Delta/W \ll 1$, where $W = 12t$. (ii) The wide intermediate coupling regime $\Delta/W \sim \mathcal{O}(1)$, and (iii) the 'scaling' region, $\Delta \rightarrow \Delta_c$, near the MIT. We analyse the data, with increasing Δ, in the sequence $(i) \rightarrow (ii) \rightarrow (iii)$.

(i) **Perturbative regime**

To leading order, the scattering rate from the disorder is $\tau_\Delta^{-1} \sim 2\pi N(\epsilon_F)\langle\epsilon_i^2\rangle$. The second moment of the random potential is, $\langle\epsilon_i^2\rangle \sim \Delta^2/12$. Since $N(\epsilon_F) \sim 0.13$, at the band center, Fig.1.(b), the scattering rate, $\Gamma_\Delta = \tau_\Delta^{-1} \approx \Delta^2/(15t)$.

The three related quantities which define Boltzmann transport are (i) the scattering rate, Γ_Δ, defined above, (ii) the (inverse) mean free path $a_0/l \sim 0.03(\Delta/t)^2$ at the band center, and (iii) the Born-Boltzmann conductivity $\sigma_B \approx 1.62(\pi e^2/\hbar a_0) * (t/\Delta)^2$ per spin channel, again at the band center. In addition the optical conductivity should have the Drude form $\sigma(\omega) = \sigma_B/(1+(\omega^2/\Gamma_\Delta^2))$, and the 'width' in the optical conductivity can be checked against the magnitude of d.c conductivity.

Using the form for σ_B, the conductivity at $\Delta = 4$, assuming Boltzmann transport, would be approximately $0.1(\pi e^2/\hbar a_0)$ per spin channel, *i.e* ~ 0.2 in our units including spin degeneracy. Our data, Fig.2, gives a value ~ 0.19 at the band center. The crude Boltzmann scaling is obvious from the moderate Δ results in Fig.1 and Fig.2. In Fig.4 we attempt to quantify the corrections to the Boltzmann result, still staying far from the localisation regime.

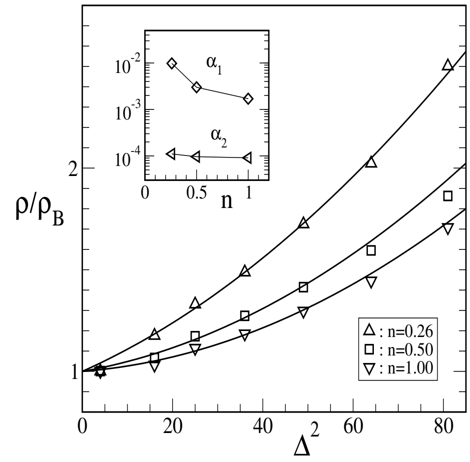

Figure 2.4: Variation of the resistivity, normalised to the Born resistivity, with disorder. The firm lines are fits of the form $1 + \alpha_1(n)\Delta^2 + \alpha_2(n)\Delta^4$. Inset shows the coefficients α_1, α_2.

The weak localisation (WL) corrections that arise beyond Boltzmann transport control the resistivity in one and two dimension. These are quantum interference effects, formally arising from the 'Cooperon' corrections. A similar argument would lead us to believe that in three dimension [1] the leading correction beyond the Boltzmann results should be $\delta\sigma \propto -(k_F l)^{-1}$. Since $(k_F l)^{-1} \propto \Delta^2$ and the Boltzmann conductivity $\sigma_B \propto k_F l$, the net conductivity would be expected to have the form $\sigma \sim \sigma_B(1 - \mathcal{O}((k_F l)^{-2}))$, *i.e*, $\sigma(\Delta) \sim \Delta^{-2}(1 - \mathcal{O}(\Delta^4))$. In that case, the *resistivity* should have a form $\rho(\Delta) \sim \rho_B(\Delta)(1 + \mathcal{O}(\Delta^4))$.

Fig.4 shows $\rho(\Delta)/\rho_B(\Delta)$ plotted against Δ^2 for three densities. We avoid too low a density to keep the scales comparable. The data are fitted to $\rho/\rho_B = 1 + \alpha_1(n)\Delta^2 + \alpha_2(n)\Delta^4$, upto $\Delta^2 = 49$ and then extrapolated to $\Delta^2 = 81$.

There are two notable features: (i) There is clearly a non zero coefficient $\alpha_1(n)$ so the equivalent of the WL corrections do not control the leading correction to σ_B in three dimension. The coefficients α_1 and α_2 are shown in the inset in Fig.4. (ii) The 'low Δ' fit seems to work reasonably for $\Delta \lesssim 10$, in the sense that $\rho/\rho_B \lesssim 2$. This *qualitative correspondence* with the Boltzmann result, even in the regime $a_0/l \gtrsim 1$, has been noticed recently [31].

The first issue has been explored in detail [34] by Belitz and Kirkpatrick who argue that the standard WL processes do not exhaust the leading corrections to σ_B in three dimension. According to them, the perturbative expansion for σ, in a continuum model, has the form

$$\sigma \sim \sigma_B\{1 - a(k_F l)^{-1} - b(k_F l)^{-2}\log(k_F l) + \mathcal{O}((k_F l)^{-2})\}$$

where a and b are numerical coefficients $\mathcal{O}(1)$. The WL argument would put $a = 0, b = 0$.

This form for the correction beyond Boltzmann transport has apparently been observed for electron mobility in dense neutral gases. The detailed coefficients in this expression would change in a tight binding model, but the key result about $k_F l$ dependence should survive.

(ii) **Intermediate coupling**

The Boltzmann result alongwith the perturabtive quantum corrections is reasonable probably upto $\Delta/W \sim 0.2 - 0.3$, although numerically the fit, in the last section, seems to describe the

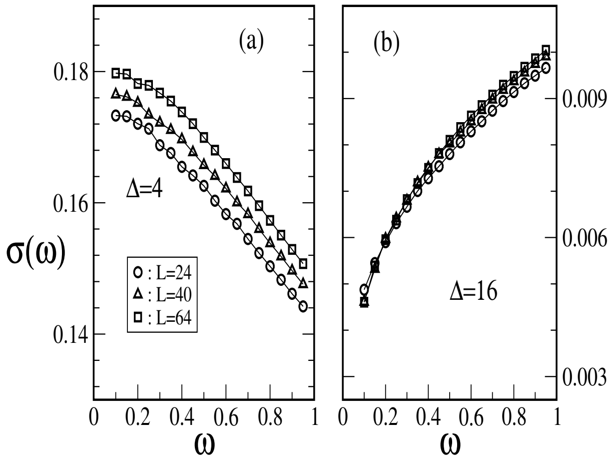

Figure 2.5: The optical conductivity, at band center, for different L . The Δ values used are representative of (a) Born scattering and (b) proximity to localisation.

resistivity even upto $\Delta/W \sim 0.75$. The scaling regime, where localisation effects become visible, occurs within about 10% of Δ_c.

Despite the correspondence of our numerical results with an extrapolation of weak coupling theory, there is no analytic framework for calculating the resistivity when the "small parameter" $(k_F l)^{-1} \sim a_0/l$ becomes $\mathcal{O}(1)$.

The paramter a_0/l is $\mathcal{O}(1)$ for $\Delta/W \sim 0.5$ but the deviation from the Boltzmann result (at the band center) is only about 25%. This has been pointed out recently by Nikolic and Allen [31] and probably arises from a fortuitious cancellation of higher order corrections. The self-consistent theory (SCT) of Vollhardt and Wolfle [19] serves as an interpolating approximation in this regime. Within the SCT also, the conductivity at band center remains within 20% of σ_B for $\Delta \lesssim 8$. The deviation from the Boltzmann result grows as we move from the band center to the band edge as evident in Fig.4.

(iii) **Scaling regime**

The scaling regime occurs close to critical disorder, within about 10% of Δ_c. The conductivity in this regime varies as $\Delta_c - \Delta$. This regime has been extensively studied to clarify the critical properties (see, *e.g*, [19] and references therein). We have not used a dense enough sampling in Δ for discussing the critical behaviour, and our system sizes too are not large enough for high accuracy calculation of the conductivity in this regime. However, based on results at $\Delta = 16$ and $\Delta = 17$ we can bracket the critical point, as shown in Fig.3. This regime has been studied in detail using transfer matrix techniques.

2.3.3 Optical conductivity

The optical conductivity $\sigma(\omega)$ is of intrinsic interest and also plays a role in our method of determining the d.c conductivity. There are some exact results known on the form of the low frequency $\sigma(\omega)$ in the Anderson model.

1. At weak disorder, when Boltzmann transport holds, the optical conductivity has the Drude form, $\sigma(\omega) \sim \sigma(0)/(1+\omega^2\tau^2)$, where $\tau^{-1} \propto \Delta^2$ as we already know. For $\omega\tau \ll 1$ this would give us the form $\sigma(\omega) \sim \sigma(0)(1-\omega^2\tau^2)$.

2. When the quantum corrections to the d.c conductivity become important the frequency dependence also picks up a non Drude form. In the intermediate disorder regime, one expects $\sigma(\omega) \sim \sigma(0) + \mathcal{O}(\Gamma\sqrt{\omega/\Gamma})$, where $\sigma(0)$ already incorporates corrections beyond the Boltzmann result. In this regime the conductivity *rises* with increasing frequency, for frequencies $\omega \ll \Gamma$.

3. At the critical point, where the zero frequency conductivity vanishes, $\sigma(\omega) \sim \omega^{1/3}$, and in the localised regime $\sigma(\omega) \sim \omega^2$.

These results originally obtained through different techniques can be obtained in a unified way via the self-consistent theory of Vollhardt and Wolfle.

Fig.5 demonstrates the changing character of $\sigma(\omega)$, at $n = 1$, as we move from the Boltzmann regime $(\Delta = 2)$, to strong disorder $(\Delta = 16)$. We show the data for three system sizes at each Δ to illustrate the explicit L dependence in $\sigma(\omega, L)$. This is important for analysing the extrapolation needed for σ_{dc}.

There are two effects of changing system size: (i) the $\sigma(\omega)$ profile itself can change with evolving system size, over the frequency range of interest, and (ii) larger system size allows access to (more dependable) low frequency data.

Fig.5.(a), the weak disorder case, reveals that the $\sigma(\omega)$ profile changes perceptibly with increasing L, the changes being $\mathcal{O}(5\%)$. This implies that in our attempt to access d.c conductivity, the contribution arises not only from lowering the frequency cutoff but also moderate changes in the $\sigma(\omega)$ profile. At strong disorder, Fig.5.(b), the profile itself does not change significantly with L and the key change in the σ_{dc} estimate comes from our ability to access lower frequencies.

2.3.4 Large L extrapolation

How important is the large L extrapolation to access the d.c conductivity, *i.e*, what is the error if we treat the low frequency average $\bar{\sigma}_{av}(L)$, at some size L, as the bulk d.c conductivity? Fig.6 illuatrates the extrapolation based on the sequence $\{L : 24, 32, 40, 48, 56, 64\}$, at $\mu = 0$, moving from weak to strong disorder.

In the weak disorder regime, the optical conductivity is 'flat' for $\omega \ll \tau^{-1}$ so if low enough frequencies can be accessed (given the finite size gaps), the d.c conductivity can be reasonably approximated. This is the feature observed at $\Delta = 2$ in Fig.6. However, in the WL region and beyond, $\sigma(\omega)$ has non trivial frequency dependence at low ω, as evident in Fig.5.(b). The corresponding low frequency average has significant L dependence. Since $\sigma(\omega) \sim \sigma(0) + \mathcal{O}(\sqrt{\omega})$, the low frequency average $\sigma_{av}(L) \sim \sigma(\infty) + \mathcal{O}(1/\sqrt{L})$. The data at $\Delta = 12, 16$ show a reasonable fit to the square root form. The much stronger frequency dependence in the strong disorder regime makes a size dependent study imperative.

These results illustrate the work involved in accessing the d.c conductivity, particularly in the regime of strong disorder, where a small L calculation (at $L = 16$ say) might overestimate the conductivity by a factor of 4. This discrepancy worsens as $\Delta \to \Delta_c$ and a systematic study of size dependence is vitally important.

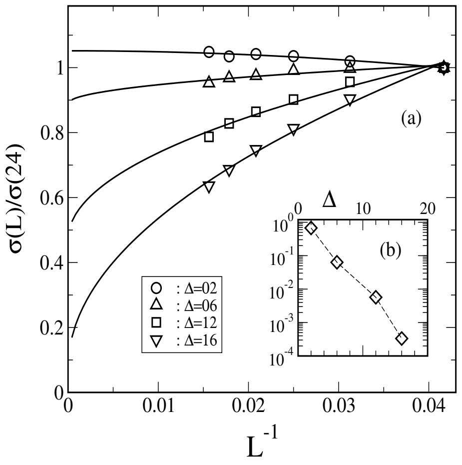

Figure 2.6: The variation of $\bar{\sigma}(L)$ with system size, in a $6 \times 6 \times L$ geometry, at various disorder. The chemical potential $\mu = 0$, so $n = 1$. Inset: variation of $\bar{\sigma}(L = 24)$ with Δ, to illustrate the rapid fall in the reference conductivity with increasing disorder.

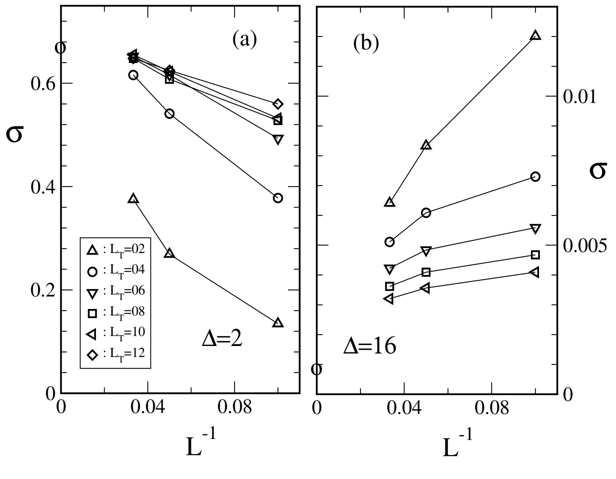

Figure 2.7: Effect of transverse dimension on the large L extrapolation. Carrier density $n = 1$. The conductivity obtained by extrapolating the $6 \times 6 \times L$ results are shown as circles on the y axes.

2.3.5 Effect of the transverse dimension

All the results quoted till now have been obtained via extrapolation on a $6 \times 6 \times L$ geometry. The 6^2 cross section was chosen to allow large L to be accessed. However, it is important to quantify the error involved in chosing a specific transverse dimension L_T. To this end we studied the low frequency average σ_{av} in a sequence $L_T \times L_T \times L$ with $L_T =, 2, 4, 6, 8, 10, 12$ and $L = 10, 20, 30$, for $\Delta = 2, 10$ and 16, and $n = 1$. The averaging interval $\Delta\omega$ was scaled as $1/(L^2 L_T)$ in all geometries.

Fig.7 shows σ_{av} with respect to L^{-1} for the sequence L_T specified above. Panel (a). shows the weak disorder, $\Delta = 2$ result. Beyond $L_T = 4$ all the curves seem to converge to $\sigma \sim 0.70$ for $L \rightarrow \infty$. The extrapolation from $L_T = 6$, obtained using L upto 64, is shown as a circle on the y axis, and is ~ 0.68.

For the strong disorder case, Fig.7.(b), the extrapolation for $L_T = 6$ is shown to be ~ 0.001, while the large L_T data, using L upto 30, suggests that the asymptotic value could be larger, ~ 0.002. This suggests that 'small' L_T somewhat underestimates the conductivity (remember $L_T = 1$ is one dimensional, so completely localised), while finite L overestimates the conductivity. Except very close to the MIT these errors are small for the sizes we use and, as verified by the phase diagram, even the critical point is located to within 5%.

2.4 Scattering from magnetic disorder

2.4.1 Global features

The effect of weak magnetic scattering on transport is quite similar to that of potential scattering. The effect is contained in the Born scattering rate, $\tau_s^{-1} \propto N(\epsilon_F) J'^2 S^2$, and the weak coupling resistivity $\rho(J', n)$ varies as $\sim b_1(n) J'^2$, where $b_1(n)$ is a density dependent coefficient. However, even at moderate coupling, $J' \sim 2$, new effects begin to show up in $\sigma(\mu)$. The conductivity at half-filling, $n \sim 1$, gets suppressed more quickly than would be guessed based on the Born argument. This deviation, and its evolution with increasing J', arises from a fundamental difference between potential scattering and magnetic scattering on a 'Kondo lattice'.

There are in fact *two* main differences that show up beyond weak coupling. These are visible when we compare Figs.8-10, with Figs.1-4. (i) The conductivity in the potential scattering case decreases monotonically (at fixed n) with increase in disorder, vanishing at $\Delta_c(n)$, while in the magnetic scattering case, at a *generic* density, the conductivity is *finite* even as $J' \rightarrow \infty$. The resistivity 'saturates' and there is no metal-insulator transition with increasing J', except in a narrow density window. (ii) The band center, $n \sim 1$, is of no particular significance in the Anderson problem, except Δ_c being largest. In the J' problem the response for $n \sim 1$ is dramatically different from that in the rest of the band. There is an MIT at $J' \approx 5$. These differences can be understood from an analysis of the strong coupling end.

For $J'/t \gg 1$ it is useful to choose a local quantisation axis at each site, for the electrons, parallel to the orientation of the spin $\mathbf{S}_i$. The coupling $J'\mathbf{S}_i$ acts as a strong local Zeeman field on the electron. Suppose the hopping term were absent. The two local eigenfunctions at each site would have spin projections parallel and antiparallel to $J'\mathbf{S}_i$, with energy $\mp J'/2$ respectively. The zero hopping problem leads to N fold degenerate levels at $\pm J'/2$. The 'gap' J' plays a key role at strong coupling. The presence of hopping generates a degenerate perturbation on the locally aligned states (say), and the electrons can now 'hop' with an amplitude that depends on the orientation of nearest neighbour spins. This mechanism has been extensively discussed in the context of the double exchange model.

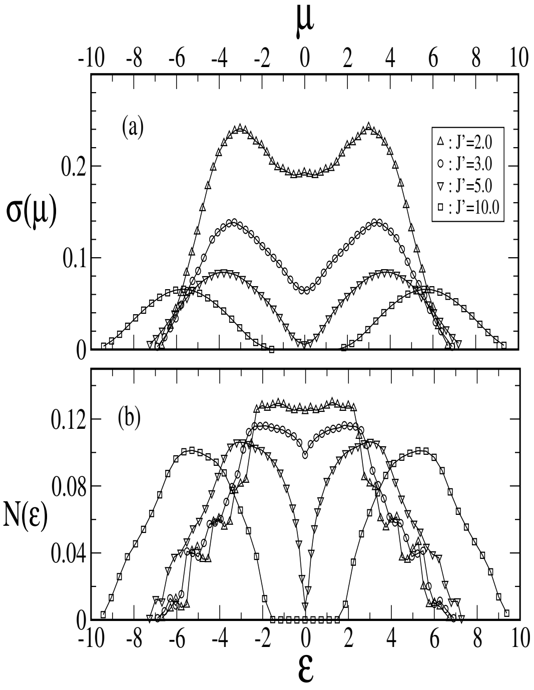

Figure 2.8: (a). Conductivity as a function of Fermi energy, (b). density of states, for different values of J', in the case of pure magnetic scattering.

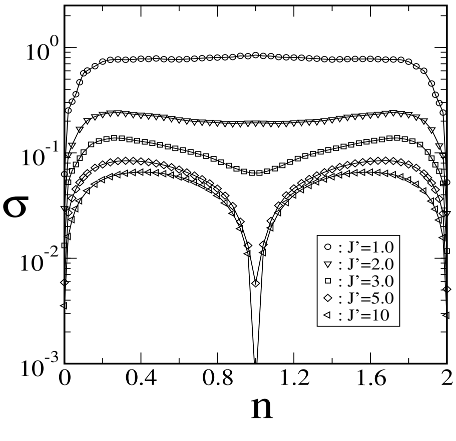

Figure 2.9: Dependence of conductivity on carrier density for varying J'. The conductivity scale is logarithmic.

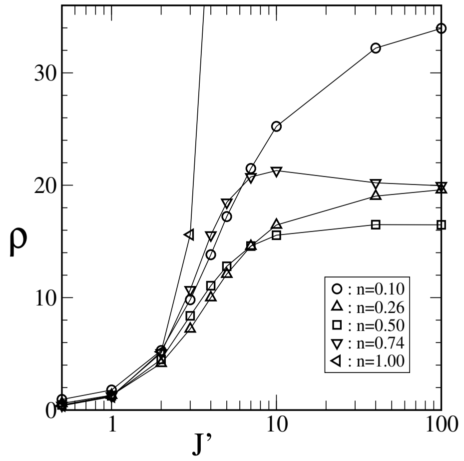

Figure 2.10: Resistivity variation with J', for several electron density, from the perturbative limit to double exchange

The mixing introduced by 'hopping' broadens the two levels into bands. For $J' \gtrsim W/2$ the broadening due to t does not fill the gap, *and the system is insulating at* $n = 1$. For J' below this critical value, J_c, say, the DOS at band center is suppressed but finite, and the resistivity is still very large. In summary, the strong coupling physics of (incipient) band splitting controls the resistivity close to band center, and creates an essential difference, in terms of J' and n, with respect to standard Anderson localisation.

The saturation in $\rho(J')$ with increasing J', over most of the band, occurs because the effect of large J' is absorbed mainly in the band splitting. The effective *disorder* seen by the electrons comes from fluctuations in the hopping amplitudes, explained in the next section, and these are $\mathcal{O}(t)$. The ratio of fluctuation to mean hopping is moderate, so the large J' limit leads to a 'dirty metal' but no metal-insulator transition. This is unlike the Anderson problem where the electrons scatter off potential fluctuations whose amplitude grows with increasing Δ.

From the data in Figs.8-10 we can now identify the different transport regimes.

2.4.2 Transport regimes

(i) **Weak coupling:** $J'/W \ll 1$

The magnetic scattering rate Γ_s is proportional to $N(\epsilon_F)J'^2$, and the weak coupling resistivity should be expandable in Γ_s. The lowest order term is well known, corresponding to Born scattering, with $\rho(J', n) \sim b_1(n)J'^2$. The density dependence is similar to that for potential scattering. Assuming $\rho(J')$ to be analytic in Γ_s, *i.e* ignoring possible log corrections etc, Fig.11 shows a fit of the form $\rho(J', n) \sim b_1(n)J'^2 + b_2(n)J'^4$ to the low J' resistivity. The J'^2 character dominates upto $J' \sim 2$, as one can see also in the $\sigma(n)$ plot in Fig.9, beyond which the quartic term becomes important. We do not know if the coefficient of the quartic term has been analytically calculated, but the *sign* of this term is crucial, and is density dependent, as we discuss next.

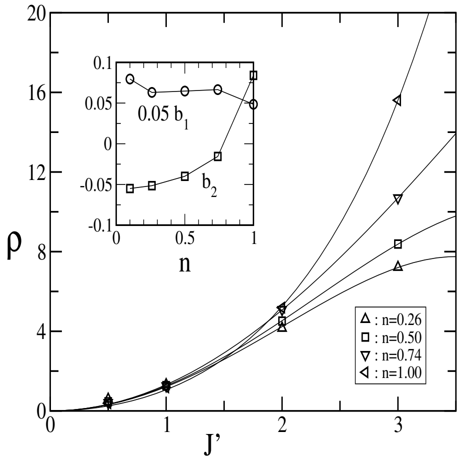

Figure 2.11: Weak coupling resistivity. The firm lines are the fits of the form $b_1(n)J'^2 + b_2(n)J'^4$. Inset shows the coefficients b_1 and b_2 as a function of n

(ii) **Intermediate coupling:** $J'/W \sim \mathcal{O}(1)$

As is obvious from the data in Fig.9-10, the resistivity saturates with increasing J', over most of the band. The exception is the vicinity of $n = 1$, and the lower edge of the band.

This suggests that the correction to the Born resistivity is *negative* for n away from $n = 1$, and changes sign as $n \to 1$. Fitting the data to $\rho(J', n) = b_1(n)J'^2 + b_2(n)J'^4$, the coefficient $b_2(n)$ illustrates the crossover from saturation to escalation, as we move across the band. Fig.11 shows the fit to this form and the coefficients are shown in the inset. The 'Born' coefficient is positive throughout the band, without significant density dependence in the density interval shown. The quartic coefficient changes sign, from positive to negative, as n is lowered from 1.0 to 0.74.

A confirmation of saturation or escalation cannot of course be obtained from a low order expansion in J'^2, but even the 'perturbative' coefficient provides a hint of strong coupling physics. It also suggests a smooth evolution from weak to strong coupling.

(iii) **Double exchange:** $J'/W \to \infty$

In the double exchange limit the J' scale acts as a 'constraint' on the electron spin orientation and no longer directly affects physical properties, the only effect is to renormalise the chemical potential. The mapping of the $J'/t \to \infty$ problem to a 'spinless fermion' problem with hopping dependent on nearest neighbour spin orientation has been widely discussed [35]. Transformed to spinless fermions, which correspond to original electron states with spin projection 'locked' parellel to the local quantisation axis, $\mathbf{S}_i$, the Hamiltonian becomes:

$$H = \sum_{\langle ij \rangle} t_{ij} \gamma_i^\dagger \gamma_j = \sum_{\langle ij \rangle} \bar{t} \gamma_i^\dagger \gamma_j + \sum_{\langle ij \rangle} \delta t_{ij} \gamma_i^\dagger \gamma_j \tag{2.8}$$

The t_{ij} being the spin orientation dependent hopping amplitude specified earlier. We can split it into the mean (uniform) hopping amplitude, $\bar{t}$, and the fluctuation δt_{ij}.

In the 'extreme' paramagnetic phase of this model, the distribution of hopping integrals is exactly known. The spins are independently distributed on a sphere so the t_{ij} can be worked out. There is no obvious small parameter, since both the mean value of hopping, $\bar{t}$, as well as the fluctuation, $\Delta t = \sqrt{\langle \delta t^2 \rangle}$, are $\propto$ t. However, the ratio $\Delta t/\bar{t} \approx 1/3$. Numerical work by Li *et al.* had demonstrated that less than 0.3% of states in the band are localised under this condition. It was not clear whether the resistivity at the band center, $n = 0.5$, could be described within a Boltzmann approach. Narimanov and Varma [36] have demonstrated that the mean free path emerging from the Boltzmann calculation is $l/a_0 \gtrsim 8$ so the method is self-consistent.

It seems now that despite the localisation effects as $n \rightarrow 1$ and $n \rightarrow 0$, resistivity over much of the band can be understood within a effective 'weak coupling' approach. The resistivity is $\approx (0.1 - 0.2)\rho_{Mott}$ at the band center according to our calculation. The resistivity is also 'particle-hole' symmetric, now within the lower band, but notice that this is cleanly visible only at very large J'/t.

(iv) **Virtual orbital mixing: large finite J'**

As we move to finite J' from the double exchange limit, the two bands still remain split (down to $J'/t \approx 5$) but there is a virtual admixture that is introduced. To access properties in this regime we need to use a two orbital formulation, with the orbital energies still separated by a large gap $\sim J'$. The chemical potential remains in the lower band. The two orbital model, written in terms of electronic states with local quantisation axis, has the form:

$$H = \sum_{ij} t_{ij}^{\alpha\beta} \gamma_{i\alpha}^{\dagger} \gamma_{j\beta} - \mu \sum_{i} n_i - \frac{J'}{2} \sum_{i} (n_{i\alpha} - n_{i\beta}) \tag{2.9}$$

We have not seen a Boltzmann calculation of transport in this regime, but using the two orbital formulation it might be possible to set up such a scheme. The resistivity *decreases* as we move down from large J', so using the correct 'basis' the transport may be accessible within a Boltzmann approach (since the double exchange limit is itself so accessible). The increase in conductivity, $\delta\sigma(J')$, as we move to lower J', is found to be proportional to $1/J'$. A perturbative correction to the large J' result, within a diagrammatic scheme yields the same answer.

(v) **Behaviour near band tails**

Spin disorder by itself cannot localise states in the center of the band, since $\Delta t/t$ is not large enough. However at the band tails, *i.e* n close to 1 or 0, the kinetic energy is small and a small fraction of states can still be localised. This was estimated by Li *et al.* [24] to be $\lesssim 0.5\%$ of the total number of states. We do not know if any analytic approaches have been explored in this localisation problem with 'hopping disorder'. This regime would be relevant to the low doping magnetic semiconductors, where there is also the possibility of carriers trapping into spin polaronic states.

2.4.3 Optical conductivity

The optical conductivity confirms the trends seen in the d.c conductivity. Fig.12 shows $\sigma(\omega)$ at $J' = 1$ and $J' = 4$, weak and 'strong' coupling respectively, at the center $(n = 0.5)$ and edge $(n = 1)$ of the lower band.

At weak coupling, over the frequency range shown, $\sigma(\omega)$ is larger at $n = 1$, the center of the *full band*, compared to $n = 0.5$. The scattering rate is $\Gamma_s = 2\pi N(\epsilon_F) J'^2$ which at the

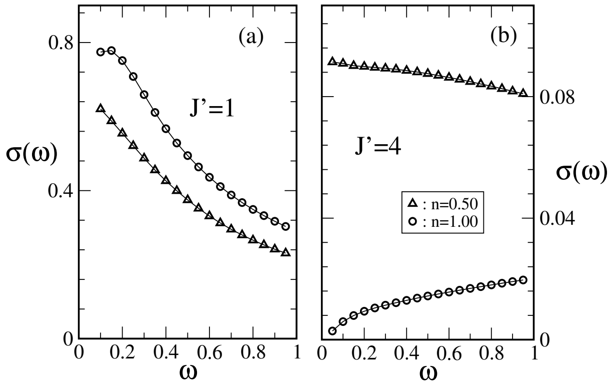

Figure 2.12: Optical conductivity in the (a) weak and (b) moderate magnetic scattering regimes at two densities.

band center is ≈ 0.75. If $\sigma(\omega)$ follows the Drude form then $\sigma(\Gamma_s)/\sigma(0)$ should be ~ 0.5, which is consistent with Fig.12.(a). By $J' = 4$, the trend has reversed. The $n = 1$ case is almost insulating, with $\sigma(0) \rightarrow 0$, while the conductivity at the (lower) band center is finite and essentially flat on the scale considered. This trend gets amplified as we go to even larger J'.

2.5 Combined structural and magnetic disorder

2.5.1 Global features

In the presence of both structural and magnetic disorder it is not possible to show the full density dependence of transport properties compactly, so we provide two generic 'cross sections' in Fig.13 at $n = 0.26$ and $n = 1.00$. In addition to the features already noted for potential scattering and magnetic scattering, there are several novel features that arise.

- For weak J' and moderately large Δ, magnetic scattering actually *weakens* localisation effects, as evident from the intermediate Δ, small J' data in Fig.13,15,16.
- At even larger Δ, where the system would have been Anderson localised, magnetic scattering actually leads to a metal. The critical disorder $\Delta_c(n)$ shifts to a larger value $\Delta_c(n, J')$, see phase diagrams in Fig.14.
- At large J' now, the system can go insulating depending on the extent of structural disorder. The resistivity could 'escalate' rather than saturate with increasing J'. This is in contrast to the generic behaviour in the 'clean' magnetic system.
- The 'additivity' of magnetic and structural scattering holds only over a very limited range in Δ and J'.

The major features can be easily motivated after we discuss the different transport regimes in this problem. Primarily, (i) The metallic regime 'expands' as magnetic scattering is turned on in the structural disorder problem, it takes a larger structural disorder to localise. (ii) At large J', the 'spinless fermion' limit, the critical structural disorder needed is *less* than at $J' = 0$, since structural and magnetic disorder 'add up'. This is visible in Figs.14.(a-c). The

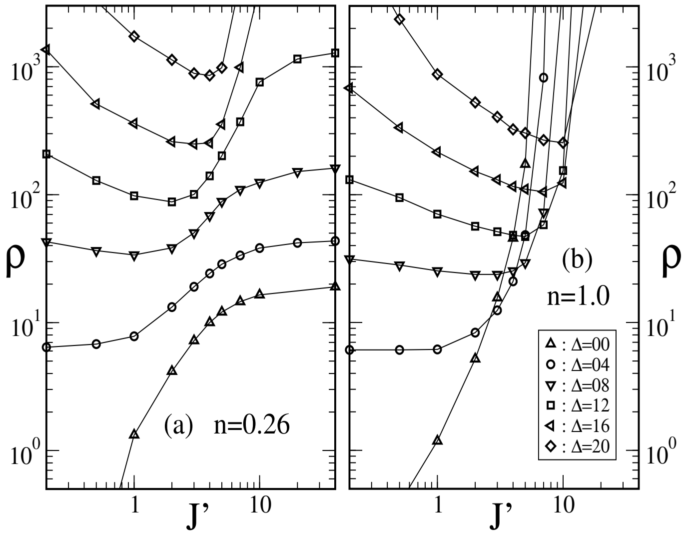

Figure 2.13: Global behaviour of the resistivity at $n = 0.26$ and $n = 1.0$

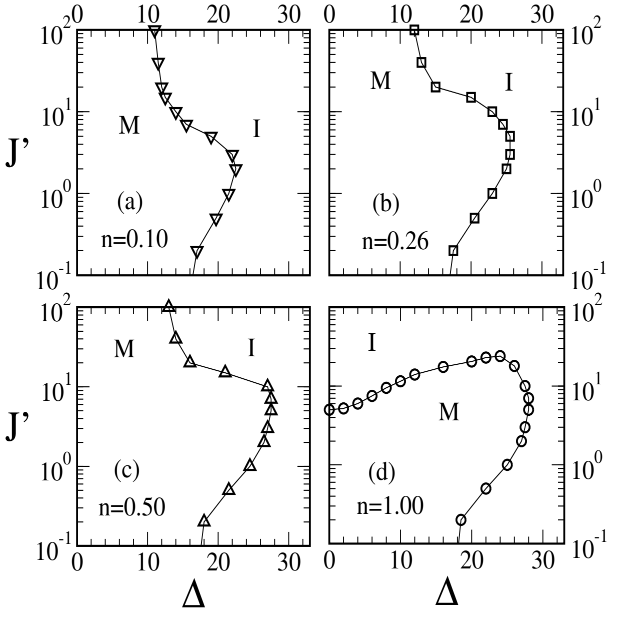

Figure 2.14: Putting together different constant density cross-sections to create a 'global' insulator-metal phase diagram for the $\Delta + J'$ problem.

resulting 'nose' is ubiquitous, except at $n = 1$. (iii) At, and near, $n = 1$ the bands splitting leads to an insulating state at $J' \sim 5$, so the metallic phase is bounded both in J' and Δ. However, there is an interesting re-entrant structure, which we will discuss later.

The detailed discussion in the rest of this section is focused on $n = 0.5$, where the response is generic of the entire band (see the phase diagrams in Fig.14).

2.5.2 Transport Regimes

There are tentatively *five* different transport regimes in the problem, and, except for (i) below, all of them are beyond the reach of standard transport theory. These are: (i) the weak scattering regime, where Mathiessens rule holds, (ii) spin flip correction to weak localisation (WL), with the Δ dependence showing WL corrections and spin flip increasing the conductivity, (iii) spin dephasing driven insulator-metal transition (IMT), occuring over a window in Δ, (iv) the disordered double exchange (DE) limit, and (v) the intermediate coupling 'metal'. We analyse our data in the spirit of this classification.

(i) **Weak scattering: Mathiessens rule**

The regime of weak structural disorder and weak electron-spin coupling can be understood in terms of additive Born scattering, with the net scattering rate, $\Gamma(\Delta, J') \approx a_1\Delta^2 + b_1 J'^2$. The resistivity is additive and both contributions are described by lowest order perturbation theory. This corresponds to the bottom left hand corner in Fig.15.(a). The 'parallel' curves in Fig.16.(a) for Δ upto 4, and the regime $J' \leq 3$ broadly identify the domain of 'Mathiessens rule'. The net resistivity in this regime, Fig.16.(a), is $< 0.1\rho_{Mott}$, *i.e*, a few hundred $\mu\Omega$cm.

(ii) **Spin flip correction to weak localisation**

In the structural disorder problem the quantum corrections to the conductivity become important with growing Δ, and show up via the WL effect. This effect is already beyond standard transport theory. In this regime, with $\Delta/W \sim 1$, the effect of magnetic scattering, even with with $J'/W \ll 1$ is non trivial. Spin flip scattering of the electrons [22, 23], by the random magnetic moments serves to *suppress* the localising effect of structural disorder, Fig.15.(a) and Fig.16.(a), as we discuss below.

Just as inelastic scattering leads to decoherence, and a suppression of quantum interference, spin flip scattering of the electrons, arising from processes of the form $(S_{xi} + iS_{yi})c^{\dagger}_{i\downarrow}c_{i\uparrow}$ etc, leads to *spin decoherence* and a corresponding cutoff to WL corrections. If the dephasing time is τ_s, then the spin diffusion length is $l_s = \sqrt{D\tau_s}$, with the diffusion constant $D \propto \Delta^{-2}$, and $\tau_s^{-1} \propto J'^2$. The WL correction gets *corrected* [1] by $\delta\sigma \propto l_s^{-1} \propto \Delta|J|$. If the WL correction to the conductivity scales as $\sim (k_F l)^{-1} \sim \Delta^2$, then the corresponding spin flip correction to the *resistivity* should behave as $\delta\rho \sim -\Delta^5|J'|$.

Fig.16.(a) shows $\rho(J', \Delta)$ in the moderate J' region, with Δ increasing beyond the Born scattering regime. At weak disorder the resistivity has the expected form $\rho(\Delta, J') \propto a_1\Delta^2 + b_1 J'^2$, while at larger disorder we expect the Δ dependence to be stronger, *and simultaneously a positive contribution to the conductivity* $\delta\sigma \propto |J'|$ *to show up*. The coefficient of the J'^2 term could also be renormalised at large Δ. Taking these possibilities into account we fit the low J' resistivity to the form: $\rho(\Delta, J')|_{J' \to 0} \approx \rho_1(\Delta) + b_1 J'^2 + c_1(\Delta)|J'| + f(\Delta)J'^2$, where the coefficients would depend on electron density. $\rho_1(\Delta)$ tracks the localising effect of structural disorder, $c_1(\Delta)$ measures the 'antilocalising' effect of spin flip scattering, and $d_1 = b_1 + f(\Delta)$ monitors the renormalised 'Born scattering' from spins.

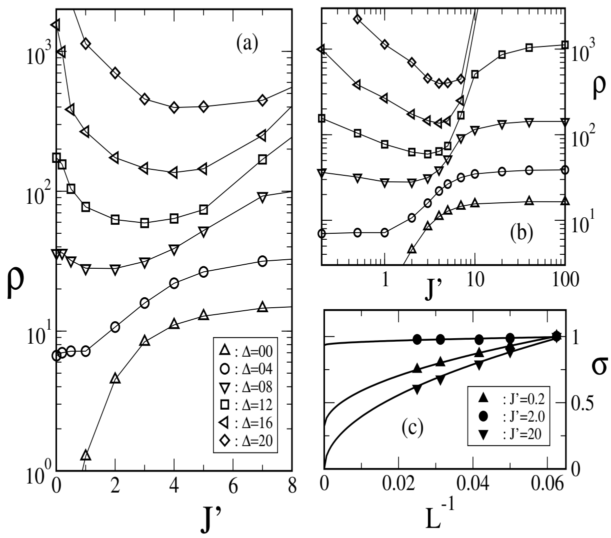

Figure 2.15: Variation of resistivity, ρ, with J' and Δ. Density $n = 0.5$. Data obtained by extrapolation on a sequence of sizes $6 \times 6 \times L$, with L varying from 24 to 40. Panel (a) shows ρ in the intermediate J' regime, while panel (b) shows a 'global' view, with a logarithmic J' scale. Panel (c) shows how the 'd.c conductivity' is obtained by extrapolation, illustrating the behaviour for various J' at $\Delta = 16$, *i.e*, near the Anderson MIT. The conductivity in panel (c) is normalised to $\sigma(L = 24)$.

For $n = 0.5$, the resistivity from structural disorder, $\rho_1(\Delta) \approx a_1\Delta^2 + a_2\Delta^4 + a_3\Delta^6$, as we fit in Fig.16.(b), with $a_1 = 0.408$, $a_2 = 3 \times 10^{-4}$, and $a_3 = 4 \times 10^{-5}$. The coefficient of the 'anti-localisation' term, Fig.16.(c) is $c_1(\Delta) \approx c_0\Delta^{\alpha}$, with $c_0 = -3.4 \times 10^{-4}$, and $\alpha \sim 5$. The (renormalised) coefficient of the J'^2 term, $d_1 = b_1 + f(\Delta)$, has the form indicated in Fig.16.(d). While Fig.16.(b) highlights the rapid growth in resistivity due to structural disorder, Fig.16.(c) indicates how this growth is cutoff via the spin flip scattering effected by J'. This affects the metal-insulator phase boundary as we discuss next.

(iii) Spin dephasing driven IMT

There is no perturbative scheme as the disorder increases beyond the weak localisation regime. The SCT provides a guide and of course there is extensive numerical work on the Anderson transition. Unfortunately, the SCT has no equivalent that includes magnetic scattering as well (although there were early attempts in two dimension [37]), and we do not know of even numerical work probing the MIT including magnetic scattering.

As Δ drives the system towards localisation, the effect of *weak* J' is dramatic. The small increase in conductivity, correcting the weak localisation contribution, now develops into a full fledged anti-localisation effect, enlarging the domain of the metallic phase, see phase diagrams in Fig.14, and pushing up the critical disorder needed for localisation. The critical disorder now depends on J' and increases from $\Delta \approx 16.5$, at $J' = 0$, to $\Delta \sim 27$ at $J' \sim 8$, before dropping to $\Delta \sim 12$ for $J' \rightarrow \infty$ (see Fig.14.(c)). The optical conductivity data, Fig.18 illustrates how the low frequency conductivity *increases* as J' grows from 0.2 to 2.0, at $\Delta = 16$, and drastically reduces again for $J' = 20$. *There is an insulator-metal-insulator transition with increasing* J' *for* $26 > \Delta > 16.5$.

While the IMT driven by 'small J'' may be motivated as the 'extrapolation' of the antilo-

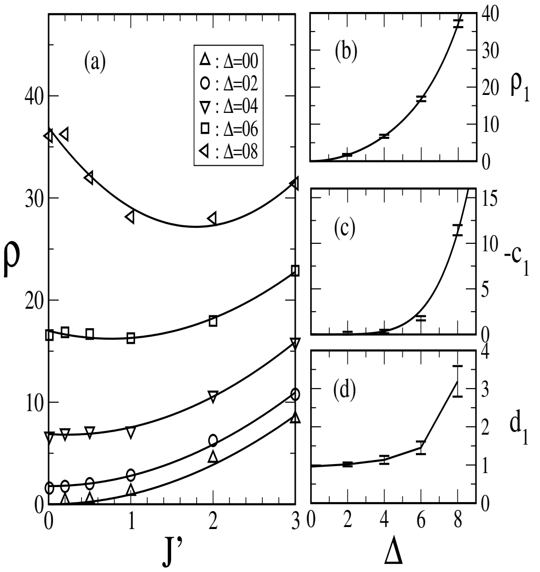

Figure 2.16: Resistivity at small J': (a) Quadratic fit to the extrapolated resistivity: $\rho(J') \approx \rho_1(\Delta) + c_1(\Delta)|J'| + d_1(\Delta)J'^2$, at weak coupling, and moderate Δ. (b) $\rho_1(\Delta)$, with a polynomial fit (see text), (c) The coefficient $-c_1$, with a power law fit (see text), and (d) coefficient d_1.

calising effect of spin flip scattering, new physical effects emerge rapidly as J' is increased, staying in the large Δ regime. The reducing resistivity, Fig.15. and Fig.16.(a), exhibits a minima, and then *rises* again with increasing J'. Such behaviour can be viewed as an extension of the J'^2 term seen at weak disorder, but it is probably more fruitful to approach the problem from the strong coupling, double-exchange, end.

(iv) Double exchange with disorder

This regime corresponds to $J'/W \rightarrow \infty$, in the presence of arbitrary structural disorder, *i.e*, the right edge of Fig.15.(b). The form of the resistivity $\rho(J')$ arising from 'magnetic disorder' at large J' is very different from what one observes in $\rho(\Delta)$ at large Δ. This is because J' contributes to both 'band splitting' and effective disorder, and the effective disorder saturates as $J'/W \rightarrow \infty$ with J' controlling only the band splitting.

The standard transformation to spinless fermions leads to the hopping disordered model with t_{ij} dependent on nearest neighbour spin orientation:

$$H = \sum_{ij} t_{ij}(\theta, \phi)\gamma_i^{\dagger}\gamma_j + \sum_i \epsilon_i \gamma_i^{\dagger}\gamma_i \equiv \sum_{ij} t_0 \gamma_i^{\dagger}\gamma_j + \sum_{ij} \delta t_{ij}\gamma_i^{\dagger}\gamma_j + \sum_i \epsilon_i \gamma_i^{\dagger}\gamma_i$$

with the hopping amplitude specified earlier. As before we have split t_{ij} into the 'mean hopping', $t_0 = \langle |t_{ij}| \rangle$, and the fluctuation δt.

The localisation properties of this model have been studied by Li *et al.* [24], although they did not calculate the resistivity. The 'hopping disorder' by itself localises less than 0.5% of the states in the band, and, as we observe, the resistivity at band center remains finite, $\sim 0.2\rho_{Mott}$. On adding structural disorder the mobility edge moves inward, with localisation

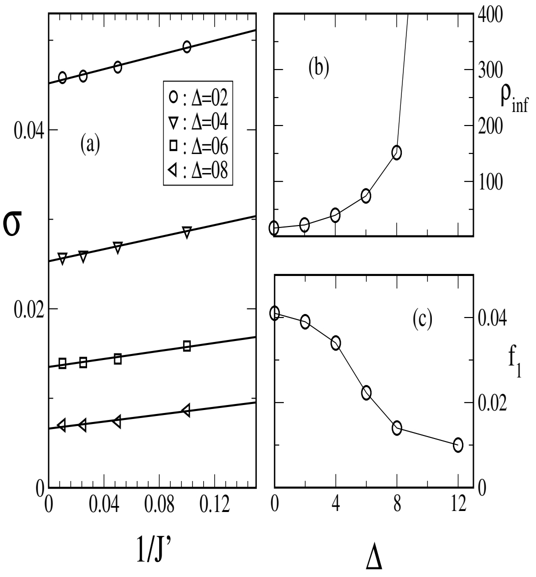

Figure 2.17: Resistivity at large J': (a) Fit to $\sigma(J', \Delta)$ of the form $\sigma(\infty, \Delta) + f_1/J'$. (b) Resistivity in the double exchange limit $\rho(\infty, \Delta) = 1/\sigma(\infty, \Delta)$. (c) The coefficient f_1.

of the full band occuring at $\Delta/t \sim 11.5$. The critical disorder, visible approximately at large J' in Fig.14.(c), can be motivated by the band narrowing in t_0 compared to t. In the fully spin disordered phase $t_0/t \sim 2/3$, and a crude scaling of $\Delta_c(J' = 0)$ would suggest, $\Delta_c(\infty)/\Delta_c(0) \sim 2/3$, so that the double exchange model in the paramagnetic phase would localise at $\Delta \sim 11$. The small deviation from this value arises from the presence of δt_{ij} and the Berry phase involved in it. Apart from the mobility edge calculation [24] we do not know of any exact results on transport in the strongly disordered double exchange model.

The growth in resistivity with Δ, remaining at large J', is visible in the right edge of Fig.17.(b). Within our calculation the MIT at large J' occurs slightly above $\Delta = 12$.

(v) Strong disorder and intermediate coupling

This is the most complicated regime in the problem and also the most relevant for real disordered magnetic systems. The regime corresponds to $\Delta/W \sim 1$ and $J'/W \sim 1$, and, as obvious from Fig.15, $\rho/\rho_{Mott} > 1$. This is a nominally 'metallic' but diffusive, highly resistive regime. There are no analytical tools for directly estimating transport properties in this regime, but much of the physics can be motivated by an expansion about the double exchange limit.

When J' is finite, both the electron spin states, polarised parallel and anti-parallel to the core spin, need to be retained. In terms of these states the Hamiltonian assumes the form:

$$H = \sum_{ij} t_{ij}^{\alpha\beta} \gamma_{i\alpha}^{\dagger} \gamma_{j\beta} + \sum_{i} \epsilon_i n_i - \frac{J'}{2} \sum_{i} (n_{i\alpha} - n_{i\beta})$$

At large J' the chemical potential will be in the lower band, if we want $n < 1$. We can split the $t_{ij}^{\alpha\beta}$, as we did for the single band model, into mean amplitudes and fluctuations. The

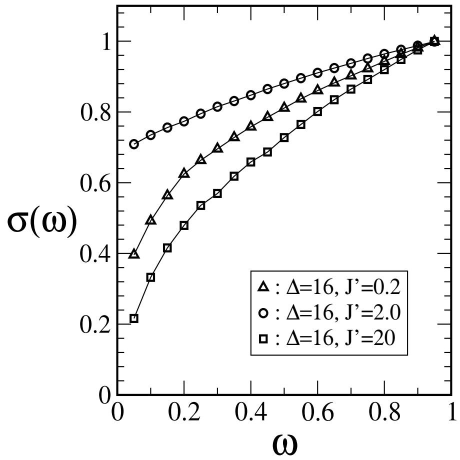

Figure 2.18: The optical conductivity illustrating the re-enterant localisation with increasing J' at a fixed Δ.

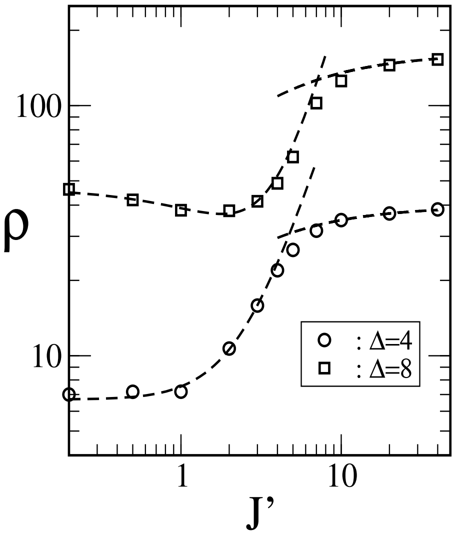

Figure 2.19: Combining the weak coupling and strong coupling expansions. Symbols are the actual data, dashed lines are the fits from the small and large J' ends.

major source of disorder is still ϵ_i, with additional contribution from the $\delta t_{ij}^{\alpha\beta}$. The orbital mixing effect of 'off diagonal' couplings, either in terms of mean amplitude or fluctuations, is regulated by the large energy denominator J'. Although the 'reference' problem, $J' \rightarrow \infty$, is not analytically tractable in the presence of structural disorder, we expect orbital mixing to generate corrections to conductivity $\sim \mathcal{O}(1/J')$. Fig.17.(a) fits the data, for Δ upto 8 and J' down to 6, to the form $\sigma(J', \Delta)\,|_{J' \rightarrow \infty} \approx \sigma(\infty, \Delta) + d_1/J'$. Fig.17.(b) show $\rho(\infty, \Delta) = 1/\sigma(\infty, \Delta)$ and Fig.17.(c) is the coefficient f_1.

Fig.19 puts together the weak coupling and strong coupling fits to $\rho(J', \Delta)$, for $\Delta < 8$, comparing with the full numerical data. The quality of the fit indicates that the dominant transport regimes in this problem can be classified as we had suggested earlier and some of the physics can be motivated by extending concepts that are already available in the transport literature. The regions of MIT cannot be described by these expansions and should probably be accessed via a complementary scaling approach.

2.6 Concluding remarks

In this chapter we have presented exact results on electron transport in the background of arbitrary structural and spin disorder and provided a framework within which the data can be analysed. We have identified and explored the distinct transport regimes that arise in the case of pure magnetic scattering, as well as the combined effect of structural and magnetic disorder, In contrast to the effect of only structural disorder (where the resistivity 'escalates' with increasing disorder) or only magnetic scattering (where it 'saturates' with increasing disorder) their combined action can lead to non monotonic dependence. The method developed in this chapter can be directly taken over in calculating the resistivity in the presence of annealed disorder, and is extensively used in the succeeding chapters.

Bibliography

[1] P. A. Lee and T. V. Ramakrishnan, Rev. Mod. Phys. **57**, 287 (1985).

[2] B. Kramer and A. MacKinnon, Rep. Prog. Phys. **56**, 1469 (1993).

[3] N. F. Mott and E. A. Davis, *Electronic Processes in Non Crystalline Materials*, Clarendon Press, Oxford (1979).

[4] N. F. Mott, *Metal-Insulator Transitions*, Taylor & Francis, London (1990).

[5] A. C. Hewson, *Kondo Problem to Heavy Fermions*, (Cambridge University Press, Cambridge).

[6] Y. Kuramoto and Y. Kitaoka, *Dynamics of Heavy Electrons*, (Oxford University Press, Oxford 2000)

[7] See, for example, S. Sullow *et al.*, Phys. Rev. Lett. **78**, 354 (1997).

[8] A. Amato, Rev. Mod. Phys. **69**, 1119 (1997).

[9] T. Dietl *et al.*, Science, **287**, 1019 (2000).

[10] G. Alvarez, M. Mayr and E. Dagotto, Phys. Rev. Lett, **89**, 277202-1 (2002).

[11] M. Berciu and R.N. Bhatt, Phys. Rev. Lett. **87**, 1072 (2001).

[12] S. Paschen *et al.*, Phys. Rev. **B 61**, 4174 (2000).

[13] S. Sullow *et al.*, Phys. Rev. **B 57**, 5860 (1998).

[14] A. P. Ramirez, J. Phys. Condens Matter **9**, 8171 (1997), E. Dagotto *et al.*, : Phys Rep **344**, 1 (2001), *Colossal Magnetoresistive Oxides*, Ed. Y. Tokura, Gordon & Breach (2000)

[15] F. Hellman, M. Q. Tran, A. E. Gebala, E. M. Wilcox and R. C. Dynes, Phys. Rev. Lett. **77**, 4652 (1996).

[16] P. Majumdar and S. Kumar, Phys. Rev. Lett. **90**, 237202 (2003).

[17] S. Legvold in *Ferromagnetic Materials, Vol I*, Ed. E. P. Wohlfarth, (North Holland, Amsterdam (1999).

[18] Gorkov et. al. , JETP Lett. **30**, 248(1979)

[19] See D. Vollhardt and P. Wolfle in *Electronic Phase Transitions*, Ed. W. Hanke and Yu. V. Kopaev, North Holland, Amsterdam (1992).

[20] Bulka et. al. , Z. Phys. B **66**, 21 (1987)

[21] Efetov , Adv. Phys. **32**, 53 (1983)

[22] P. A. Lee, J. Non Cryst. Solids, **35**, 21 (1980).

[23] S. Hikami, A. I. Larkin and Y. Nagaoka, Prog. Theor. Phys. **63**, 707 (1980).

[24] Q. Li, J. Zang, A.R. Bishop and C.M. Soukoulis, Phys. Rev **B 56**, 4541 (1997).

[25] P. G. de Gennes and J. Friedel, J. Phys. Chem. Solids **4**, 71 (1958).

[26] Michael E. Fisher and J. S. Langer, Phys. Rev. Lett. **20**, 665 (1968).

[27] See, for example, Fazekas, *Lecture Notes on Electron Correlation and Magnetism*, (World Scientific,)

[28] J. A. Mydosh, *Spin Glasses*, Taylor & Francis (1993).

[29] G. D. Mahan, *Quantum Many Particle Physics*, Plenum Press, New York (1990).

[30] S. Datta, *Electronic Transport in Mesoscopic Systems*, (Cambridge University Press, Cambridge 1992).

[31] B. K. Nikolic and P. B. Allen, Phys. Rev. **B 63**, 020201-(R) (2000)

[32] K. Slevin, T. Ohtsuki and T. Kawarabayashi, Phys. Rev. Lett. **84**, 3915 (2000).

[33] Economou and Soukoulis, Phys. Rev. B **28**, 1093(1983)

[34] T. R. Kirkpatrick and D. Belitz, Phys. Rev. **B 34**, 2168 (1986).

[35] E. Mller-Hartmann and E. Dagotto, Phys. Rev. **B 54**, R6819 (1996).

[36] E. E. Narimanov and C. M. Varma, Phys. Rev. **B 65**, 024429 (2002).

[37] D. Yoshioka *et al.*, J. Phys. Soc. Jpn, **50**, 3419 (1981).

Chapter 3

Effective Spin Hamiltonian for Double Exchange Models

Chapter Summary: We propose a scheme for constructing classical spin Hamiltonians from Hunds coupled spin-fermion models in the limit $J_H/t \rightarrow \infty$. The strong coupling between fermions and the core spins requires self-consistent calculation of the effective 'exchange' in the model, either in the presence of inhomogeneities or with increasing temperature. In this chapter we discuss results mainly on homogeneous phases, with self consistently renormalised couplings, and compare our results with exact simulation of the double exchange model. We can access system sizes much beyond the reach of 'exact' simulations, and study transport and optical properties of the model without artificial broadening. The generalisation to handle quenched disorder or competing interactions is made in subsequent chapters. Some of the results in this chapter appear in our preprint cond-mat 0305345.

3.1 Introduction

The double exchange (DE) model was introduced by Zener [1] in 1951 to motivate ferromagnetism in the perovskite manganites. In contrast to 'Heisenberg like' coupling between localised spins, the effective interaction in 'double exchange' arises from optimisation of carrier kinetic energy in the spin background. The intimate correlation between spin configuration and electron motion had, till recently, restricted the study of the DE model to mostly qualitative analysis or mean field theory. The original proposal of Zener was followed up [2] by Anderson and Hasegawa, who clarified the physics of the coupled spin-fermion system in a two site model, and de Gennes [3] who presented a thermodynamic calculation and a phase diagram (incorporating antiferromagnetic superexchange). He produced the first estimate of transition temperature (T_c) in the model. The thermodynamic transition within double exchange was also studied [4] by Kubo and Ohata. This short list essentially exhausts activity on the double exchange problem prior to the 'manganite renaissance'.

The discovery of colossal magnetoresistance (CMR) and a variety of magnetic phases in the manganites [5] led to renewed interest in the DE model. In addition, the availability of powerful analytical and numerical tools, *e.g* , dynamical mean field theory (DMFT) and Monte Carlo methods provided impetus for studying the DE model in detail. In real systems the double exchange interaction is supplemented by [6] antiferromagnetic (AF) superexchange, electron-phonon interactions, and disorder, and some of these models have been studied within various approximations. In this chapter our detailed results are on the clean DE model, and we only briefly discuss the effect of disorder and competing magnetic interactions. These effects are discussed in detail in later chapters.

Let us define the Hamiltonian, and the parameters relevant in our problem.

$$\begin{aligned} H &= H_{el} + H_{AF} \\ H_{el} &= \sum_{\langle ij \rangle, \sigma} t_{ij} c^{\dagger}_{i\sigma} c_{j\sigma} + \sum_i (\epsilon_i - \mu) n_i - J_H \sum_i \mathbf{S}_i . \vec{\sigma}_i \\ H_{AF} &= J_S \sum_{\langle ij \rangle} \mathbf{S}_i . \mathbf{S}_j \end{aligned} \tag{3.1}$$

The $t_{ij} = -t$ are nearest neighbour hopping, on a square or cubic lattice as relevant. The on site potential is uniformly distributed between $\pm\Delta/2$ and J_S is an antiferromagnetic superexchange between the core spins. J_H is the 'Hunds' coupling, and we will work in the limit $J_H/t \to \infty$. The parameters in the problem are Δ/t, J_S/t, and the carrier density n (or chemical potential μ). We assume a classical core spin, setting $|\mathbf{S}_i| = 1$, and absorb the magnitude of the spin in J_S. All our energy scales, frequency (ω) and temperature (T), etc, will be measured in units of t.

For $J_H/t \to \infty$ the fermion spin at a site is constrained to be parallel to the core spin, gaining energy $-J_H/2$, while the 'antiparallel' orientation is pushed to $+J_H/2$. Since the hopping term t_{ij} itself is spin conserving, the motion of the low energy, locally parallel spin, fermions is now controlled by nearest neighbour spin orientation. The strong magnetic coupling (J_H) generates an effective single band 'spinless fermion' problem [7], with core spin orientation dependent hopping amplitudes. We will discuss the hopping term further on, for the moment let us denote the renormalised (spin orientation dependent) hopping amplitude as $\tilde{t}$, indicative of double-exchange physics.

The $\tilde{t} - \Delta - J_S$ problem has a variety of ground states.

- In the absence of J_S, both the 'clean' and the disordered DE model has a *ferromagnetic ground state*, at all electron density, with T_c reducing with increase in Δ.
- The non disordered problem, with J_S, leads to a variety of phases [8, 9] competing with ferromagnetism. These are *ferromagnetic and A, C, G type AF phases, etc.* There could also be more exotic 'flux', 'skyrmion' or 'island' phases in some parts of parameter space. The boundaries between these phases are often first order so there are regimes of *macroscopic phase coexistence*. The specific set of possible AF phases depends on J_S.
- *Weak* disorder in the $t - J_S$ problem [10, 11] converts the regions of macroscopic phase separation into *mesoscopic phase coexistence of FM and AF clusters.*
- For some density and $\Delta - J_S$ combination, the ground state is a *spin glass*.

Although the phases above can be motivated easily, the electrical character of the ground state, or the temperature dependence of magnetic and transport properties, or the response to an applied magnetic field, are still not well understood. A comprehensive understanding of these effects within the relatively simple model in Eqn.1 would be the first step in approaching the even richer variety of phases in the manganites, where the lattice degrees of freedom are also active. This calls for a new technique, handling spatial and thermal fluctuations, the formation of clusters, and the effect of electron localisation. We propose and extensively benchmark such a real space technique in this chapter. To appreciate the need for a new method let us quickly review the current approaches to the Hamiltonian above.

3.1.1 Theoretical approaches

The approaches can be broadly classified into three categories. These are: (i) Exact variational calculations [12] at $T = 0$, and generalisation [13, 14, 15] to $T \neq 0$ via approximate mean field techniques. Let us call these methods variational mean field (VMF), for convenience. (ii) Dynamical mean field theory (DMFT) based calculations [16, 17] which map on the lattice model to an effective single site problem in a temporally fluctuating medium. Apart from a formal limit $d \to \infty$, where d is the number of spatial dimensions, there are no further approximations in the theory. (iii) Real space, finite size, Monte Carlo (MC) simulations [18, 19, 20, 21, 22] of the coupled 'spin-fermion' problem, treating the core spin as classical.

We can set a few indicators in terms of which the strength and weakness of various approximations can be judged. These are, tentatively:

1. The ability to access ground state properties.
2. Ability to handle fluctuations. and accuracy of T_c estimate.
3. The ability to access response functions: *e.g*, transport and optical properties.
4. Treatment of disorder effects: Anderson localisation and cluster coexistence.
5. Ability to handle Hubbard interactions, and quantum effects in spins and phonons.
6. Computational cost and severity of finite size effects.

Variational calculations

The variational calculations attempt a minimisation of the energy of the (clean) system, at $T = 0$, with respect to a variety of ordered spin configurations. The optimal configuration $\{\mathbf{S}_i\}_{min}$ for specified J_S, μ, etc, is accepted as the magnetic ground state. The energy calculations are relatively straightforward, since the electron motion is in a periodic background. The method has been used to map out the ground state phase diagram of DE model with AF superexchange in two and three dimension [8, 9]. The approach, however, can only be approximately implemented at finite temperature [13, 14, 15]. One has to calculate a spin distribution instead of just targeting the ground state, and estimating the energy of an electron system in a spin disordered background is non trivial. Due to the mean field character of VMF, fluctuation effects are lost and transition temperatures are somewhat overestimated. The method is focused on thermodynamic properties so there is no discussion of transport, etc, within this scheme (with one exception [13]). Disorder effects have been included, approximately [13], in some of these calculations. Variational methods can provide indication of phase coexistence [8, 9] at $T = 0$, or, approximately, at finite temperature [14, 15], but cluster coexistence in a disordered system is beyond its reach. The method has not been generalised to include quantum many body effects. Finite size effects in this approach are small and the method is relatively easy to implement.

Dynamical mean field theory

The single site nature of the DMFT approximation becomes exact in the limit of 'high dimensions'. DMFT can access both ground state and finite temperature properties, but the effective single site approximation cannot capture spatial fluctuations, or a non trivial paramagnetic phase. The 'mean field' character leads to an overestimate of T_c, and also the inability to differentiate between two and three dimensional systems. Being a Greens function based theory

DMFT can readily access response functions. However, effects like Anderson localisation or cluster coexistence, which require spatial information, cannot be accessed. The method can handle many body, Hubbard like, interactions and quantum dynamics in all the variables involved, although such calculations are quite difficult. DMFT is defined directly in the thermodynamic limit, so there are no finite size effects. The calculations are relatively easy, when quantum many body effects are not involved, and have been a major tool in exploring phenomena in the manganites.

The limitations of DMFT become apparent as we consider the more complicated phases that can arise in our model. For instance in the strong disorder problem, when there is a possibility of electron localisation, the DMFT approach cannot access the insulating phase. Neither can it access the spatially inhomogeneous nature of freezing, and the persistence of strong spin correlations above the bulk T_c. Similarly, in the problem of competing double exchange and superexchange, in the presence of weak disorder, the system breaks up into interspersed 'ferro-metallic' and 'AF-insulating' regions. A complicated variant of this coexistence effect has been extensively studied in manganite experiments [23]. The 'single site' nature of DMFT cannot access cluster coexistence, except possibly in an averaged sense. The transport and metal-insulator transitions that can occur in this situation also remain inaccessible. So, there are important *qualitative effects* beyond the reach of DMFT, in systems where spatial inhomogeneity is important.

Monte Carlo

The finite size real space approach uses the Metropolis algorithm to generate equilibrium configurations of the spins at a given temperature. Monte Carlo calculations on classical systems with short range interactions involve a cost $\mathcal{O}(zN)$ for a system update, with z being the coordination number on the lattice and N the system size. In the spin-fermion problem, however, the 'cost' of a spin update at a site has to be computed from the fermion free energy. If one uses direct diagonalisation of the Hamiltonian to accomplish this, the cost *per site* is $\mathcal{O}(N^3)$, the cost for a 'system update' is a prohibitive N^4. All this is after ignoring quantum many body effects. Current MC approaches have not been generalised to handle Hubbard like interactions.

Despite the severe computational cost, this method, which we will call ED+MC (exact diagonalisation based MC), has been successfully used to clarify several aspects of manganite physics, and DE models in general. System sizes accessible are ~ 100 at most (recent algorithms [21] have enhanced this somewhat), with $50-60$ being more typical. This method can provide an outline of the finite temperature magnetic phase diagram, reveal major spectral features, and even yield the basic signatures of cluster coexistence. However, as is obvious from the accessible N, the finite size gaps are much too large for any reasonable estimate of d.c transport properties, and the small linear dimension available, in two or three spatial dimension, allows only a preliminary glimpse of coexistence physics. The size limitation apart, the method is *exact* and comprehensive, with none of the problems of standard quantum Monte Carlo (QMC). An extension of this approach to larger system sizes would allow exploration of several unresolved issues in manganite physics. Apart from the ED based MC, 'hybrid MC' results have been reported [9, 22] for the various phases of double exchange competing with superexchange antiferromagnetism. No transport results, however, have yet been presented within this framework.

Our method, described in the next section, is developed in this spirit. It is a *real space Monte Carlo approach* with the key advantage that it avoids the iterative N^3 diagonalisation step. We extract an effective Hamiltonian for the core spins from the coupled spin-fermion problem, through a self-consistent scheme. We can work at arbitary temperature, handle strong disorder, and have better control on 'cluster physics' and transport properties due to our significantly larger system size, $N \sim 10^3$.

In the next section we describe our approximation and its computational implementation in detail. Following that we describe our results on the 'clean' DE model in two and three dimension. We will discuss results on thermodynamics, spectral features, resistivity and optical conductivity, in most of these cases, and compare with exact simulation results. We will also highlight systematically the size effects in transport and optical properties.

3.2 Method

3.2.1 The $J_H/t \rightarrow \infty$ limit

We have already written down our basic Hamiltonian in Eqn.1. The transformation and projection described in the next couple of paragraphs is well known, but we repeat them here for completeness.

Since we work at large J_H/t it is useful to 'diagonalise' the $J_H \mathbf{S}_i.\vec{\sigma}_i$ term first.The electron spin operator is $\vec{\sigma}_i = \sum_{\alpha\beta} c^{\dagger}_{i\alpha}\vec{\sigma}_{\alpha\beta}c_{i\beta}$, where the $\sigma^{\mu}_{\alpha\beta}$ are the Pauli matrices, and this 2×2 problem has eigenvalues $\pm J_H/2$. The eigenfunctions are linear combinations of the standard 'up' and 'down' z quantised fermion states at the site. The lower energy state $\gamma^{\dagger}_{il}$, a linear combination of the form $A^i_{11}c^{\dagger}_{i\uparrow} + A^i_{12}c^{\dagger}_{i\downarrow}$, is at energy $-J_H/2$ and has fermion spin parallel to the core spin $\mathbf{S}_i$. The orthogonal linear combination, $\gamma^{\dagger}_{iu}$, has fermion spin anti-parallel to the core spin and is at energy $+J_H/2$. The amplitudes A^i are standard [7].

In the γ basis, the Hunds coupling term becomes $-(J_H/2)(\gamma^{\dagger}_{il}\gamma_{il} - \gamma^{\dagger}_{iu}\gamma_{iu})$ at all sites. The intersite hopping term, however, picks up a non trivial dependence on nearest neighbour spin orientation, $t_{ij}c^{\dagger}_{i\sigma}c_{i\sigma} \rightarrow \sum_{\alpha\beta} t_{ij}g^{\alpha\beta}_{ij}\gamma^{\dagger}_{i\alpha}\gamma_{j\beta}$ where α, β refer to the u, l indices. $g^{\alpha\beta}_{ij}$ arises from the product of the two transformations at site i and site j, and we will describe its specific form later. Since the canonical transformation is local, the density operator $\sum_{\sigma} c^{\dagger}_{i\sigma}c_{i\sigma} \rightarrow (\gamma^{\dagger}_{il}\gamma_{il} + \gamma^{\dagger}_{iu}\gamma_{iu})$.

At finite J_H/t this is just a transformation from the 'lab frame' to a local axis and the 'up' and 'down' spin fermions get mapped to (l, u), but we still have to solve a mixed 'two orbital problem'. However, if $J_H/t \rightarrow \infty$ then all the 'anti-parallel' $\gamma^{\dagger}_{iu}|0\rangle$ states get projected out and we can work solely in the subspace of states created by $\gamma^{\dagger}_{il}$. In this space, the Hamiltonian assumes a simpler form:

$$\begin{aligned} H_{el} &= -t\sum_{\langle ij \rangle}(\ g_{ij}\gamma^{\dagger}_i\gamma_j + h.c\ ) + \sum_i (\epsilon_i - \mu)n_i \\ &= -t\sum_{\langle ij \rangle} f_{ij}(\ e^{i\Phi_{ij}}\gamma^{\dagger}_i\gamma_j + h.c\ ) + \sum_i (\epsilon_i - \mu)n_i \qquad (3.2) \end{aligned}$$

where we have dropped the superfluous ll label in g_{ij}, and absorbed $-J_H/2$ in the chemical potential. The hopping amplitude $g_{ij} = f_{ij}e^{i\Phi_{ij}}$ between locally aligned states, can be written in terms of the polar angle (θ_i) and azimuthal angle (ϕ_i) of the spin $\mathbf{S}_i$ as, $\cos\frac{\theta_i}{2}\cos\frac{\theta_j}{2} + \sin\frac{\theta_i}{2}\sin\frac{\theta_j}{2}e^{-i\ (\phi_i - \phi_j)}$. It is easily checked that the 'magnitude' of the overlap, $f_{ij} = \sqrt{(1 + \mathbf{S}_i.\mathbf{S}_j)/2}$, while the phase is specified by $\tan\Phi_{ij} = Im(g_{ij})/Re(g_{ij})$.

This problem can be viewed as a quadratic 'spinless fermion' problem with core spin dependent hopping amplitudes. The fermions move in the background of quenched disorder ϵ_i and 'annealed disorder' in the $\{\mathbf{S}_i\}$, where the second brackets indicate the full spin configuration. To exploit the nominally 'non interacting' structure of the fermion part we need to know the relevant spin configurations, $\{\mathbf{S}_i\}$, or, more generally, the distribution $P\{\mathbf{S}_i\}$, controlling the probability of occurence of a spin configuration.

3.2.2 Effective Hamiltonian for spins

The partition function of the system is $Z = \int \mathcal{D}\mathbf{S}_i \mathrm{Tr} e^{-\beta H}$. To extract $P\{\mathbf{S}_i\}$ note that for a system with only spin degrees of freedom, Z will have the form $\int \mathcal{D}\mathbf{S}_i e^{-\beta H\{\mathbf{S}\}}$. Comparing this with the partition function of the spin-fermion problem we can use

$$\int \mathcal{D}\mathbf{S}_i \mathrm{Tr} e^{-\beta H} \equiv \int \mathcal{D}\mathbf{S}_i e^{-\beta H_{eff}\{\mathbf{S}\}}$$

from which it follows that

$$\begin{aligned} H_{eff}\{\mathbf{S}_i\} &= -\frac{1}{\beta}\log \mathrm{Tr} e^{-\beta H} \\ P\{\mathbf{S}_i\} &\propto e^{-H_{eff}\{\mathbf{S}_i\}} \end{aligned} \tag{3.3}$$

The trace is over the fermion degrees of freedom. In our case

$$H_{eff} = -\frac{1}{\beta}\log \mathrm{Tr} e^{-\beta H_{el}} + J_S \sum_{\langle ij \rangle} \mathbf{S}_i.\mathbf{S}_j \tag{3.4}$$

The principal difficulty in a simulation, and quite generally in spin-fermion problems, is in evaluating the first term on the r.h.s above for an *arbitrary spin configuration*. This is the origin of the N^3 factor in the exact MC. Our key proposal, whose analytic and numerical justification we provide later, is

$$-\frac{1}{\beta}\log \mathrm{Tr} e^{-\beta H_{el}} \approx -\sum_{\langle ij \rangle} D_{ij} f_{ij} \tag{3.5}$$

where D_{ij} is an effective 'exchange constant' to be determined as follows. Define the operator $\hat{\Gamma}_{ij} = (e^{i\Phi_{ij}}\gamma_i^\dagger \gamma_j + h.c)$. This enters the 'hopping' part of the electron Hamiltonian. In any specified spin configuration $\{f, \Phi\}$ we can calculate the correlation function $D_{ij}\{f, \Phi\} = Z_{el}^{-1} \mathrm{Tr} \hat{\Gamma}_{ij} e^{-\beta H_{el}}$, where Z_{el} is the electronic partition function in the specified background. The exchange that finally enters H_{eff} is the average of $D_{ij}\{f, \Phi\}$ over the assumed equilibrium distribution, *i.e*: $D_{ij} = \int \mathcal{D}f \mathcal{D}\Phi P\{f, \Phi\} D_{ij}\{f, \Phi\}$ where we denote a spin configuration interchangeably by $\{f, \Phi\}$ or $\{\mathbf{S}\}$. Qualitatively, the 'effective exchange' is determined as the thermal average of a fermion correlator over the assumed equilibrium distribution. Let us bring together the equations for ready reference.

$$\begin{aligned} H_{el} &= -t \sum_{\langle ij \rangle} f_{ij}\hat{\Gamma}_{ij} + \sum_i (\epsilon_i - \mu) n_i \\ \hat{\Gamma}_{ij} &= (e^{i\Phi_{ij}}\gamma_i^\dagger \gamma_j + h.c) \\ f_{ij} &= \sqrt{(1 + \mathbf{S}_i.\mathbf{S}_j)/2} \\ H_{eff}\{\mathbf{S}\} &= -\frac{1}{\beta}\log \mathrm{Tr} e^{-\beta H_{el}} + J_S \sum_{\langle ij \rangle} \mathbf{S}_i.\mathbf{S}_j \end{aligned}$$

$$\begin{aligned} &\approx& -\sum_{\langle ij\rangle} D_{ij} f_{ij} + J_S \sum_{\langle ij\rangle} \mathbf{S}_i.\mathbf{S}_j \\ D_{ij} &=& \int \mathcal{D}f\mathcal{D}\Phi e^{-\beta H_{eff}\{S\}} D_{ij}\{f,\Phi\} \\ D_{ij}\{f,\Phi\} &=& Z_{el}^{-1} Tr \hat{\Gamma}_{ij} e^{-\beta H_{el}} \end{aligned} \quad (3.6)$$

The ED+MC approach 'solves' for physical properties by using the first four equations above: equilibriating the spin system by using H_{eff}, which itself involves a solution of the Schrodinger equation for the electrons.

Our method approximates the 'exact' H_{eff} by the form specified in the fifth equation, and *computes an exchange* rather than equilibrium configurations themselves, by fermion diagonalisation. The sixth and seventh equation indicate how the 'loop' is closed.We will refer to this method as Self Consistent Renormalisation (SCR) or H_{eff} scheme, throuout this thesis.

This nonlinear integral equation for the D_{ij} is solved to construct the 'classical spin model' for a set of electronic parameters, disorder realisation, and temperature. Although the assumption about H_{eff} seems 'obvious', and in fact something similar, but simpler, had been explored early on by Kubo and Ohata [4], and recently by Calderon and Brey [19], the power of the method becomes apparent in disordered systems or in the presence of competing interactions. In these cases the solutions D_{ij} can be spatially strongly inhomogeneous, and dramatically temperature dependent. The properties of such systems are far from obvious.

The equilibrium thermal average of any fermion operator, or correlation function, $\hat{O}$, can now be computed using the self-consistent distribution as:

$$\langle\langle \hat{O} \rangle\rangle = \int \mathcal{D}\{\mathbf{S}\} P\{\mathbf{S}\} O(\mathbf{S}) \quad (3.7)$$

The average $O(\mathbf{S})$ is computed on a spin configuration $\{\mathbf{S}_i\}$, with the configurations themselves picked according to the effective Boltzmann weight $\propto e^{-\beta H_{eff}}$.

We have not written the equation for μ. Since we would typically want to work at fixed density rather than fixed chemical potential, we employ the procedure above to calculate n and iterate μ till the 'target' density is obtained. In actual implementation, discussed later, the μ 'loop' and the D_{ij} 'loop' run simultaneously. We next discuss the analytic underpinning of our method before moving to numerical results.

3.2.3 Analytic limits

The central problem in DE models is construction of an energy functional for arbitrary spin configurations $\{f, \Phi\}$. This information is contained in the fermion free energy, $-T \log Tr e^{-\beta H_{el}}$ as we have seen. We study two limits below, where the leading effects are well captured by our effective Hamiltonian.

Low temperature

If we ignore disorder and AF coupling, for simplicity, and if the free energy of the fermions can be approximated by the internal energy, then $D_{ij}\{f,\Phi\}$ contains the necessary information about the energy of *any spin configuration*: $\mathcal{E}\{f,\Phi\} \equiv H_{eff}\{f,\Phi\} = \sum_{ij} D_{ij}\{f,\Phi\} f_{ij}$. The *configuration dependent* correlation function, however, is hard to calculate, since it requires a solution of the Schrodinger equation for each spin configuration.

At low temperature, as the spins gradually randomise, the system explores configurations $\{f,\Phi\}$ near the ground state in the free energy landscape. The relevant $D_{ij}\{f,\Phi\} \sim$

$D^0_{ij} + \delta D_{ij}\{f, \Phi\}$, where D^0 is the 'exchange' computed on the ground state, and δD is the variation. At low T, such that the relevant $\delta D \ll D^0$, we can neglect the variation, δD, between configurations, and the 'effective Hamiltonian' assumes the form:

$$\lim_{T\to 0} H_{eff} \sim -\sum_{\langle ij\rangle} D^0_{ij} f_{ij} = -\sum_{\langle ij\rangle} D^0_{ij} \sqrt{(1 + \mathbf{S}_i.\mathbf{S}_j)/2}$$

As we will see in the simulations this approximation is remarkably good in the simple DE model almost upto $T_c/2$. At higher T the 'renormalisation' of D becomes important.

High temperature

For $T_c/T \ll 1$, cumulant expansion yields an asymptotically exact effective Hamiltonian:

$$H_{eff} \sim \lim_{\beta t\to 0} -\frac{1}{\beta}\ln \mathrm{Tr}(1 + \beta H + \frac{1}{2}\beta^2 H^2 + ..)$$

The leading contribution from this is:

$$H^{high\ T}_{eff} \sim -n(1-n)\beta t^2 \sum_{\langle ij\rangle} f^2_{ij}$$

This apparently has a structure different from that of our H_{eff}, and additionally an 'effective coupling' falling off as $1/T$. In fact our coupling D has the same form, as can be checked by evaluating $\langle\langle \hat{\Gamma}_{ij}\rangle\rangle$ in a high temperature expansion. This quantity also depends on $n(1-n)$, to allow hopping, and falls off as $1/T$ since it is non local. The *self-consistent* calculation of the effective exchange, now based on the high temperature phase rather than the ground state, ensures that the leading contribution to the energy is well captured. The physical consequence of the $1/T$ effective exchange is that the susceptibility of the DE model does not have the Curie-Weiss form that one expects for Heisenberg like models [24].

The next order in series expansion will generate terms of the form:

$$\sum_{ijkl} f_{ij} f_{jk} f_{kl} f_{li} e^{i(\phi_{ij}+\phi_{jk}+..)},$$

summed over the minimal plaquette. Higher powers in βt involve longer range excursion of the fermions, but the limited data available from exact simulations suggests that the critical properties of double exchange are similar to that of short range spin models.

Although the procedure above can be extended to extract an 'exact' effective Hamiltonian to high order in βt, we know of no such attempt. The only series expansion results available are on the $S = 1/2$ model, directly calculating thermodynamic properties [25].

3.2.4 Monte Carlo implementation

Since the ground state of the system is often not known it is usual to start from high temperature and follow the sequence below in generating the effective Hamiltonian and studying equilibrium properties.

(i) We start at high temperature, $T \gg T_c$, assuming some $D^n_{ij}(T)$, where n is the iteration index. and 'equilibriate' the system with this assumed effective Hamiltonian (not yet self-consistent), (ii) We compute the average $\langle\langle e^{i\Phi_{ij}}\gamma^\dagger_i\gamma_j + h.c\rangle\rangle$ over these (pseudo) equilibrium configurations. This generates $D^{n+1}_{ij}(T)$. (iii) Compare the generated exchange with the assumed exchange at each bond. Accept if within tolerance. If converged, then D_{ij} represents the correct 'exchange' at that temperature. Else, replace D^{n}_{ij} by D^{n+1}_{ij}. (iv) At each temperature and iteration, adjust μ as necessary to keep n constant.

At convergence fermion properties can be calculated and averaged over equilibrium MC configurations of the spin model. For a disordered system $(\Delta \neq 0)$, the thermal cycle above has to be repeated for each realisation of disorder. In the clean problem, translation invariance forces the exchange to be uniform at all bonds, while $\Delta \neq 0$ generates a bond disordered spin model.

The computational effort needed in the ED+MC approach is $\propto N_{MC} \times N^4$, at each temperature, where N_{MC} is the number of MC sweeps $(10^3 - 10^4)$, and N the size of the system (actually the Hilbert space dimension). As we have mentioned before, current resources allow $N_{max} \sim 100$. Within our H_{eff} scheme the MC configurations are generated using a short range spin model, with cost $\mathcal{O}(N)$. The actual cost is in determining the exchange: this is $\propto N_{iter} \times N_{av} \times N^3$, where N_{iter} is the number of iterations needed to get a converged solution, with $\sim$ 10% accuracy per bond, and N_{av} is the averaging needed *per iteration* for generating a reasonable 'equilibrium average'. Typically $N_{iter} \sim 4$ and $N_{av} \sim 50$.

We can roughly compare the computational cost of ED+MC with the H_{eff} scheme. For ED+MC, the time required is, $\tau_N \sim N_{MC} \times N^4$ at a given temperature. For the H_{eff} scheme, $\tau_N \sim N_{iter} \times N_{av} \times N^3$. Putting in the numbers, if resources allow $N \sim 100$ for the ED+MC approach, the same resource will allow $N \sim 1000$ within the H_{eff} scheme. In terms of computation time, H_{eff} is no more expensive than standard 'disorder average' in electronic systems.

3.2.5 Physical properties at equilibrium

The major physical properties we compute at equilibrium are optical conductivity and d.c resistivity, the density of states (DOS), and the magnetic structure factor.

(i) We have already discussed our transport calculation method in the previous chapter. This technique is used for accessing σ_{dc} and $\sigma(\omega)$. (ii) Each equilibrium magnetic configuration leads to a 'DOS' of the form $\sum_{\alpha} \delta(\omega - \epsilon_{\alpha})$, where ϵ_{α} are the single particle eigenvalues in that background. The thermally averaged DOS that we show involves a Lorentzian broadening of each δ function, as indicated below.

$$N(\omega) \approx \frac{1}{N_{eq}} \sum_{eq} \sum_{\alpha} \frac{(\Gamma/\pi)}{(\omega - \epsilon_{\alpha})^2 + \Gamma^2} \tag{3.8}$$

The sum runs over the eigenvalues obtained in any spin configuration, and summed over equilibrium configurations. We use $\Gamma \sim 0.1$ in our results, although much smaller Γ would still give a smooth spectra at high T. (iii) The magnetic structure factor is calculated as

$$S(\mathbf{Q}) = \frac{1}{N_{eq} N^2} \sum_{eq} \sum_{ij} \langle \mathbf{S}_i . \mathbf{S}_j \rangle e^{i\mathbf{Q}.(\mathbf{r}_i - \mathbf{r}_j)} \tag{3.9}$$

3.3 Results

In this section we provide a comprehensive comparison of results based on the 'exact' scheme (ED+MC) and our effective Hamiltonian approach, for the 'clean' DE model in two and three dimension, and extend the study to large sizes using the H_{eff} scheme. The system is translation invariant, there are no competing interactions, and the low temperature phase is a ferromagnet.

3.3.1 Magnetism and thermodynamics

We begin with a comparison of the magnetisation, $m(T)$, obtained via the exact and approximate schemes on 8×8 lattices in 2d, and 4^3 systems in 3d, with periodic boundary condition (PBC) in both directions. Fig.1 compares the $m(T)$ obtained via the two schemes at three electron densities.

Note at the outset that both the DE model and our H_{eff} are $O(3)$ symmetric and are *not* expected to have long range order at finite T in 2d (in an infinite system). However, as has been demonstrated in the case of the two dimensional classical Heisenberg model [26], $O(3)$ models have *exponentially large* correlation length at low temperature in 2d. For a nearest neighbour classical Heisenberg model with $|\mathbf{S}_i| = 1$, and exchange J, the low T correlation length $\xi(T) \sim 0.02e^{2\pi J/T}$. So, for $T \ll J$ even large finite lattices would look 'fully polarised' and one would need to access exponentially large sizes to see the destruction of long range order. This allows us to define a (weakly size dependent) 'characteristic temperature' $T_{ch}(n)$ for the DE model which marks the crossover from paramagnetic to a nominally 'ordered' phase. The true ordering temperature of strongly anisotropic DE systems, *e.g*, the layered manganites, which the planar model mimics, would be determined by the interplane coupling, but the in plane transport would be dictated mainly by the 2d fluctuations as encountered here.

The difference between the two schemes, Fig.1.(a) is most prominent at the highest density, $n = 0.41$, where the T_{ch} inferred from these small size calculations differ by $15\% - 20\%$. At lower density the difference is still visible but much smaller. We have indicated the T_{ch} scales inferred from the two schemes in the inset in Fig.1.(a) The difference between the two schemes is usually largest in clean high density systems, as we will see also in the three dimensional case. However, over the entire density range, the maximum deviation is $\sim 20\%$.

Notice that at all n, the low temperature $m(T)$ obtained via H_{eff} corresponds almost exactly with results based on ED+MC. This works upto $\sim T_{ch}/2$. The high temperature result within the two schemes is also in close correpondence but that is better illustrated in the thermodynamic data, Fig.2, which we will discuss in the 3d context.

Fig.1.(b) shows the results on magnetisation in the three dimensional problem at three densities, comparing results based on ED+MC and H_{eff}. As in two dimension the difference in the estimated T_c is greatest near the band center, being $\sim 15\% - 20\%$, the correspondence improving as we move to $n \lesssim 0.2$. As before, the exact and approximate $m(T)$ match at low T for all densities.

Fig.2(a) which shows the thermodynamic indicators in the 3d case reveals that D_{ij} itself is virtually indistinguishable in the two schemes. The correlation $D_{ij} = \langle\langle \hat{\Gamma}_{ij} \rangle\rangle$ can be evaluated as an equilibrium average in an exact simulation also, although there it does not feed back into the calculation. The match between the D's computed in two different schemes, and across the density range, suggests that the difference in $m(T)$ seen near half-filling is not due to different numerical values of D, but the assumed *form* of H_{eff}. We either need a more sophisticated definition of the finite temperature D, or a different form of H_{eff} to bring the high density results of H_{eff} in closer correspondence with ED+MC. Notice that the D's are only weakly temperature dependent and the $m(T)$ at low temperature could have been obtained by setting $D(T) = D(0)$. In fact over the temperature range $0 - T_c$ the qualitative physics can be accessed without the thermal 'renormalisation' of the exchange. However, for $T \gg T_c$ the renormalisation is important, as suggested earlier by the high temperature expansion.

The results on all thermodynamic indicators, $D(T)$, $E(T)$, $\mu(T)$ and $E_b(T)$, Fig.2, show the close correspondence between results of the exact and approximate scheme. The D's are almost temperature independent in the range $0 - T_c$ and hardly distinguishable between ED+MC and H_{eff}, suggesting that effects beyond our effective Hamiltonian $-D \sum f_{ij}$ is

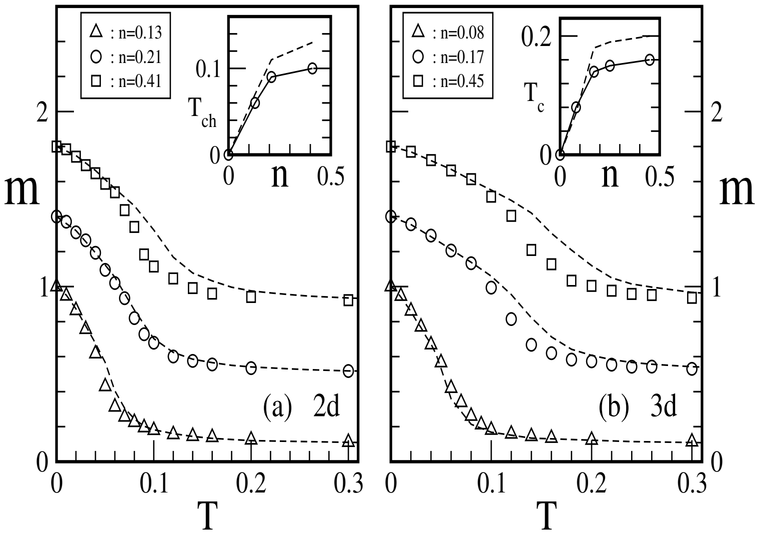

Figure 3.1: Magnetism in the 2 and 3 dimensions, open symbols are for ED+MC, the dotted lines indicate the SCR results.

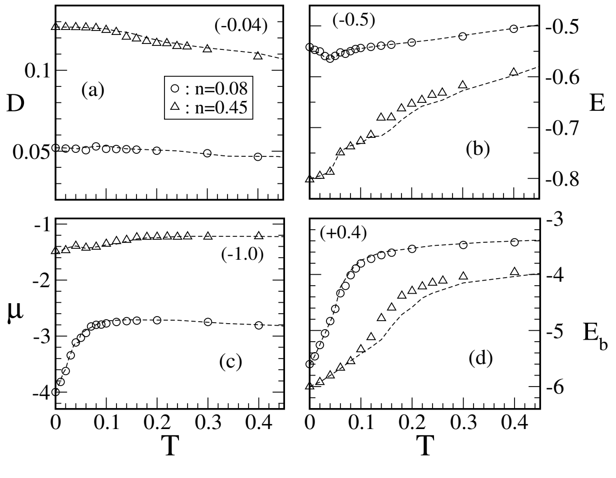

Figure 3.2: Comparing thermodynamic indicators between ED-MC and the H_{eff} scheme in 3d: (a) effective exchange, (b) internal energy, (c) chemical potential and (d) band edge. Displayed value is actual value + shift. System size $4 \times 6 \times 4$. Open symbols: ED-MC, dotted lines: SCR.

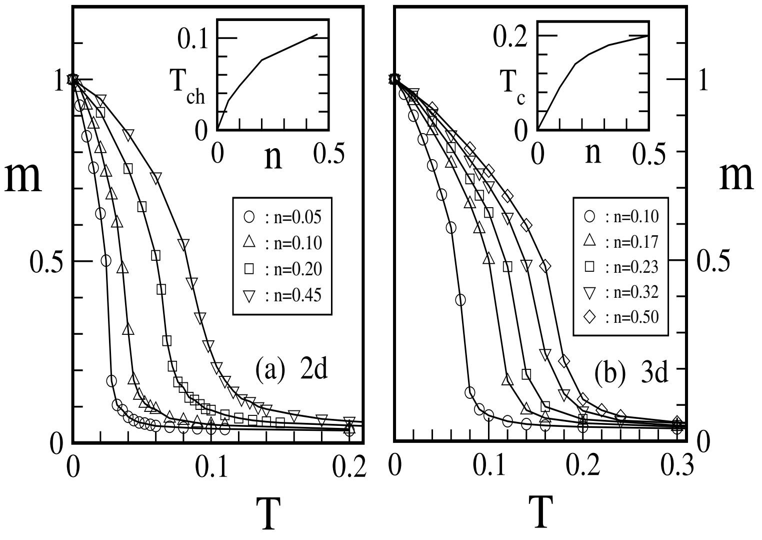

Figure 3.3: Magnetisation based on H_{eff} in (a)30×30 and (b)$10 \times 10 \times 10$ systems. Insets show the characteristic temperature scales inferred from the $m(T)$

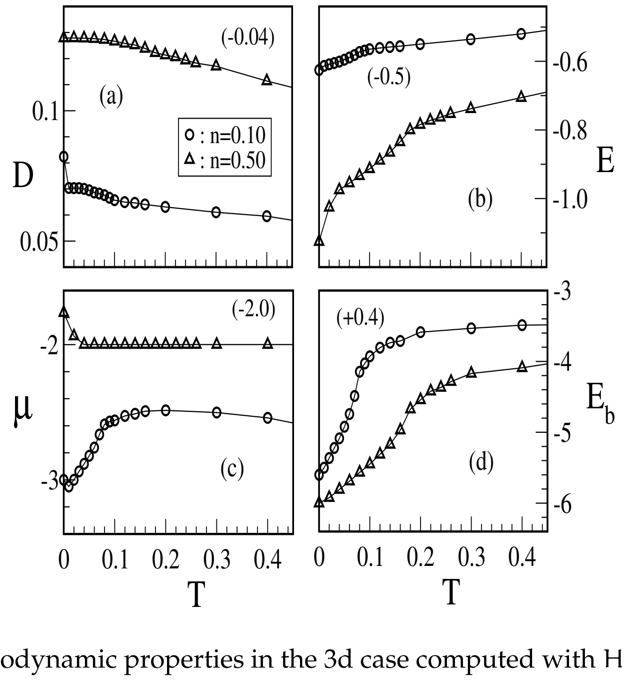

Figure 3.4: Thermodynamic properties in the 3d case computed with H_{eff}, $10 \times 10 \times 10$.

needed to accurately describe the magnetic transition at the band center.

We extend the H_{eff} scheme to large system size, and study the magnetism in 32^2 and 10^3 lattices. Fig.3 shows the results on $m(T)$, and the inset shows the T_c inferred from these simulations. The maximum T_c, occuring at band center is ~ 0.2 which, with $t \sim (100-150)$meV, will be in the range $200-300$K. These numbers are typical of high electron density Hunds coupled systems, and are in the right ballpark when compared to the manganites.

Fig.4 shows the thermodynamic indicators computed within the H_{eff} scheme on 10^3 in 3d. The strong T dependence in μ and E_b, seen also at small sizes, arise from the 'band narrowing' effect of spin disorder which reduces the mean hopping amplitude with increasing temperature.

3.3.2 Density of states

Fig.5 shows the density of states (DOS) computed at $n = 0.3$, four temperatures, and for a small, 4^3, and a large, 10^3, system. The mean level spacing at high temperature (where the spins are completely disordered) is $\sim 12/L^3$ which is ~ 0.01 at $L = 10$ and ~ 0.18 at $L = 4$. For $T \rightarrow 0$, the polarised ferromagnetic state leads to large degeneracy and the level spacings could be more than 10 times larger than the high temperature value. We have broadened all δ functions by $\Gamma = 0.1$, so that the high temperature $L = 4$ spectra looks reasonable. With this broadening the $L = 10$ data looks reasonable even below T_c.

This comparison highlights the unreliability of small size data in inferring spectral features over most of the interesting temperature range. Small sizes can often provide reasonable results on energetics, but on spectral features and, more importantly, on low frequency transport, they are completely unreliable.

3.3.3 Optical properties

Fig.6 shows the optical conductivity, $\sigma(\omega)$ The optical conductivity is a vital probe of charge dynamics in the system. Our data in the main panel, Fig.6, is for a $8 \times 8 \times 8$ geometry. At the lowest temperature there is an artificial 'hump' in $\sigma(\omega)$ which we think arises because the polarised three dimensional system has large degeneracy, and finite size effects are stronger than in two dimension. Nevertheless, there are some notable features in $\sigma(\omega)$, (i) the conductivity is Drude like, (ii) there is rapid reduction in low frequency spectral weight with increasing temperature, with some transfer to high frequency, (iii) the weight in $\sigma(\omega)$ is not conserved with increasing temperature, the loss is related to the suppression of kinetic energy with increasing spin disorder.

3.3.4 Resistivity

Finally, we look at the resistivity which, surprisingly, has seen little discussion. Fig.7 shows the correlation between the ferromagnet to paramagnet transition and the rise in $\rho(T)$. We have normalised $\rho(T)$ by the value at $T = 0.4$, the 'absolute' resistivity is shown in Fig.7.(c)-(d). Unlike mean field treatments which treat the paramagnetic phase as completely 'uncorrelated' and would yield a 'flat' resistivity for $T > T_{ch}$, there is a significant increase in $\rho(T)$ with rising temperature in the 'paramagnetic' phase as the short range spin correlation is gradually lost and the system heads towards the fully spin disordered phase. The general rise in $\rho(T)$ in the paramagnetic phase is not specific to two dimension, but surprisingly in 2d most of the rise seems to occur after the drop in $m(T)$, rather than across T_{ch} as one sees in three dimension. We will discuss the 'critical behaviour' of the resistivity and thermodynamic response in two dimensional (layered) and three dimensional systems elsewhere.

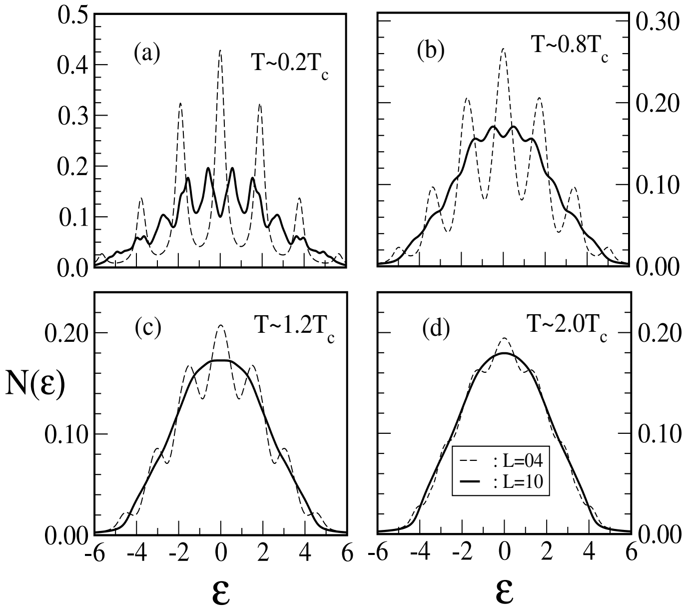

Figure 3.5: DOS in three dimension. Results on H_{eff} with $4 \times 6 \times 4$ and $10 \times 10 \times 10$ geometry, $n = 0.3$.

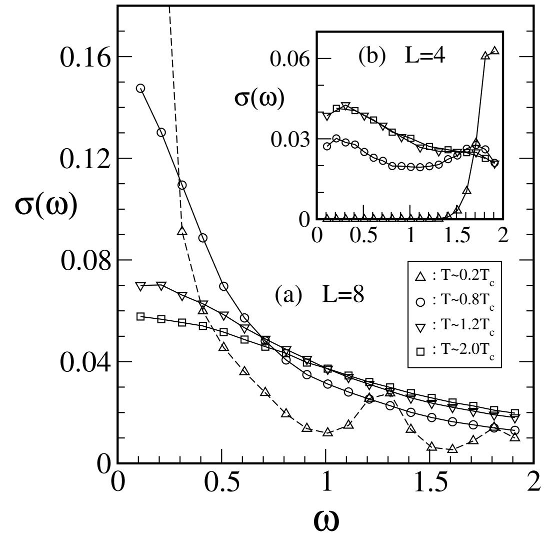

Figure 3.6: Optical conductivity based on H_{eff} in three dimension. System size $4 \times 4 \times 4$ (inset) and $8 \times 8 \times 8$ (main panel), $n = 0.3$

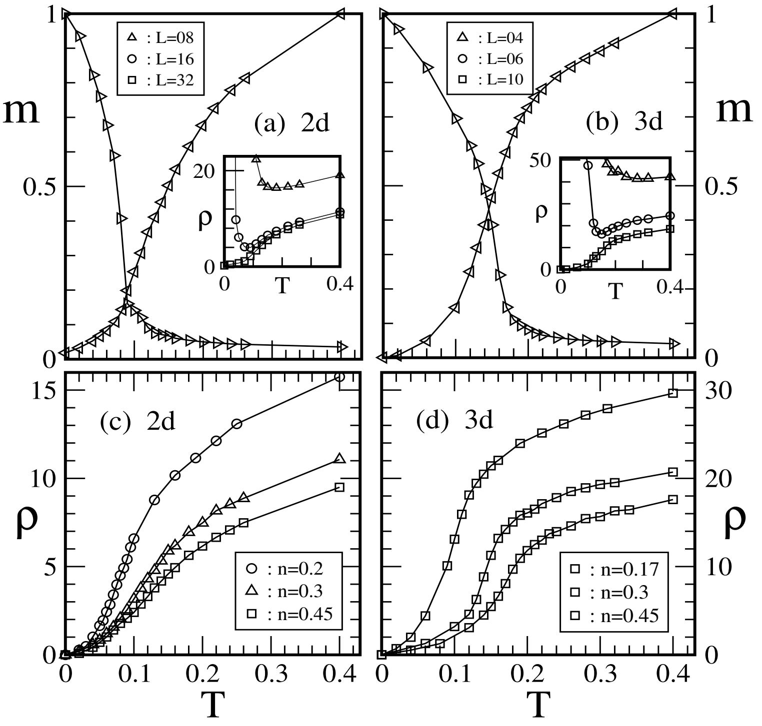

Figure 3.7: Magnetisation and (normalised) 'resistivity' in (a)2d and (b)3d. Insets to (a) and (b) show the size dependence. (c)32×32 and (d)$10 \times 10 \times 10$ look at the density dependence of resistivity.

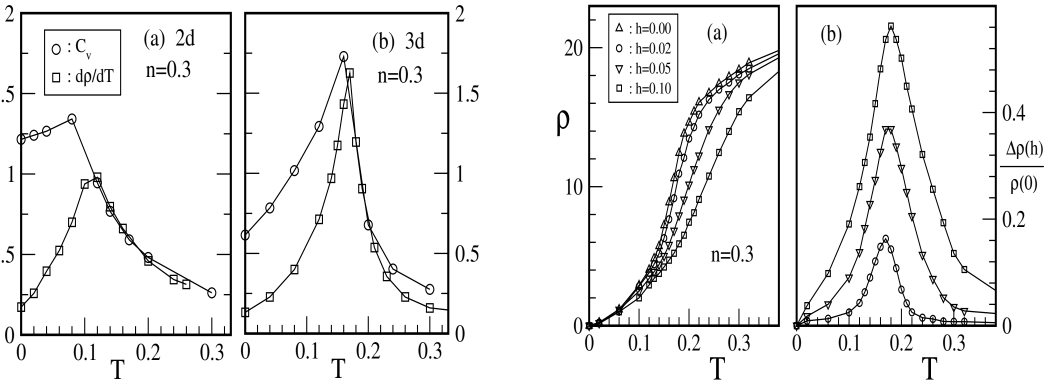

Figure 3.8: Left: Correlation between specific heat and $d\rho/dT$ Right: Magnetoresistance in the three dimensions. The parameter values used are indicated in the figure itself.

For a check on the reliability of the computed $\rho(T)$ the inset in Fig.7.(a) shows the 'resistivity' computed on $L \times L$ geometry for $L = 8, 16, 24, 32$ across the full temperature range. The $L = 8$ result has the same problem that we discussed in the context of $\sigma(\omega)$, it essentially behaves as an 'insulator' at low T due to the finite size gap. The $L = 16$ data has similar upturn, but at a lower temperature. The data at $L = 24$ (not shown) and $L = 32$ are stable down to $T \sim 0.02$ and almost coincide, suggesting that except at very low temperature, results on these sizes are representative of bulk transport.

The resistivity across the band is shown in Fig.7.(c)-(d). The three densities show similar overall temperature dependence, and the 'high temperature' values are around 10. Our conductivity results are in units of $(\pi e^2)/\hbar$ in 2d.

The resistivity in the three dimensional case differs from two dimensional case in that the major rise in $\rho(T)$ occurs around T_c in the 3d case, while it occurs *beyond* T_{ch} in the 2d case. Fig.7.(b) shows $m(T)$ correlated with the normalised $\rho(T)$, and the rise is reminiscent of the Fisher-Langer result [27] in *weak coupling* electron-spin systems.

The inset in Fig.7.(b) shows the stability of the transport result for $L \gtrsim 8$, and the unreliability for $L \sim 4$. Fig.7.(c)-(d), shows the absolute resistivity for a few densities. The 'high temperature' resistivity, at $T \sim 3T_c$ is approximately $15 - 25$, in the density range shown, which in real units would be $\sim (1 - 2) m\Omega$cm, roughly the high T resistivity of $La_{1-x}Sr_xMnO_3$ for $x \gtrsim 0.4$.

The left panel of fig.8. shows the correlation between $d\rho/dT$ and the specific heat. The $d\rho/dT$ seems to match C_v very well for $T > T_c$, which is consistent with the Fisher-Langer result. The magnetoresistence is shown in the right panel of fig.8. for both $2d$ and $3d$. The response to the magnetic field is strongest in the vicinity of T_c.

To conclude this section we have presented comprehensive data on magnetism, thermodynamics, spectral features, transport, and optics in the DE model in two and three dimension retaining the correlated nature of spin fluctuations and implementing the Kubo formula.

3.4 Conclusion

In this chapter we have dicussed only the ferromagnetic phase of the DE model. In this case the complicated consistency and thermal renormalisation involved in our scheme are not crucial for a qualitative understanding. However, when we move to disordered systems, or non ferromagnetic ground states, or the regime of multiphase coexistence, the full power of a 'bond disordered' effective Hamiltonian, with non trivial spatial correlation between the bonds, becomes apparent. For the 'clean' ferromagnetic case one may try to 'improve' the self-consistency scheme to obtain better correspondence [19, 28] with ED+MC results. However, given the complexity of the current scheme, and the range of possibilities that it offers, we think it is more important to exploit the present scheme to resolve the outstanding *qualitative issues* first. Finally, although the entire scheme is presently implemented numerically, it would be useful to make analytic approximations within this framework to create greater qualitative understanding.

Bibliography

[1] C. Zener, Phys. Rev. **82**, 403 (1951).

[2] P. W. Anderson and H. Hasegawa, Phys. Rev. **100**, 675 (1955).

[3] P. G. de Gennes, Phys. Rev. **118**, 141 (1960).

[4] K. Kubo and N. Ohata, J. Phys. Soc. Jpn **33**, 21 (1972).

[5] A. P. Ramirez, J. Phys. Condens Matter **9**, 8171 (1997), E. Dagotto *et al.*, : Phys Rep **344**, 1 (2001), *Colossal Magnetoresistive Oxides*, Ed. Y. Tokura, Gordon & Breach (2000), M. B. Salamon and M. Jaime, Rev. Mod. Phys. **73**, 583 (2001).

[6] See article by A. J. Millis in *Colossal Magnetoresistive Oxides*, Ed. Y. Tokura, Gordon & Breach (2000).

[7] E. Muller-Hartmann and E. Dagotto, Phys. Rev. **B 54**, R6819 (1996).

[8] H. Aliaga *et al.*, Phys. Rev. **B 64**, 024422 (2001).

[9] J. Alonso *et al.*, Phys. Rev. **B 64**, 054408 (2001).

[10] A. Moreo *et al.*, Phys. Rev. Lett. **84**, 5568 (2000), J. Burgy *et al.*, Phys. Rev. Lett. **87**, 277202 (2001).

[11] Sanjeev Kumar and Pinaki Majumdar, Phys. Rev. Lett. **92**, 126602 (2004).

[12] M. Yamanaka *et al.*, Phys. Rev. Lett. **81**, 5604 (1998).

[13] E. E. Narimanov and C. M. Varma, Phys. Rev. **B 65**, 024429 (2002).

[14] D. I. Golosov, Phys. Rev. **B 58**, 8617 (1998).

[15] J. A. Alonso, *et al.*, Phys. Rev. **B 63**, 054411 (2001).

[16] N. Furukawa, J. Phys. Soc. Jpn. **63**, 3214 (1995).

[17] K. Nagai *et al.*, J. Phys. Soc. Jpn. **69**, 1837 (2000).

[18] S. Yunoki, *et al.*, Phys. Rev. Lett. **80**, 845 (1998), E. Dagotto, *et al.*, Phys. Rev. **B 58**, 6414 (1998).

[19] M. J. Calderon and L. Brey, Phys. Rev. **B 58**, 3286 (1998).

[20] Y. Motome and N. Furukawa, J. Phys. Soc. Jpn. **68**, 3853 (1999), J. Phys. Soc. Jpn. **69**, 3785 (2000).

[21] Y. Motome and N. Furukawa, preprint cond-mat 0304551.

[22] J. L. Alonso *et al.*, Nucl. Phys. **B 596**, 587 (2001). The hybrid MC technique discussed by the authors can apparently access sizes $\sim 16^3$, far beyond the reach of ED based techniques. However, there does not seem to be any follow up in disordered problems.

[23] M. Uehara, *et al.*, Nature, **399**, 560 (1999).

[24] R. S. Fishman and M. Jarrell, Phys. Rev. **B 67**, 100403(R) (2003).

[25] H. Roder *et al.*, Phys. Rev. **B 56**, 5084 (1997).

[26] M. Takahashi, Phys. Rev. **B 36**, 3791 (1987).

[27] M. E. Fisher and J. S. Langer, Phys. Rev. Lett. **20**, 665 (1968).

[28] I. V. Solovyev, Phys. Rev. **B 67**, 014412 (2003).

Chapter 4

Anderson-Mott Transition in α-GdSi

Chapter Summary: A zero temperature Anderson-Mott transition driven by spin disorder can be 'tuned' by an applied magnetic field to achieve colossal magnetoconductance. Usually this is not possible since spin disorder by itself cannot localise a high density electron system. However, the presence of strong structural disorder can realise this situation, self consistently generating a disordered magnetic ground state. In this chapter we explore such a model, constructed to understand amorphous GdSi, and highlight the emergence of a spin glass phase, Anderson-Mott signatures in transport and tunneling spectra, and unusual magneto-optical conductivity. We solve a disordered strong coupling fermion-spin-lattice problem, essentially exactly on finite systems, and account for the qualitative features observed in magnetism, transport, and the optical spectra in this system. Some of the results discussed here have been published in Phys. Rev. Lett. **90**, 237202 (2003).

4.1 Introduction

The role of disorder in electronic systems is an enduring theme in condensed matter physics [1, 2, 3, 4]. Structural disorder leads to localisation of electronic states and, in a three dimensional system, all electronic states would be localised [3] if the disorder, 'Δ' say, were greater than a critical value (Δ_c). For weaker disorder, $\Delta < \Delta_c$, only states *beyond* an energy $\epsilon_c(\Delta)$ of the band center, *i.e* in the band tails, are localised. A system is metallic or insulating depending on whether the Fermi level, ϵ_F, is above or below this 'mobility edge' ϵ_c. Variation in electron density, and hence ϵ_F, can drive a system through the insulator-metal transition (IMT). This is the basic scenario for the 'Anderson transition' in a non interacting electron system [3, 4].

Doped semiconductors [5] have served as a laboratory for studying disorder effects since they allow systematic control of the carrier density. The IMT has been studied in doped crystalline systems, the most famous example being phosphorus doped silicon [6] (Si:P), and less extensively in amorphous semiconductors [7]. In experimental systems, however, the phenomena of localisation is complicated by electron-electron (EE) interaction effects which become very pronounced close to the IMT [8]. In amorphous systems, for example, there are clear signatures of interaction effects in the density of states and the conductivity close to the IMT. The interplay of disorder and interaction effects near the IMT is not completely understood [9, 10] and continues to be an area of active research.

The introduction of magnetic moments in a ‘disordered’ system brings in new phenomena. The effects are well understood in crystalline semiconductors [11, 12], where the disorder is weak and the relevant regime is of low carrier density. In these systems, electrons are trapped in the potential fluctuations and polarise the magnetic moments in their neighbourhood. This leads to a gain in exchange energy, and tends to enhance the localisation of the carrier. The net localising effect in these systems, therefore, arises from a combination of (i) on site disorder; a ‘single particle’ effect, and (ii) ‘bound state’ formation between the electron and the magnetic moments; a ‘many body’ effect. The composite object, a (trapped) electron and the polarised spins in its vicinity, is called a ‘spin polaron’. Since the IMT in these systems occurs at a carrier density $\sim 10^{-5}$ (per unit cell), the picture of non overlapping, uncorrelated, spin polarons is adequate. The interesting difference between these systems and their non magnetic counterparts lies in the response to a magnetic field. An applied field globally aligns the magnetic moments, reduces the polaron binding energy, and tunes the ‘magnetic component’ of localisation. The change in activation energy (or mobility) of the carriers can lead to *enormous magnetoresistance* [13, 14]. These systems have been known to exhibit ‘colossal magnetoresistance’ (CMR) much before such effects were observed in the manganites.

Recent experiments [15, 16, 17, 18, 19] on amorphous (a)-GdSi reveal that doping magnetic moments in an *amorphous* system combines the richness, and complication, of the traditional IMT in amorphous semiconductors [7] with the physics of ‘CMR’. In addition a disordered magnetic state, a spin glass, with rather unusual properties emerges at low temperature. This combination of an IMT, in a high carrier density system, with CMR, and a spin glass ground state is probably unique to GdSi. We will discuss these experiments in the next section. The essential phenomena in these systems seems to be:

- Electron localisation due to strong disorder in the amorphous structure.

- Indirect exchange interaction between the doped moments, mediated by the electrons, leading to a spin glass state.

- Feedback of the spin background on the electronic system, via ‘spin disorder’, tending to enhance electron localisation.

- Control of the ‘spin disorder’ by a magnetic field, h, leading to large negative magnetoresistance close to the critical density.

- Large transfer of spectral weight [19] from high to low frequency in the optical conductivity, is response to a magnetic field (in GdSi) or increase in temperature.

- In addition the following effects, characteristic of the interplay of disorder and EE interactions near an IMT are also seen: (i) a correlation gap in the density of states, (ii) $\sqrt{T}$ dependence in the the low temperature conductivity, and, possibly, (iii) local moment formation’ in the electron system.

Unlike the case of crystalline magnetic semiconductors, where the concept of isolated ‘bound magnetic polarons’ [11, 12] seems to suffice, we do not have an understanding of a *high density of electrons in the background of strong disorder, interacting with randomly located magnetic moments and with each other*. Scenarios in terms of a canonical “Anderson transition”, or isolated polarons, or model spin glasses, do not suffice, and the interplay of these effects is what we study in this chapter.

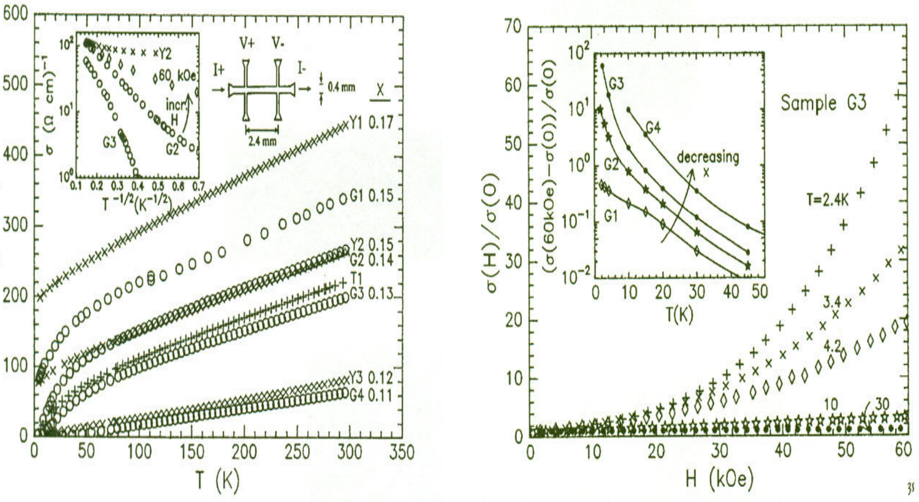

Figure 4.1: Left panel: Temperature dependence of the conductivity for a-GdSi (samples G1-G4) a-YSi (samples Y1-Y3) and a-TbSi. Composition is shown for each, uncertainty in x is ± 0.01. Inset: $\log_{10}\sigma$ vs $T^{-1/2}$. Right panel: σ -vs- magnetic field for a-GdSi (G3) at different temperatures (normalised to $\sigma(0)$, the zero field value at each temperature). Inset: $\sigma(60\ KOe) - \sigma(0)$ normalised by $\sigma(0) \equiv$ the magnetoresistance versus temperature for G1-G4.

4.2 Experiments on a-GdSi

Let us review the basic experiments in a-GdSi in some detail. The measurements have been made [15, 16, 17, 18, 19] on a-GdSi and simultaneously on the *non-magnetic analog* a-YSi, to clarify the role of magnetic moments on the IMT. The results are broadly on (i) the conductivity, σ, and the magnetoresistance, (ii) spectral properties/density of states (DOS), probed through tunneling, (iii) thermodynamic properties: specific heat, C_V, and entropy, S, (iv) magnetic properties: the linear response susceptibility $\chi(T)$ and the magnetisation $m(h, T)$, and (v) the magneto-optical response.

4.2.1 Conductivity:

We begin with the conductivity, Fig.1 reproduced from [15].

- Both Y_xSi_{1-x} and Gd_xSi_{1-x} show an insulator-metal transition as the doping, x, is increased across a critical value x_c. The critical doping required $(x_c \sim 14\%)$ is slightly greater in GdSi compared to YSi.

- For both GdSi and YSi, in the doping range $0.17 > x > 0.11$, the conductivity has $d\sigma/dT > 0$, *i.e* $d\rho/dT < 0$, at all T. This is true even of the systems which are 'metallic' at low temperature.

- For the metallic samples the low temperature conductivity can be fitted to $\sigma(T) \sim \sigma_0 + \sigma_1\sqrt{T}$. σ_0 and σ_1 are constants and the $\sqrt{T}$ term arises from Coulomb effects

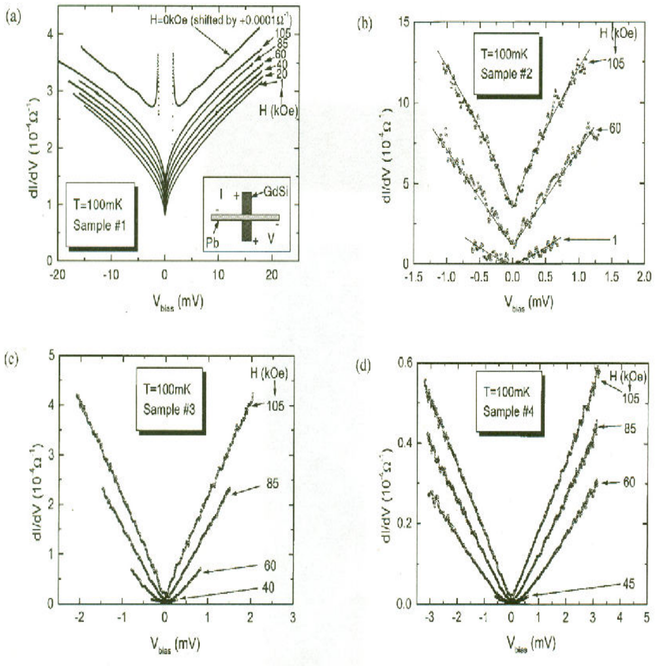

Figure 4.2: $(a) - (d)$ Tunneling conductance dI/dV -vs- bias voltage V_{bias} of four GdSi/oxide/Pb tunnel junctions, at $T = 100$ mK for indicated magnetic field H. (a) Sample 1 is the most metallic sample reported. The $H = 0$ data are offset by $1 \times 10^{-4}\Omega^{-1}$ for clarity: other H data are not offset. With increasing $H > 1$ KOe, dI/dV increases. (b) Sample 2 is very close to the MIT at $H = 0$. As H is increased there is a transition in the bias dependence of the conductance. (c) Sample 3 is metallic for $H > 50$ KOe and (d) Sample 4 is metallic for $H > 60$ KOe.

in a disordered system [8]. On the insulating side $\sigma(T) \sim e^{-\sqrt{T_0/T}}$, indicating variable range hopping (VRH) in the presence of a soft Coulomb gap [20].

- All Gd based systems, in the doping range studied, show pronounced negative magnetoresistance (MR). The MR increases on reducing x (towards x_c), on decreasing T, and on increasing h. YSi samples of comparable composition show a significantly smaller, *positive*, MR.

- The field dependence of conductivity is seen to arise principally from variations in σ_0 in the metallic phase [21], and from the variation of T_0 in the insulator [22]. So, the dominant *temperature dependence* of the conductivity in the metallic phase arises from Coulomb effects, driving the $\sqrt{T}$, *but the MR arises almost entirely from variations in the* $T = 0$ *conductivity.*

- For GdSi samples with $x \lesssim x_c$ a magnetic field can drive the system metallic. Near this field driven IMT, σ_0 varies as $(h - h_c)$, h_c being the field at which the IMT occurs.

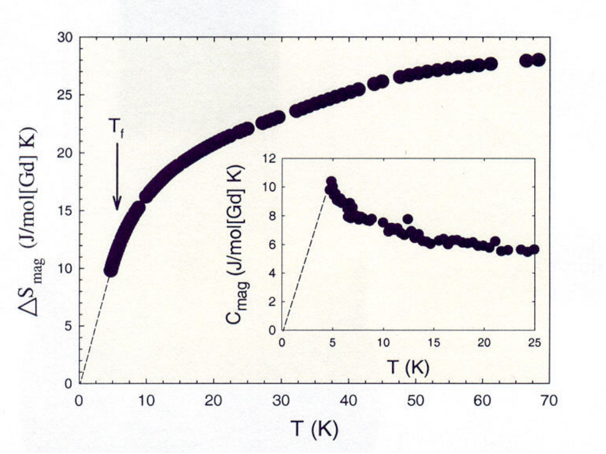

Figure 4.3: Magnetic entropy developed -vs- T for a sample. The dashed line is the entropy from the extrapolated C_{mag}. Inset: C_{mag} -vs- T with the extrapolation shown as a dashed line. $T_f = 5.2$ K in this case and $R\ln(2S_{Gd}+1) = 17.3$ in the units shown.

4.2.2 Tunneling DOS:

The low energy DOS, Fig.2, has been studied [18], from measurement of the tunneling conductance, across the field driven IMT. These measurements provide direct information on the evolution of the correlation gap [8] (dip in DOS at ϵ_F) near the metal-insulator transition and the Coulomb gap [20] in the insulating phase. The principal conclusion from these measurements is that, for the field tuned transition, the density of states at the Fermi level, $N(0)$, varies as $(h-h_c)^2$ while $\sigma_0(h) \sim (h-h_c)$. The critical behaviour near the IMT, therefore, follows $N(0) \propto \sigma^2$, with both the DOS and the d.c conductivity vanishing at the transition.

4.2.3 Specific heat:

The difference in the thermodynamic properties of magnetic and non magnetic systems again emphasises the role of the doped moments. Even for disordered 'non-magnetic' systems close to the metal-insulator transition the specific heat has a contribution arising from 'local moments' [23]. This arises because electrons can behave like *localised* $S = 1/2$ *objects* in the presence of disorder and strong EE interactions [24].

Naively, we would have expected that after subtracting out the specific heat of the non magnetic analog the 'high temperature' entropy of the magnetic system would correspond to $S^0(\infty) \sim n_{sp}\log(2S+1)$. Results on GdSi, Fig.3, differ from this:

- Specific heat measurements indicate that at 'high' temperature $S_{mag}(T) = \int_0^T dT' C_V^{mag}/T'$ is larger [16] than $S^0(\infty)$ by approximately 50%! The total magnetic entropy tends to saturate, at this (larger) value by $T \sim 60-70$ K. A simple minded estimate [16] suggests that the additional entropy can be accounted for by ~ 2 spin 1/2 moments (conduction electrons) for each Gd moment.

- C_V^{mag} should vanish as $T \to 0$, however, down to 5 K, it shows *no sign of a downturn* [16].

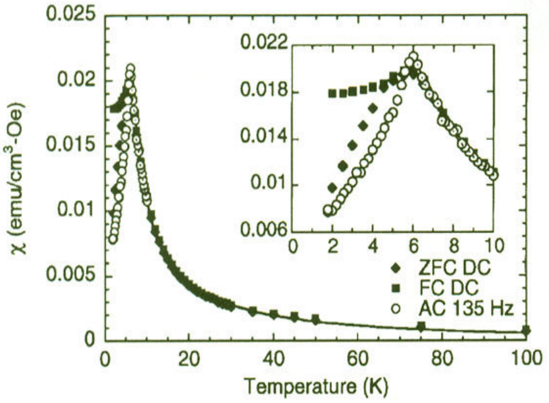

Figure 4.4: χ for $x = 0.14$. χ_{dc} was measured in 100 Oe after cooling (ZFC) or at 300 K (FC). χ_{ac} was measured in 135 Hz, 4 Oe, after cooling to 10 K in zero field. Line is a Curie Weiss fit above T_f. Inset: same data on an expanded scale.

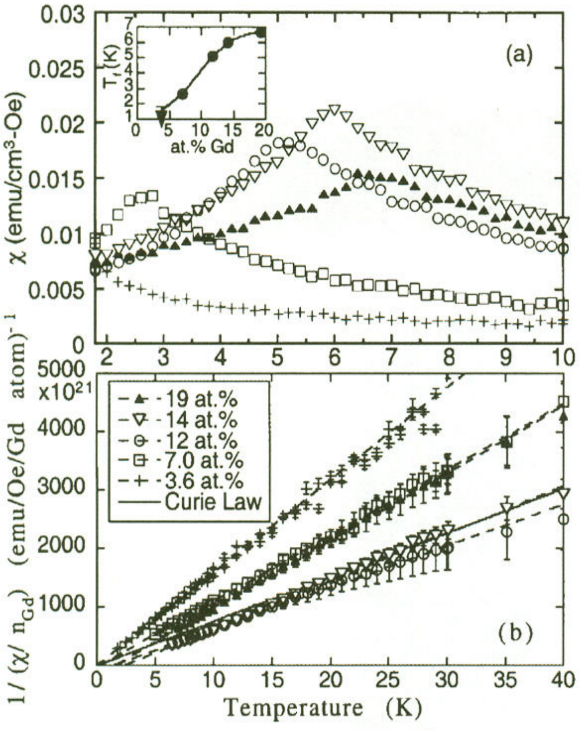

Figure 4.5: (a) $\chi(T)$ for $x = 0.036 - 0.19$ measured at 135 Hz in a 4 Oe field. Inset shows T_f (from peak in χ_{ac}) -vs- % Gd. (b) Inverse χ_{dc} (measured in 100 Oe) -vs- T. Dashed lines are Curie-Weiss fits. Solid line in (b) is the Curie law for non interacting Gd moments.

This suggests that the peak in C_V^{mag} occurs somewhere below 5 K. At high temperature the magnetic and non magnetic systems have the same C_V.

4.2.4 Magnetism:

The doped Gd atoms possess a moment $J = S = 7/2$, arising from the half-filled f shell. The coupling between the randomly located moments arises primarily through mediation by the conduction electrons. The overall magnetic effects also have contributions from the 'local moments' in the conduction electron system, alluded to in the previous paragraph. The basic observations on the magnetism, Fig.4-5, are:

- Measurements at high fields, $h \sim 1$ T, show a magnetisation growing as $\sim 1/T$, *i.e*, free moment like response. However, measurements of χ at low field ($h \sim 10$ mT), reveals a transition [17] to a spin glass state at a temperature $T_f \sim 1 - 6$ K depending on doping.
- There is a distinct difference between the field cooled (FC) and zero field cooled (ZFC) susceptibilities $\chi(T)$; the χ_{FC} saturates to a higher value as $T \to 0$.
- The freezing temperature increases from $T_f \sim 1$ K at $x = 0.04$ to $T_f \sim 6$ K at $x \sim 0.20$. The observation of the characteristic [25, 26, 27] (logarithmic) frequency dependent shift of T_f confirms that these are indeed spin glasses.
- Fitting a Curie form to the susceptibility, $\chi(x, T) = A(x)/(T - \theta(x))$, reveals that the effective moment, μ_{eff}, which can be extracted from A, varies significantly with x. Naively, this should have been just $\sqrt{S(S+1)}$, independent of x. It is close to this expected (free moment) value for $x \approx x_c$ and falls off on both the metallic and insulating sides.
- The spin glass freezing does not have any signature in the temperature dependence of transport properties. The freezing itself is eliminated by fields $h \gtrsim 0.1$T.

The magnetic state, which crucially affects electronic transport, is itself determined by electron spin interaction, the background disorder, and EE effects.

4.2.5 Optical response

There is huge transfer optical spectral weight with increasing temperature in both YSi and GdSi, Fig.6. This follows the rapid rise in the d.c conductivity itself with increasing T. In GdSi, such spectral weight transfer can also be driven by applying a magnetic field, for materials which are on the insulating side of the IMT [19]. The frequency interval over which such transfer occurs is a couple of orders of magnitude larger that the field scale itself.

4.2.6 Summary

Let us abstract our lessons from these effects, to start on a theory. The *primary* effect in amorphous magnetic systems is electron localisation due to disorder, either due to randomness in the amorphous structure or disorder in the spin configuration. To a first approximation, the IMT is driven by varying the mobility edge ϵ_c across ϵ_F. However, as the data indicates, the transition is not a simple 'Anderson transition', driven by structural and spin disorder, in a non-interacting electron system. Electron-electron interaction effects are clearly in evidence in (i) the T dependence of $\sigma(T)$, (ii) low energy features in the DOS, $N(\epsilon)$, (iii) the 'excess entropy', at high temperature, and (iv) the non monotonic variation in μ_{eff} across the IMT.

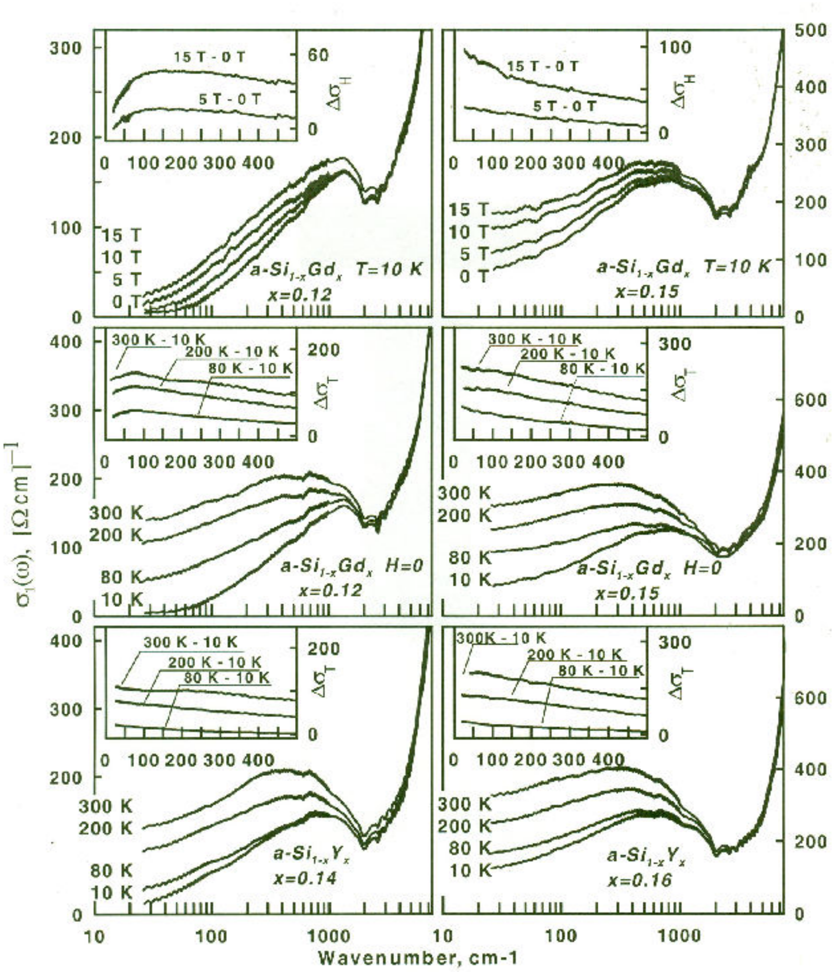

Figure 4.6: The optical conductivity of a-Si$_{1-x}$RE$_x$ films at different temperatures (middle and bottom panels) and magnetic fields (top panels). Insets show differential conductivity $\Delta\sigma_T(\omega)$ and $\Delta\sigma_H(\omega)$ defined in the text. In all samples the intragap conductivity is strongly reduced at low T with the spectral weight being transferred to energies exceeding the band gap of amorphous Si. In a-Si$_{1-x}$Gd$_x$ films a part of the spectral weight, which is lost at $T < 80$ K, is recovered in high magnetic field (top panels).

The transition, however, is not driven by interaction effects *per se*. Interactions become relevant near the transition, there the effects of disorder and interactions cannot be deconvolved, but most of the phenomena occur *because the system is strongly disordered.* Since we will study a model without EE effects, note that many of the experimental results *can be understood*, at least qualitatively, even without such interaction. These include (i) the *existence* of an IMT, from variation in the 'effective disorder' seen by the electron, (ii) a magnetically disordered ground state and the spin glass signatures, and, (iii) the large MR from the field tuning of spin disorder.

This problem, even without Coulomb effects, is non trivial because: (a) there is no simple method for accessing transport properties in the regime we are interested in (even if the 'disorder' were completely specified), and (b) the 'spin disorder' is *not specified*, the magnetic state itself depends intimately on the electronic spectrum and wavefunctions.

4.3 Model for a-GdSi

A 'first principles' model for a-GdSi will have to consider an underlying 'random' structure in which a fraction x of the sites are occupied by Gd atoms and $(1-x)$ by Si atoms. The Gd and Si atoms have different orbital structure so a complicated set of inter-orbital, intersite hopping possibilities need to be considered. We try to retain the essential features in the following, simpler, one band model:

$$\begin{aligned} H &= -t \sum_{\langle ij\rangle,\sigma} c^{\dagger}_{i\sigma} c_{j\sigma} + \sum_{i\sigma} (\epsilon_i - \mu) n_{i\sigma} - J' \sum_{\nu} \sigma_{\nu}.\mathbf{S}_{\nu} \\ &\quad - \lambda \sum_{\nu} n_{\nu} x_{\nu} + \frac{1}{2} K \sum_{\nu} x_{\nu}^2 + H_{Coul} \end{aligned} \tag{4.1}$$

This is a tight binding model with uniform hopping t, and an on site potential ϵ_i uniformly distributed between $\pm\Delta/2$. The sites labelled 'ν' are a fraction x of the lattice corresponding to the dopant (Y/Gd) locations. The electron-spin coupling is J', $\mathbf{S}_i$ are the $S = 7/2$ Gd spins, and $\sigma_{i\mu} = \sum_{\alpha\beta} c^{\dagger}_{i\alpha} \tau^{\alpha\beta}_{\mu} c_{i\beta}$, where τ_{μ} are the Pauli matrices. The x_i are local displacement variables (bond distortions [28]) coupled to the electron density via λ, and the structural stiffness is K. H_{Coul} would include Hubbard and long range Coulomb interactions.

The width of the impurity level distribution (Δ) in YSi/GdSi has been estimated [17] to be ~ 200 meV, and the 'polaron binding energy' $g = \lambda^2/K \sim 30$ meV. The existence of lattice polaron effects in amorphous semiconductors had been argued early on by Anderson [28], and has been revived now [17] in the context of doped a-Si. We think the diamagnetism in YSi confirms bipolaronic effects, but these lattice effects are probably not very important in GdSi. There is no simple estimate of the 'effective hopping amplitude' to be used in a single band approximation. However, calculations on the Anderson model indicate [29] that we need $\Delta/t \approx 14$ to localise 10% of the electronic states in the band. This suggests a rather small effective hopping amplitude ~ 200 K, if Δ is 200 meV. The electron-spin coupling $J'S$ (called J' from now on), arising out of the $d - f$ coupling in Gd, is large. It is estimated to be ~ 0.9 eV from photoemission measurements [30] on Gd, but would be somewhat smaller in the effective one band description that we are using. Although the parameter values have some uncertainty it is clear that $\Delta, J' \gg t$. We use $\Delta/t = 11$, $J'/t = 4$, $g/t = 0.5$, $K = 1$, roughly consistent with the experimental estimates. The electron-phonon and electron-spin coupling are operative only at the dopant sites. We distribute the 'impurities' (Y or Gd in the

Si host) into Nx sites with the lowest potential in any given realisation $\{\epsilon_i\}$. This ensures that at low dopant concentration, the electrons are trapped near the dopant sites. All energies are measured in units of t, and finally set $t \approx 500$ K for comparing our results with the experiments.

Our principal results using the Hamiltonian above are the following:

- The magnetic ground state in the low doping region is a spin glass with T_f having overall scale $\sim t^2/(J' + \Delta)$ and following the experimental doping dependence,
- There is a metal-insulator transition for both GdSi and YSi with decreasing x, with $x^c_{Gd} \gtrsim x^c_Y$, and a field driven IMT and CMR for GdSi,
- There is large transfer of spectral weight from high to low frequency in $\sigma(\omega)$, driven by an applied magnetic field in GdSi.

We explain our scheme of calculation next and then discuss these results in detail.

4.4 Method

Since the Hamiltonian involves $\Delta/t, J'/t \gg 1$ and $g/t \sim \mathcal{O}(1)$ none of these couplings can be handled perturbatively. To study the properties of this model within a controlled approximation we use a finite size combination of Monte-Carlo (MC) and exact diagonalisation (ED) [31]. This approach exactly handles the strong disorder, but treats the spin and lattice variables as 'classical'. Since we have $2S \gg 1$, the 'classical' spin limit is reasonable, and the adiabatic approximation should capture the leading effect of electron-phonon coupling.

If we ignore H_{coul} to start with, H represents non-interacting fermions coupled to classical variables $\mathbf{S}_i$ and x_i, in addition to the random potential ϵ_i. The ϵ_i are 'quenched' variables while the spin and lattice degrees of freedom are 'annealed', with the distribution $P\{x, S\} = Z^{-1}\mathrm{Tr}e^{-\beta H}$ where $Z = \int \mathcal{D}S\mathcal{D}x\mathrm{Tr}e^{-\beta H}$ is the full partition function for a specific realisation of $\{\epsilon_i\}$.

The 'exact' MC+ED allows only small system sizes, $\mathcal{O}(100)$ sites, so the key step is to construct an approximate 'effective Hamiltonian' for the lattice and spin variables. Once the magnetic and phonon problem are self consistently solved, the $T = 0$ electron problem can be solved in the classical ground state $\{\mathbf{S}_i, x_i\}_0$, which itself depends on $\{\epsilon_i\}$, finally averaging over disorder.

4.4.1 The magnetic problem

Formally the magnetic effective Hamiltonian is

$$H_{eff}\{S\} = -\frac{1}{\beta} \log \int \mathcal{D}x\mathrm{Tr}e^{-\beta H}$$

We have $J'/t \gg 1$, a dilute system (the spins occupy only a fraction x of sites), and strong disorder in the electron system. There is no perturbative expansion possible in J' but the large J' and $x \ll 1$ allows a simplification. In this limit the doped carriers are essentially localised at the magnetic sites, with the electron density falling off exponentially away from the sites. This generates a pairwise *antiferromagnetic coupling*, for $R_{ij} > 1$, with $J_{ij} \sim (t^2/J')e^{-R_{ij}/\lambda(J')}$, with $\lambda \propto 1/J'$. For neighbouring sites the coupling is ferromagnetic $\sim \mathcal{O}(t)$.

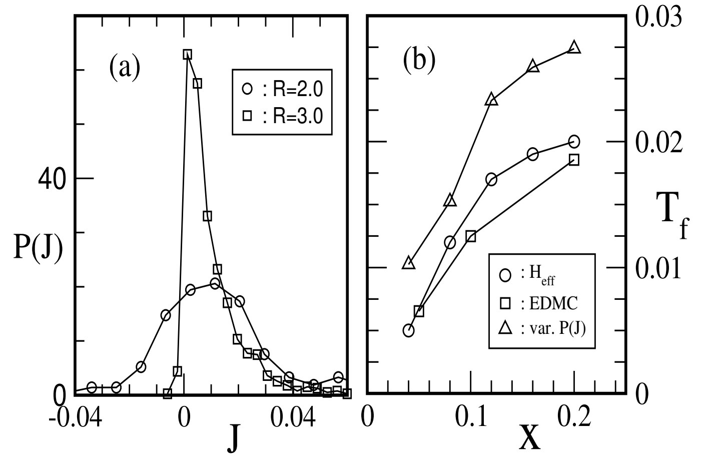

Figure 4.7: (a)Bond distributions and (b) the freezing scales inferred from the variance of distributions as well as actual simulations.

In the disordered system, for a given separation R_{ij}, the bonds have a distribution. We construct the distributions $P(J, R_{ij})$ and study the model:

$$H_{eff}\{\mathbf{S}\} = \sum_{ij} J_{ij}\mathbf{S}_i.\mathbf{S}_j.$$

The bond distribution $P(J, R_{ij})$ is constructed by picking a pair of spins located at separation R_{ij} on the lattice and finding out the energy difference between the parallel and antiparallel spin configurations using exact diagonalisation. Fig. 7(a) shows the bond distributions at $R = 2$ and $R = 3$. The presence of both positive and negative bonds hints towards a complicated ground state for the spins. Fig.8.(b) compares the T_f scales obtained from the actual simulations with those inferred from the width of bond distributions.

For a pair of moments located at $\mathbf{R}_i$ and $\mathbf{R}_j$ the J_{ij} is picked from $P(J, R_{ij})$. This ignores correlations between bonds in a specific $\{\epsilon_i\}$ realisation. We simulate the model for different dilutions, compute the order parameter for freezing,

$$q(T) = (xN)^{-1} \sum_i |\langle \mathbf{S}_i \rangle_T|$$

and check that the structure factor has no peaks at any wavevector $\mathbf{Q}$.

4.4.2 Handling the phonons

Solving the magnetic problem establishes the spin glass nature of the ground state, without yet bringing in the phonons. We simplify the remaining electron-phonon problem by assuming the spins to be frozen in an uncorrelated random manner, ignoring the short range spatial correlations in the spin glass.

The effective Hamiltonian for phonons is $H_{eff}\{x\} = -\frac{1}{\beta}\log\int \mathcal{D}\mathbf{S}\mathrm{Tr}e^{-\beta H}$. At moderate g and strong disorder there would be 'frozen' bond distortions in the ground state, and we cannot expand about the $x_i = 0$ state. To incorporate this effect we use the lowest order self-consistent expansion, *i.e*,

$$H_{eff}\{x\} \approx \frac{1}{2}K\sum_i x_i^2 + \sum_i a_i x_i$$

with $a_i = -\lambda\bar{n}_i$, where $\bar{n}_i = \langle n_i\rangle$, computed in the electronic ground state. The minimum of H_{eff}, *i.e* the lattice distortion in the ground state, corresponds to $\bar{x}_i = (\lambda/K)\bar{n}_i$. The $T = 0$ problem now corresponds to electrons in the background of structural disorder, $\{\epsilon_i\}$, coupled to randomly oriented spins with coupling J', and density coupled to a phonon field $x_i = (\lambda/K)\bar{n}_i$, *i.e*,

$$H^{el}_{eff} = H_{kin} + \sum_i \epsilon_i n_i - J'\sum_v \sigma_v.\mathbf{S}_v - g\sum_v \bar{n}_v n_v \tag{4.2}$$

4.4.3 Transport

We solve this problem through iterative ED. The transport and spectral properties of YSi correspond to $g = 0.5$ and $J' = 0$, while for GdSi $g = 0.5$ and $J' = 4$. The ED is done for a sequence of sizes $6 \times 6 \times L$, with $L = 24, 32, 40, 48$. Due to the finite size gaps the d.c. conductivity cannot be directly computed on finite systems. We use the Kubo-Greenwood formula to compute the integrated optical spectral weight $\sigma_{int}(\Delta\omega) = \int_0^{\Delta\omega}\sigma(\omega)d\omega$, disorder average, and invert to obtain the optical conductivity $\sigma(\omega)$. The extent of averaging varies from $400 - 100$ realisations, decreasing with increasing L. We track $\sigma(\omega_{ref}; L)$ with $\omega_{ref} \propto L^{-1}$, setting $\omega_{ref} = 0.08$ at $L = 32$, and use $\sigma_{dc} = \lim_{L\to\infty}\sigma(\omega_{ref}, L)$.

4.5 Results

4.5.1 Spin glass phase

Fig.8 shows $q(T)$, alongwith $\chi(T)$ at $x = 0.2$, and the freezing temperature [32] $T_f(x)$. At $x = 0.2$ our $T_f \sim 10$K, while experimentally $T_f \sim 6$K. We have done the exact MC+ED simulation for 4^3 systems, with the same J', Δ and $x \sim 0.1$ and verified that the system freezes into a spin glass, with T_f within 10% of our result here.

4.5.2 Insulator-metal transition

Fig.9(a) shows this 'dc' conductivity appropriate to YSi and GdSi. Our x_c are smaller than the experimental values and we have not fine tuned parameters to match the data. The σ are in units of $\pi e^2/\hbar a_0$ and the typical values shown in Fig.9(a) are ~ 0.01. For $a_0 \sim 2$Å, $\sigma_{dc} \sim 400$ $(\Omega cm)^{-1}$, roughly as in experiments [15]. Fig.9(b) shows the L dependence of $\sigma(\omega_{ref}; L)$, while Fig.9(c) shows the 'magnetoconductance'. We have checked that the conductivity in a 'spin glass' backgound shows the same trend as for random spins and the numbers match within $\sim$ 20%.

To our knowledge there are no standard results on electron systems combining strong structural disorder *and* strong coupling to dilute magnetic moments. In the well studied opposite limit, $\Delta/t \gg 1, J'/t \ll 1$, spin flip scattering actually *weakens* [4] Anderson localisation, so large J'/t is crucial to enhanced localisation in GdSi. We have cross checked the trends in

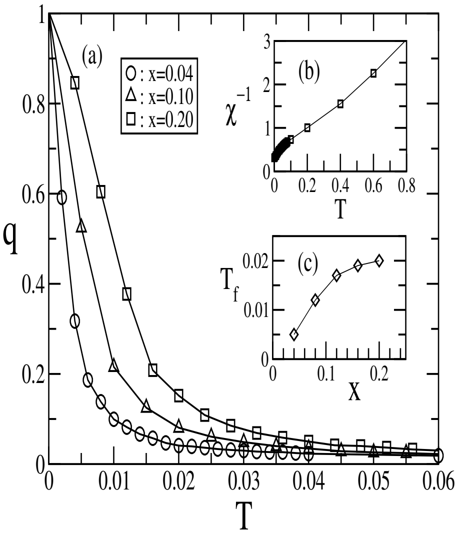

Figure 4.8: (a). Order parameter for freezing, $q(T)$ (see text), within our effective magnetic model. Insets: (b). The inverse susceptibility $\chi^{-1}(T)$ over a large temperature range. (c). Freezing temperature $T_f(x)$. Simulation on 10^3 lattices.

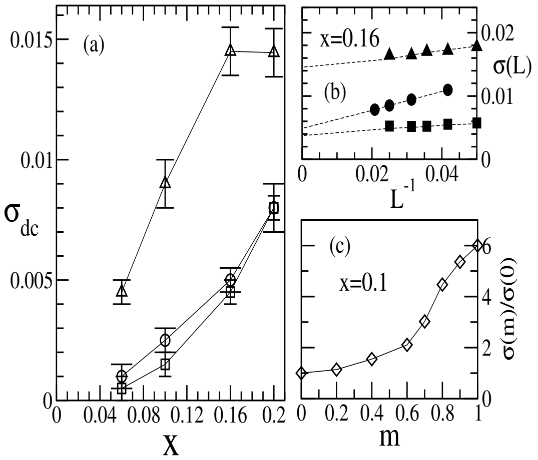

Figure 4.9: (a): D.C conductivity, at $T = 0$. Model for: YSi (circles), GdSi in the spin glass phase (squares), and GdSi in the fully polarised phase (triangles). (b): $L \to \infty$ extrapolation to construct σ_{dc} (see text). (c): GdSi: dependence of σ_{dc}, at $x = 0.10$ and $T = 0$, on magnetisation.

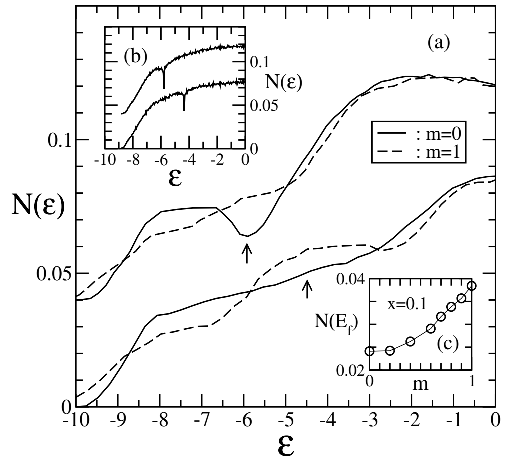

Figure 4.10: (a). Density of states in the model for GdSi for two densities, $x = 0.1$ and $x = 0.2$, for random spins $(m = 0)$ and polarised spins $(m = 1)$. The curves are vertically shifted by 0.04. Fermi energy marked by arrows. (b). DOS in model for YSi, at $x = 0.1$ (above) and $x = 0.2$ (below). (c). DOS at ϵ_F in the model for GdSi, at $x = 0.1$, with increasing magnetisation.

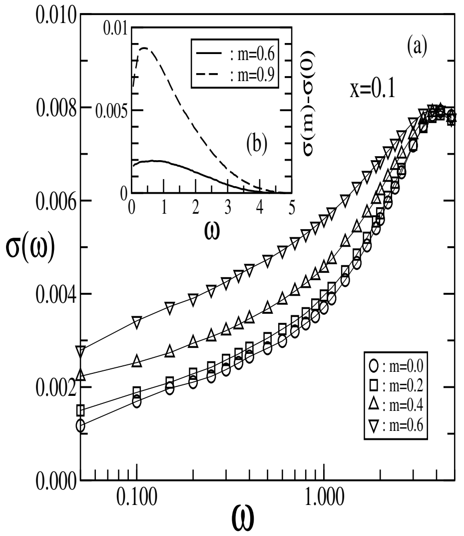

Figure 4.11: Variation of optical conductivity in the model for GdSi, at $T = 0$, with degree of magnetisation. Note the log scale in frequency. Inset: magneto-optical conductivity.

σ_{dc} by computing the averaged Greens function $G^{\sigma\sigma'}(\mathbf{r}-\mathbf{r}')$ at large Δ, with increasing J'. Using $\mathrm{Tr}G = \sum_{\sigma} G^{\sigma\sigma}(\mathbf{r}-\mathbf{r}')$ as the indicator of 'delocalisation', we find that at $|\mathbf{r}-\mathbf{r}'|/a_0 = 6$, $\mathrm{Tr}G$ *grows* with J' upto $J' \sim 0.5$ and then falls rapidly. It recovers quickly as the spins are polarised by an applied field, tracking the change in conductivity.

4.5.3 Spectral features

The DOS computed by us in the magnetic case, at low x, has a broad minimum at ϵ_F, Fig.10.(a), since J' pulls down states to lower energy. This minimum is *not* related to the Altshuler-Aronov 'correlation gap' which would be a sharper feature near ϵ_F (with effects of H_{coul} included). In YSi, the effect of phonons on the disordered background shows up as a sharp dip [4] in the DOS, Fig.10.(b), since it generates a short range attractive interaction with $U_{eff} = -\lambda^2/K$.

4.5.4 Magneto-optical Response

We mimic the effect of finite field, in GdSi, by using a spin distribution with specified magnetisation, *i.e*, finite $\langle S_z \rangle$. Finite m leads to significant redistribution of weight in the DOS, due to the large J', which should be visible in photoemission measurements. The conjunction of increased mobility, and increased DOS near ϵ_F, Fig.10.(c), leads to the large changes observed in $\sigma(\omega)$, Fig.11 The 'outer scale' in $\sigma(\omega)$ is $\sim 5t \approx 0.25$ eV, as in the data [17].

4.6 Coulomb effects

There are certain experimental features for which the 'Mott' aspect is essential. These are principally the $\sqrt{T}$ dependence in $\sigma_{dc}(T)$, the $\sqrt{\omega}$ correlation gap, the T driven spectral weight transfer in $\sigma(\omega)$, and the excess magnetic C_V. Most of these are generic correlation effects, well known in other amorphous systems [4, 7], and unrelated to the magnetic character.

4.7 Concluding remarks

There is a certain uniqueness to a-GdSi. Disorder, electron-spin coupling and electron-phonon interactions are features common, in some form, to a-GdSi, Anderson-Mott systems (NbSi, say) and the CMR manganites. The crucial differences are: (i) GdSi is a *strongly disordered 'dilute' magnetic system, with strong electron-spin coupling.* These features are essential to the spin glass behaviour and the consequent IMT and CMR. Electron-phonon interactions, even if present, are not crucial to the physics. (ii) Anderson-Mott systems are also *strongly disordered, but nominally non magnetic*. There are no remarkable magnetic field effects and the physics is controlled by disorder and electron correlations. (iii) Most CMR manganites are reasonable metals at low temperature, indicating *weak intrinsic disorder*. They have *strong electron-spin coupling* on a *periodic Mn lattice*, which, in contrast to 'dilution', promotes double exchange *ferromagnetism*. Electron-phonon (Jahn-Teller) interactions are important in these systems. The finite temperature IMT and CMR are related to multi-phase coexistence [33] and not an Anderson transition. GdSi differs also from the diluted magnetic semiconductors in that the spin polaron concept is not tenable in this high electron density system, due to strongly overlapping wavefunctions.

Our study provides a qualitative understanding of the insulator-metal transition, CMR, spin glass freezing and optical properties of a-GdSi, bridging the gap between Anderson-Mott transition and CMR systems.

Bibliography

[1] N. F. Mott and E. A. Davis, *Electronic Processes in Non Crystalline Materials*, Clarendon Press, Oxford (1979).

[2] N. F. Mott, *Metal-Insulator Transitions*, Taylor & Francis, London (1990).

[3] P. W. Anderson, Phys. Rev. **109**, 1498 (1958).

[4] P. A. Lee and T. V. Ramakrishnan, Rev. Mod. Phys. **57**, 287 (1985).

[5] M. P. Sarachik in *Metal-Insulator Transitions Revisited*, Ed. P. P. Edwards and C. N. R. Rao, Taylor & Francis, London (1995).

[6] R. F. Milligan, T. F. Rosenbaum, R. N. Bhatt and G. A. Thomas in *Electron-Electron Interactions in Disordered Systems*, ed. A. L. Efros and M. Pollak, North Holland (1985).

[7] G. Hertel, D. J. Bishop, E. G. Spencer, J. M. Rowell and R. C. Dynes, Phys. Rev. Lett. **50**, 743 (1983).

[8] See the review by B. L. Altshuler and A. G. Aronov in *Electron-Electron Interactions in Disordered Systems*, ed. A. L. Efros and M. Pollak, North Holland (1985).

[9] See the review by D. Belitz and T. R. Kirkpatrick, Rev. Mod. Phys. **66**, 261 (1994), for a summary of current understanding.

[10] See V. Dobrosavljevic and G. Kotliar, Phys. Rev. Lett. **78**, 3943 (1997), for a recent approach to the problem.

[11] T. Kasuya and A. Yanase, Rev. Mod. Phys. **40**, 684 (1968).

[12] P. A. Wolff, in *Semiconductors and Semimetals, Vol. 25*, Ed. Willardson and Beer, Academic Press (1988).

[13] S. von Molnar, A. Briggs, J. Floquet and G. Remenyi, Phys. Rev. Lett. **51**, 706 (1983).

[14] H. Ohno, H. Munekata, T. Penney, S. von Molnar and L. L. Chang, Phys. Rev. Lett. **68**, 2664 (1992).

[15] F. Hellman, M. Q. Tran, A. E. Gebala, E. M. Wilcox and R. C. Dynes, Phys. Rev. Lett. **77**, 4652 (1996).

[16] B. L. Zink, E. Janod, K. Allen and F. Hellman, Phys. Rev. Lett. **83**, 2266 (1999).

[17] F. Hellman, D. R. Queen, R. M. Potok and B. L. Zink Phys. Rev. Lett. **84**, 5411 (2000).

[18] W. Teizer, F. Hellman and R. C. Dynes, Phys. Rev. Lett. **85**, 848 (2000).

[19] D. N. Basov *et al.*, preprint, cond-mat 0104245.

[20] A. L. Efros and B. I. Shklovskii, J. Phys. **C8**, L49 (1975), and in *Electron-Electron Interactions in Disordered Systems*, ed. A. L. Efros and M. Pollak, North Holland (1985).

[21] W. Teizer, F. Hellman and R. C. Dynes, Sol. St. Comm. **114**, 81 (2000).

[22] P. Xiong, B. L. Zink, S. I. Appelbaum, F. Hellman and R. C. Dynes, Phys. Rev. B **59**, R3929 (1999).

[23] M. A. Paalanen, J. E. Graebner, R. N. Bhatt and S. Sachdev, Phys. Rev. Lett. **61**, 597 (1988).

[24] M. Milovanovic, S. Sachdev and R. N. Bhatt, Phys. Rev. Lett. **63**, 82 (1989).

[25] K. Binder and A. P. Young, Rev. Mod. Phys. **58**, 801 (1986).

[26] K. H. Fischer and J. A. Hertz, *Spin Glasses*, Cambridge (1991).

[27] J. A. Mydosh, *Spin Glasses*, Taylor & Francis (1993).

[28] P. W. Anderson, Phys. Rev. Lett. **34**, 953 (1975)

[29] E. N. Economou *et al.*, Phys. Rev. **B 30**, 1686 (1984)

[30] K. Maiti *et al.*, Phys. Rev. Lett. **88**, 167205-1 (2002).

[31] E. Dagotto *et al.*, Phys. Rev. **B 58**, 6414 (1998), M. J. Calderon and L. Brey, Phys. Rev. **B 58**, 3286 (1998).

[32] Stabilised in 3d by weak dipolar couplings: A. J. Bray *et al.*, Phys. Rev. Lett. **56**, 2641 (1986), A. Chakrabarti and C. Dasgupta, Phys. Rev. Lett. **56**, 1404 (1986).

[33] A. P. Ramirez, J. Phys. Condens Matter **9**, 8171 (1997), E. Dagotto *et al.*, : Phys Rep **344**, 1 (2001), *Colossal Magnetoresistive Oxides*, Ed. Y. Tokura, Gordon & Breach (2000).

Chapter 5

Disordered Double Exchange Magnets

Chapter Summary: We solve the double exchange model in the presence of arbitrary substitutional disorder by using the SCR scheme. The magnetic properties are studied through classical Monte Carlo on the effective Hamiltonian while the effective exchange, D_{ij}, are calculated by self-consistently solving the disordered fermion problem. We discuss the conductivity, magnetoresistance, optical response and 'real space' structure of the inhomogeneous ferromagnetic state, and compare our results with charge dynamics in disordered $La_{1-x}Sr_xMnO_3$. The large sizes, $\mathcal{O}(10^3)$, accessible with the SCR scheme allows a complete and controlled calculation on this disordered strongly interacting problem. The results reported here are published in Phys. Rev. Lett. **91**, 246602-1 (2003).

5.1 Introduction

As discussed in chapter 3, the double exchange (DE) model describes the strong coupling between itinerant electrons and localised 'core' spins in many transition metal systems. The combination of the strong local coupling, arising typically from Hunds rule, and the tendency of the carriers to delocalise and gain kinetic energy leads to an effective ferromagnetic interaction in these systems. In many of the 'real' systems there are other effects, *e.g*, electron-phonon coupling, Hubbard interactions, antiferromagnetic exchange, and disorder, that may be relevant in addition to DE interaction. While the simultaneous effect of these additional interactions may be important for realistic modelling, it is useful to have a complete description of simpler models for reference.

We have discussed the methods for approaching the clean DE model in detail earlier. The clean model has been studied by various authors, using a range of techniques, discussed before, and is essentially understood. The problem is more difficult in the presence of quenched disorder, which arises inevitably in real materials [1, 2, 3, 4, 5] from ionic substitution and resulting bond distortions. Disorder leads to an inhomogeneous magnetic state and enhances the density of low energy spin fluctuations. The resistivity arising out of structural disorder and magnetic scattering is usually large, comparable to the Mott resistivity [3, 4], violates Mathiessens rule, and cannot be accessed by standard transport theory. The optical response reveals a strongly non Drude character [4, 5], implying unconventional charge dynamics, and rapid loss in low energy spectral weight with rising temperature.

Most of these features, which depend explicitly on the *inhomogeneous spatial character of the magnetic and electronic state* cannot be captured within 'mean field' approximations, including 'dynamical mean field theory' (DMFT), and current 'real space' approaches are severely size limited in three dimension. In this chapter we use the SCR scheme, generalised to handle disorder in the electron system. As we will see, the method handles the interplay of disorder and spin correlation accurately, and allows us to provide the first controlled results on charge dynamics in the disordered double exchange (DDE) model. We map out the phase diagram, clarify the nature of the inhomogeneous ferromagnetic state, and provide results on magnetotransport and optical response in the model. Our results are directly relevant to the 'coherent to incoherent' crossover [3, 4, 5] in disordered $R_{1-x}Sr_xMn_{1-z}Al_zO_3$, and the properties of disordered metallic ferromagnets [6] in general.

The combination of structural disorder with even *quenched* spin disorder leads to a nontrivial transport problem [7]. For the DDE model there is the additional difficulty of annealing the spin variables. All these make the DDE model the ideal case for studying the interplay of strong correlations *and* strong disorder. Thankfully, compared to other such problems, for example the 2d electron gas, involving interactions and disorder, the DDE model turns out to be much more 'solvable'. In this chapter we hope to address some of the key qualitative issues concerning the DDE model, *e.g*,

- When does a spin disorder driven Anderson transition occur in the DDE model?
- How is the ferromagnetic T_c affected by Anderson localisation?
- What is the nature of the inhomogeneous magnetic state: in terms of ferromagnetic cluster formation above T_c, and non uniform disordering of the polarised state with increasing temperature about $T = 0$.
- What is the impact of quenched disorder on the magnetoresistance?
- Is there a 'coherent' to 'incoherent' crossover in the optical response?

5.1.1 Earlier work

Previous studies of the model have used variational mean field (VMF) theory [8], DMFT [9, 10], and the Monte Carlo approach [11] to access the magnetism. Transport properties have been analysed within DMFT [9] and by using 'scaling theory' [12] in the limits of a spin polarised $(T = 0)$ state and a fully spin disordered $(T \gg T_c)$ state. The real space MC technique has also been used [11] to study the spin wave spectrum, although, remarkably, there is no work on transport. Both VMF and DMFT 'factor' the correlated spin distribution into a product of single site distributions. This loses out on spin correlations and trivialises the paramagnetic phase. In addition, DMFT misses out key vertex corrections in the 'disorder average' process, losing electron localisation effects. The 'scaling theory' approach to electronic transport is valid for $T \to 0$ and $T \gg T_c$, but not of much use in the crucial regime around T_c. The only unbiased implementation of step (i) is via Monte Carlo, but the computational cost of these simulations limits typical sizes to $\sim 4^3$ in three dimension [13]. The small linear dimensions, and the large finite size gaps, make it impossible to reliably estimate transport properties. This is where the SCR method allows a breakthrough.

5.2 Model and Method

We work with the following model, defined on a three dimensional cubic lattice.

$$H = -t \sum_{\langle ij \rangle \sigma} c^{\dagger}_{i\sigma} c_{j\sigma} + \sum_i (\epsilon_i - \mu) n_i - J_H \sum_i \mathbf{S}_i . \vec{\sigma}_i \tag{5.1}$$

The nearest neighbour hopping $t = 1$ sets our energy scale. The potential ϵ_i is distributed uniformly between $\pm\Delta/2$. We set $J_H/t \rightarrow \infty$. The parameters in the problem are Δ/t, and density n (or chemical potential μ). We assume classical core spins, with $|\mathbf{S}_i| = 1$. There are two key steps in solving for the magnetic and transport properties of a model like this:

1. Evaluate the spin distribution, $P\{\mathbf{S}_i, \epsilon_i\}$, controlling the magnetic response, by 'integrating out' the electronic degrees of freedom. $\{\mathbf{S}_i, \epsilon_i\}$ denotes the full spin configuration.

2. Solve for the charge dynamics; resistivity, optical response, etc, in the background of structural disorder and equilibrium spin configurations.

Large J_H/t leads to the usual 'hopping disordered' spinless fermion problem.

$$\begin{aligned} H &\equiv -t \sum_{\langle ij \rangle} (\, g_{ij} \gamma^{\dagger}_i \gamma_j + h.c \,) + \sum_i (\epsilon_i - \mu) n_i \\ &= -t \sum_{\langle ij \rangle} f_{ij} (\, e^{i\Phi_{ij}} \gamma^{\dagger}_i \gamma_j + h.c \,) + \sum_i (\epsilon_i - \mu) n_i \end{aligned} \tag{5.2}$$

The hopping amplitude $g_{ij} = f_{ij} e^{i\Phi_{ij}}$ between locally aligned states, can be written in terms of the polar angle (θ_i) and azimuthal angle (ϕ_i) of the spin $\mathbf{S}_i$ as,

$$g_{ij} = \cos\frac{\theta_i}{2}\cos\frac{\theta_j}{2} + \sin\frac{\theta_i}{2}\sin\frac{\theta_j}{2} e^{-i\,(\phi_i - \phi_j)}$$

The overlap $f_{ij} = \sqrt{(1 + \mathbf{S}_i . \mathbf{S}_j)/2}$, while the phase is specified by $\tan\Phi_{ij} = Im(g_{ij})/Re(g_{ij})$.

This is a problem of quadratic 'spinless fermions' with core spin dependent hopping amplitudes, moving in the background of quenched disorder ϵ_i. To exploit the nominally 'non interacting' structure of the fermion part we need to know the distribution $P\{\mathbf{S}_i\}$, controlling the probability of occurence of a spin configuration.

5.2.1 Effective Hamiltonian for spins

We use the SCR method, as described in the previous chapter, for this disordered problem. We repeat some of the earlier arguments here for easy reference. The partition function of the system is $Z = \int \mathcal{D}\mathbf{S}_i Tr e^{-\beta H}$. To extract $P\{\mathbf{S}_i\}$ note that for a system with only spin degrees of freedom, Z will have the form $\int \mathcal{D}\mathbf{S}_i e^{-\beta H\{\mathbf{S}\}}$. Comparing this with the partition function of the spin-fermion problem we can use

$$\int \mathcal{D}\mathbf{S}_i Tr e^{-\beta H} \equiv \int \mathcal{D}\mathbf{S}_i e^{-\beta H_{eff}\{\mathbf{S}\}}$$

from which it follows that

$$\begin{aligned} H_{eff}\{\mathbf{S}_i\} &= -\frac{1}{\beta} \log Tr e^{-\beta H} \\ P\{\mathbf{S}_i\} &\propto e^{-\beta H_{eff}\{\mathbf{S}_i\}} \end{aligned} \tag{5.3}$$

The trace is over the fermion degrees of freedom.

As before, we propose:

$$-\frac{1}{\beta}\log \mathrm{Tr} e^{-\beta H} \approx -\sum_{\langle ij \rangle} D_{ij} f_{ij} \tag{5.4}$$

where D_{ij} is an effective 'exchange constant' to be determined as follows. Define the operator $\hat{\Gamma}_{ij} = (e^{i\Phi_{ij}}\gamma_i^\dagger \gamma_j + h.c)$. This enters the 'hopping' part of the electron Hamiltonian. The 'effective exchange' is determined as the thermal average of the fermion correlator over the assumed equilibrium distribution.

We bring together the consistency equations for ready reference:

$$\begin{aligned}
H_{el} &= -t\sum_{\langle ij \rangle} f_{ij}\hat{\Gamma}_{ij} + \sum_i (\epsilon_i - \mu) n_i \\
\hat{\Gamma}_{ij} &= (e^{i\Phi_{ij}}\gamma_i^\dagger \gamma_j + h.c) \\
H_{eff}\{\mathbf{S}\} &= -\frac{1}{\beta}\log \mathrm{Tr} e^{-\beta H} \approx -\sum_{\langle ij \rangle} D_{ij} f_{ij} \\
D_{ij} &= \langle\langle \hat{\Gamma}_{ij} \rangle\rangle_{H_{eff}}
\end{aligned} \tag{5.5}$$

This nonlinear integral equation for the D_{ij} is solved through the self-consistent MC scheme to construct the 'classical spin model' for a set of electronic parameters, disorder realisation, and temperature. The equilibrium thermal average of any fermion operator, or correlation function, $\hat{O}$, can be computed using the self-consistent distribution as:

$$\langle\langle \hat{O} \rangle\rangle = \int \mathcal{D}\{\mathbf{S}\} P\{\mathbf{S}\} O(\mathbf{S}) \tag{5.6}$$

The average $O(\mathbf{S})$ is computed on a spin configuration $\{\mathbf{S}_i\}$, with the configurations themselves picked according to the effective Boltzmann weight $\propto e^{-\beta H_{eff}}$. We iterate μ, at a given T etc, till the 'target' density is obtained.

5.2.2 Monte Carlo implementation

The MC implementation follows the same strategy as in the previous chapter, except for the additional task of keeping track of the inhomogeneous bonds.

1. Start at high temperature, $T \gg T_c$, assuming some $D_{ij}^n(T)$, where n is the iteration index. and 'equilibriate' the system with this assumed effective Hamiltonian (not yet self-consistent),

2. Compute the average $\langle\langle (e^{i\Phi_{ij}}\gamma_i^\dagger \gamma_j + h.c) \rangle\rangle$ over these (pseudo) equilibrium configurations. This generates $D_{ij}^{n+1}(T)$.

3. Compare the generated exchange with the assumed exchange at each bond. Accept if within tolerance. If converged, then D_{ij} represents the correct 'exchange' at that temperature. Else, replace D_{ij}^n by D_{ij}^{n+1}.

4. At each temperature and iteration, adjust μ as necessary to keep n constant.

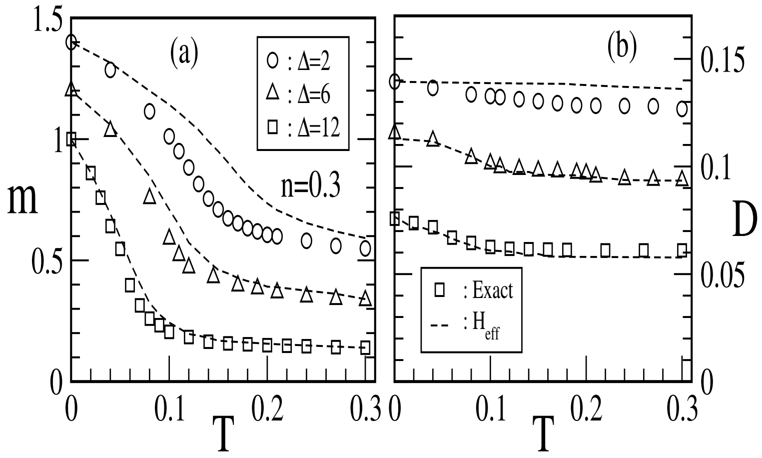

Figure 5.1: H_{eff} vs. Exact on $L = 4$. Panel (a): magnetisation on 4^3, open symbols ED-MC, dotted lines H_{eff}. Panel (b): effective exchange, averaged over system size: open symbols ED-MC, dotted lines H_{eff}.

At convergence fermion properties can be calculated and averaged over equilibrium MC configurations of the spin model. For the disordered system the thermal cycle above is repeated for each realisation of disorder. In the clean problem, translation invariance forces the exchange to be uniform at all bonds, while for DDE the iterations generate a bond disordered spin model. Equilibrium properties are calculated as described in the previous chapter, except for additional disorder average.

5.3 Results

5.3.1 Benchmarking H_{eff} against ED-MC

Let us start with a comparison of the SCR scheme with ED-MC for the DDE model. As we will see, the correspondence between SCR and ED-MC actually *improves* with increasing disorder, probably because increasing electron localisation makes the effective short range model more accurate.

Our first results, Fig.1, are on the disorder dependence of the magnetisation profile, $m(T)$, at $n = 0.3$ computed on a 4^3 system. As emphasised in the earlier chapter on SCR, the H_{eff} scheme overestimates T_c in the clean system, at high densities, by $15-20\%$. This is also visible in Fig.1.(a), however, there is a dramatic improvement in the match with increasing disorder. The mean (spatially averaged) effective exchange, computed with ED-MC and SCR, also have a visible difference at weak disorder, but are virtually indistinguishable at $\Delta = 6$ & 12.

Fig.2, left panels, shows some more data on thermodynamic indicators compared at $\Delta = 6$ and $n = 0.3$. Both the mean exchange and internal energy are accurately captured *over the entire temperature interval* by the SCR scheme. Lastly, Fig.2, right panels, shows the real

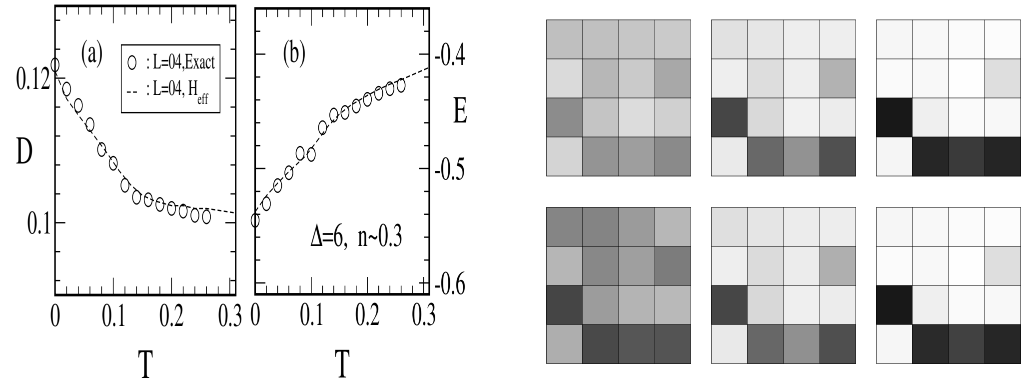

Figure 5.2: Left panels: Comparing average bond strength and energy between ED-MC and SCR. Right panels: Comparing real space density patterns. Top row: ED-MC, bottom row: SCR. Temperatures, from left to right, are $T \sim 2T_c, T_c, 0.1T_c$

space density pattern computed for the same realisation of ϵ_i and it is clear that in addition to overall thermodynamic features, the present scheme captures detailed spatially resolved properties as well. This is primarily due to a faithful solution of the Schrodinger equation in computing the effective exchange, exactly handling the underlying disorder, and would be vital in the phase coexistence problem discussed in the next chapter.

5.3.2 Phase diagram

Fig.3 shows the "global" phase diagram of the DDE model. The phases are ferromagnetic metal (FM), ferromagnetic insulator (FI) and the corresponding paramagnetic variants PM and PI. We have studied the problem at $n = 0.3$ and $n = 0.1$, varying disorder from the perturbative end to the localisation regime. Fig.3.(a). superposes the results at $n = 0.3$ and $n = 0.1$, appropriately scaling the disorder and temperature. The disorder (x axis) is measured in units of the critical disorder for Anderson localisation in the spin polarised phase, while the temperature (y axis) is measured in terms of the T_c of the non disordered model (at the appropriate density). The critical disorder for the PM-PI crossover, or the disorder dependence of T_c need not be 'universal' but seems to follow the same overall trend at moderate n. Fig.3.(b) shows the 'true' phase diagram specifically at $n = 0.3$.

The T_c of DE models is approximately related to the internal energy change: $T_c \log(2S+1) \sim \mathcal{E}(T_c) - \mathcal{E}(0)$, which in turn is related to the kinetic energy, K, at $T = 0$. At small Δ and $T = 0$, $K(\Delta) \sim K(0) - \chi_d \Delta^2$, where χ_d is the 'local' density response function. At strong disorder, in the 'localised' phase, $K(\Delta) \propto t^2/\Delta$. The correspondence of these limits with the inferred $T_c(\Delta)$ is visible in Fig.3.(b). Note that even at strong localisation, $\Delta \sim 24$, local excursion of the electrons can still sustain a $T_c \sim 0.05$, which would be ~ 75K for $t \sim$ 150meV. DMFT and VMF also provide qualitatively similar trends in T_c.

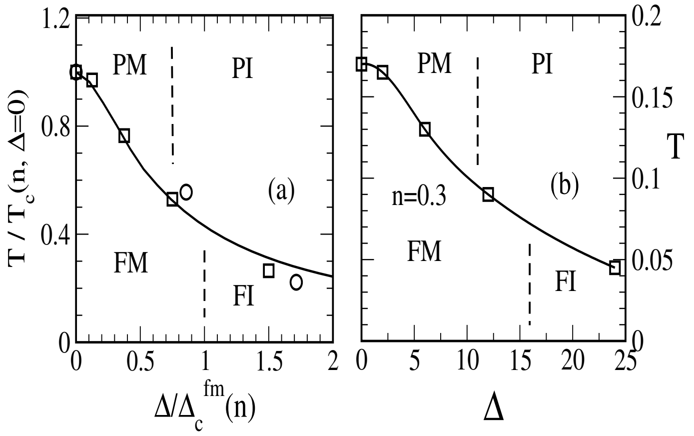

Figure 5.3: (a). Approximate 'universal' phase diagram of the DDE model. For a specified electron density, n, Δ is measured in units of the $T = 0$ critical disorder, $\Delta_c^{FM}(n)$, while T is measured in units of $T_c(n, \Delta = 0)$. Our data for $n = 0.1$ (circles) and $n = 0.3$ (squares) are described approximately by a common fit. (b). Actual phase diagram for $n = 0.3$.

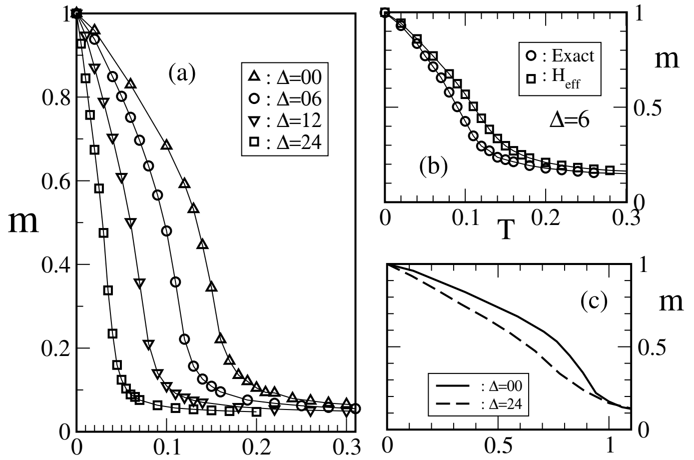

Figure 5.4: (a). Temperature dependence of magnetisation at $n = 0.3$, with Δ increasing from $0 - 24$. The inferred $T_c(\Delta)$ is shown in Fig.3. (b). Comparison of $m(T)$ obtained via 'exact' MC and H_{eff} on a 4^3 system at $n = 0.3$. Disorder average over 8 realisations in both case. (c). The scaled magnetisation $m(T/T_c(\Delta))$, at $n = 0.3$,for $\Delta = 0$ and $\Delta = 24$.

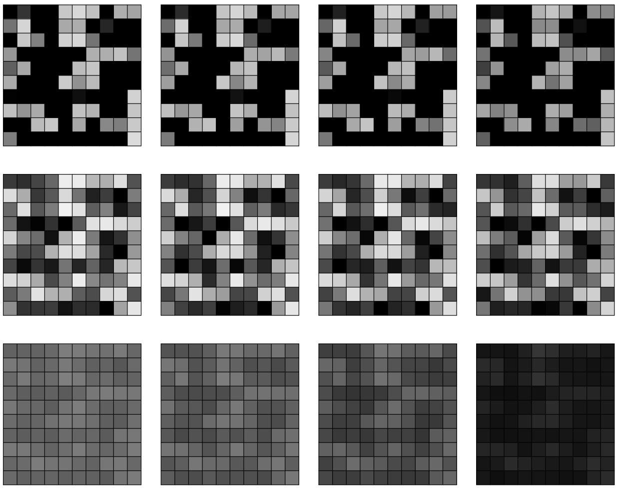

Figure 5.5: Real space images, top surface of a $10 \times 10 \times 10$ system with PBC, at $n = 0.3$ and $\Delta = 6$, for a specific realisation of disorder. First row: electron density distribution, $\langle n(\mathbf{r}) \rangle_T$, second row: effective exchange, $D(\mathbf{r}, \mathbf{r}+\delta : T)$, third row: nearest neighbour spin correlation, $f_2 = \langle \mathbf{S}(\mathbf{r}).\mathbf{S}(\mathbf{r}+\delta) \rangle_T$. Temperatures along the row are, $T/T_c \sim 1.2, 0.9, 0.6$ and 0.2. Dark regions correspond to high density (top row), strong exchange (central row), and strong FM correlation (bottom).

5.3.3 Magnetism

Fig.4.(a) shows $m(T)$ with increasing disorder, at $n = 0.3$, from which the data in Fig.3.(b) was inferred, while Fig.4.(b) compares the $m(T)$ computed with H_{eff} with the 'exact' MC at $\Delta = 6$. Although the asymptotic behaviour of $T_c(\Delta)$ is easy to motivate, Fig.4.(c) provides the first indication that the properties of the disordered ferromagnet cannot be understood by merely scaling T_c. Even though the $T = 0$ state is fully polarised, at low finite T the 'weak' bonds lead quickly to local disordering. The magnetisation $m(T/T_c)$ falls more sharply at low temperature in the disordered system [6]. The inhomogeneous character, and correspondingly wide distribution, of the 'exchange' leads to an overall increase in the density of low energy magnetic excitations. In addition to suppressing $m(T)$ it enhances the specific heat, $C_V(T/T_c)$, and reduces the spin wave stiffness D_{SW} [11].

5.3.4 Spatial inhomogeneity

The real space images, Fig.5, illustrate the inhomogeneous freezing into a ferromagnetic state in a 'cooling sequence', left to right. The density profile $\langle n(\mathbf{r}) \rangle$, first row, remains unchanged over the T range of interest, $0 - 1.2T_c$. The exchange, $D_{ij}(T)$, central row, is strongly spatially inhomogeneous, but as a whole not strongly T dependent. The bond distribution, $P(D, T)$ (not shown), reveals that weak bonds at low T get quickly weakened with increasing T while strong bonds are essentially T independent. The thermally averaged nearest neighbour spin correlation, $f_2 = \langle \mathbf{S}(\mathbf{r}).\mathbf{S}(\mathbf{r}+\delta) \rangle_T$, highlights the inhomogeneous disordering of the polarised

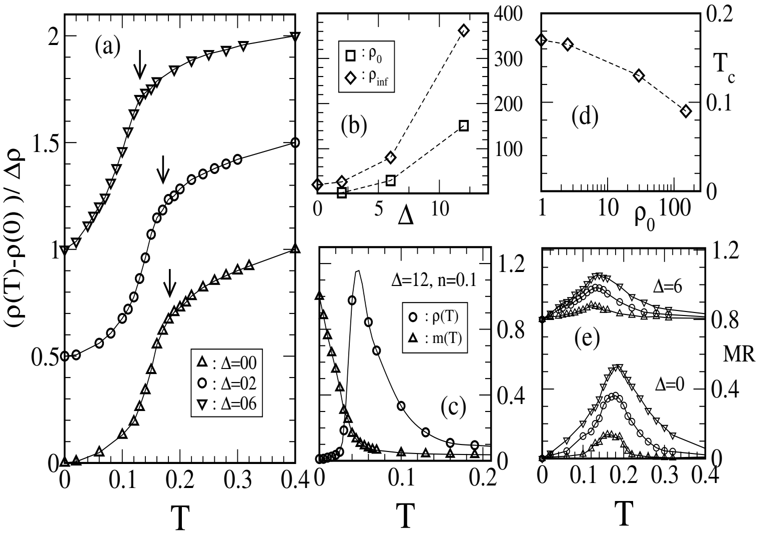

Figure 5.6: (a). Temperature dependence of resistivity at $n = 0.3$. We plot $\rho(T, \Delta) - \rho(0, \Delta)$ normalised by $\rho(0.4, \Delta) - \rho(0, \Delta)$, shifting successive curves by 0.5 for clarity. T_c is marked by an arrow on each curve. (b). Resistivity at $T = 0$, ρ_0, and at $T = 0.4$, ρ_{inf}, with increasing disorder. Note the clear violation of Mathiessens rule even at $\Delta = 2$, which would have required these curves to be parallel. (c) Resistivity normalised to maximum value $(\sim 10^4)$, and $m(T)$ at $n = 0.1$ and $\Delta = 12$ illustrating the FM $\rightarrow$ PI transition. (d). Variation in T_c with residual resistivity. Note the logarithmic scale on the x axis. (e). The magnetoresistance $(\rho(T, 0) - \rho(T, h))/\rho(T, 0)$ at $n = 0.3$: $\Delta = 0$ (lower set) and $\Delta = 6$ (upper set). The $\Delta = 6$ set has been vertically shifted by 0.8. Field values are $h = 0, 0.02, 0.05, 0.10$.

state with increasing T (white regions, two panels on the right), and the surviving local order for $T > T_c$ (left panel).

These results suggest the possible correlation between spatial inhomogeneity in the magnetic state and the bulk thermodynamics, for example the quicker disordering of the ferromagnetic state with increasing temperature, and the sharper fall in $m(T)$.

5.3.5 Transport and metal-insulator transitions

The interplay of thermal spin disorder and 'frozen' structural disorder also affects the charge dynamics. Increasing Δ increases the residual resistivity (ρ_0), with $\rho_0 \sim \rho_{Mott}$ at $\Delta \sim 10$. The resistivity deep in the paramagnetic phase (ρ_{inf}), tracked at $T = 0.4$ in Fig.4.(b), is not simply the additive contribution of structural and spin disorder. If Mathiessens rule were obeyed, $\rho_{inf} - \rho_0$ should have been constant.

The deviation arises from interference between structural and magnetic scattering and is clearly observed in the metallic $Re_{1-x}Sr_xMnO_3$, at $x = 0.4$, with Re being, La, Pr, Nd [4], and in $La_{1-x}Sr_xMn_{1-z}Al_zO_3$, at $x = 0.3$, varying z [3]. This 'interference' is beyond Boltzmann theory. With $a_0 \sim 4$Å, ρ_{Mott} would be ~ 5 mΩcm in the manganites. For the 'disordered' LaSr family, as ρ_0/ρ_{Mott} varies from $0.005 - 0.04$ with increasing disorder, the corresponding

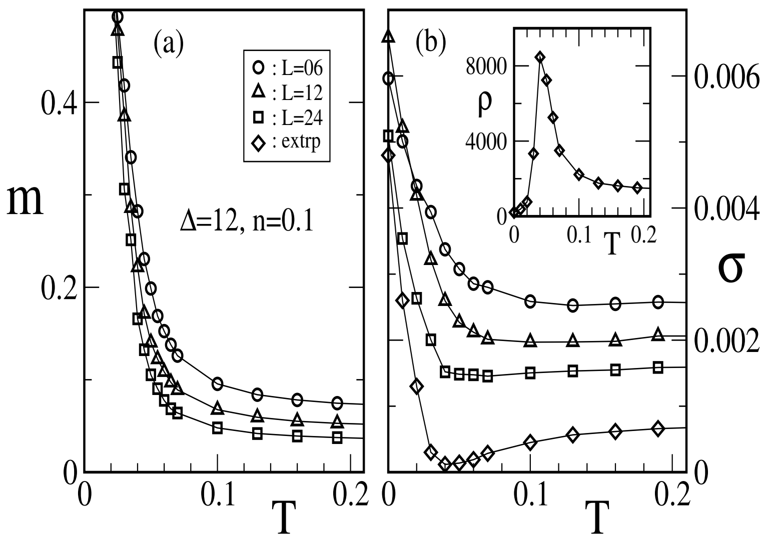

Figure 5.7: size dependence of (a) the magnetisation and (b) the conductivity. Inset shows the $\rho(T)$ obtained from the $L \rightarrow \infty$extrapolation of the conductivity.

ρ_{inf}/ρ_{Mott} increases from $0.4 - 1.5$ [3, 4].

Fig.6.(a) shows the normalised resistivity $\delta\rho(T) = (\rho(T) - \rho(0))/(\rho(0.4) - \rho(0))$ for $\Delta = 0, 2, 6$. The shift in T_c in this disorder regime is quite small, but $\delta\rho(T/T_c)$ quickly changes character with increasing disorder. The more prominent short range spin fluctuations in the disordered system couple to the diffusive electrons leading to a sharper rise in $\rho(T)$. While most of the rise in the 'clean' system occurs in the vicinity of T_c, the rise is spread over a wide interval in the disordered system.

Fig.6.(c). shows data at $n = 0.1$ and $\Delta = 12$ to illustrate the FM-PI transition. We work with this lower density because the MIT is easier to access. We solve the full problem for sizes $6 \times 6 \times L$, with $L = \{6, 12, 24\}$, disorder average, and extrapolate the computed 'd.c conductivity' to $L \rightarrow \infty$. This is crucial to capture 'Anderson localisation' in finite systems. The transport in the insulating phase is controlled by activation to the mobility edge. The detailed size dependence from which we infer the finite temperature 'Anderson transition' (more a crossover) is shown in Fig.7.

The correlation between T_c and residual resistivity has been experimentally explored [1, 2] and Fig.6.(d) highlights the fall in T_c as ρ_0 heads towards the Mott limit.

Our results on MR, Fig.6.(e), indicate that in the intermediate disorder regime the MR is actually *smaller* in the disordered problem than in the clean system. The MR is $1 - \rho(T, h)/\rho(T, 0)$. The minimum $\rho(T, h)$ is limited by ρ_0, the residual resistivity. With increasing Δ, ρ_0 grows, limiting the MR. The MR rises again only when Δ is large enough to drive a finite temperature FM-PI transition.

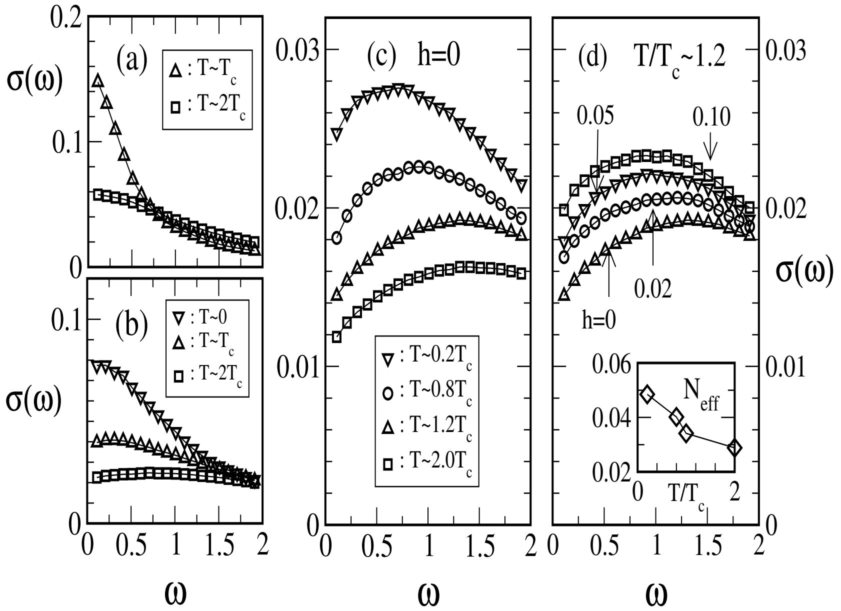

Figure 5.8: Optical conductivity at $n = 0.3$. (a). $\Delta = 0$, (b). $\Delta = 4$, (c). $\Delta = 6$, at $h = 0$, and (d). $\Delta = 6$ at $T \sim T_c$. Other parameters indicated in the figure. Inset in panel (d) shows the integrated spectral weight, $N_{eff}(T)$, (see text) derived from the data in panel (c). Data averaged over $4 - 8$ realisations of disorder.

5.3.6 Optical response

The optical response of the system, at $n = 0.3$ and $\Delta = 0, 4$ and 6, is shown in Fig.8. Panel (a). shows $\sigma(\omega)$ at $\Delta = 0$ and the Drude feature survives even for $T \sim 2T_c$ with $\sigma_{dc} \sim 6\sigma_{Mott}$. For $\Delta = 4$, however, panel (b). reveals that $\sigma(\omega)$ changes from a Drude form for $T \lesssim T_c$ to an essentially 'flat' incoherent response at $T \sim 2T_c$. At $2T_c$, $\sigma_{dc} \sim 2\sigma_{Mott}$. This response is roughly like $La_{1-x}Sr_xMnO_3$ at $x \sim 0.4$ [4]. At even larger disorder, $\Delta = 6$, the response is non Drude *even down to* $T = 0.2T_c$, and becomes markedly so, with a finite ω peak, as T is increased. The apparently $\sqrt{\omega}$ rise results from the intimate coupling of the diffusive electrons to spin fluctuations via the hopping modulation. For $\Delta = 6$, $\sigma_{dc} \sim 2\sigma_{Mott}$ at $T = 0$, and $\sigma_{dc} \sim \sigma_{Mott}$ at $T \sim 2T_c$. This is like the response in $(Pr,Nd)_{1-x}Sr_xMnO_3$ at $x \sim 0.4$ [4]. We predict that the response will be similar at $x = 0.4$ in $La_{1-x}Sr_xMn_{1-z}Al_zO_3$ at $z \sim 1\% - 2\%$. The inset to panel (d). shows the integrated low frequency spectral weight $N_{eff}(\omega', T) = \int_0^{\omega'} \sigma(\omega, T)d\omega$, at $\omega' = 2$. There is a 40% loss in spectral weight in the T range $0 - 2T_c$. Our energy cutoff in N_{eff} roughly corresponds to $\omega' \sim 0.3$eV in the manganites. Panel (d). shows the magneto-optical response at $\Delta = 6$ and $T \sim 1.2T_c$.

The non Drude relaxation with $\sigma(\omega)$ having a finite ω peak occurs in a regime where $d\rho/dT > 0$, as in conventional metals, but the charge dynamics is highly diffusive as expected in a system with strong 'effective disorder'. The change from 'coherent' to 'incoherent' dynamics occurs in $\sigma(\omega, T)$ when $\rho_{dc}(T) \sim \rho_{Mott}$. This general feature is true of the PM phase of all the manganites.

5.4 Conclusions

In this chapter we have discussed an essentially exact solution for double exchange model in the presence of arbitrary substitutional disorder. Our benchmarks indicate that the SCR approximation to the DDE model works excellently at strong disorder. Using this as our annealing strategy, and the transport calculation methodology evolved by us, we have studied (i) the inhomogeneous magnetism and spatial variations in the system, (ii) the variation of ferromagnetic T_c with disorder, (iii) the detailed transport properties, including the thermally driven Anderson transition, and (iv) the coherent to incoherent crossover in the optical response with increasing temperature. We believe this is one of the few complete solutions of a strong disorder strong coupling problem available in the literature.

Bibliography

[1] J. M. D. Coey *et al.*, Phys. Rev. Lett. **75**, 3910 (1995).

[2] L. M. Rodriguez-Martinez and J. P. Attfield, Phys. Rev. **B 54**, 15622 (1996).

[3] Y. Sawaki *et al.*, Phys. Rev. **B 61**, 11588 (2000).

[4] E. Saitoh, *et al.*, Phys. Rev. B **60**, 10362 (1999).

[5] K. Takenaka *et al.*, Phys. Rev. **B 65**,

[6] T. Kaneyoshi, *Introduction to Amorphous Ferromagnets*, World Scientific, Singapore (1992).

[7] Sanjeev Kumar and Pinaki Majumdar, Europhys. Lett. **65**, 75 (2004).

[8] E. E. Narimanov and C. M. Varma, Phys. Rev. **B 65**, 024429-1 (2001).

[9] B. M. Letfulov and J. K. Freericks, Phys. Rev. B **64**, 174409 (2001).

[10] M. Auslender and E. Kogan, Phys. Rev. B **65**, 012408 (2001).

[11] Y. Motome and N. Furukawa, J. Phys. Chem. Solids, **63**, 1357 (2002).

[12] L. Sheng, *et al.*, Phys. Rev. Lett. **79**, 1710 (1997).

[13] Some algorithms allow larger sizes: J. L. Alonso *et al.*, Nucl. Phys. **B 596**, 587 (2001); Y. Motome and N. Furukawa, cond-mat 0305029.

[14] S. Kumar and P. Majumdar, cond-mat 0305345.

Chapter 6

Nanoscale Phase Coexistence

Chapter Summary: This chapter discusses the nanoscale phase coexistence of ferromagnetic metallic (FMM) and antiferromagnetic insulating (AFI) regions in a two dimensional system by including the effect of AF superexchange and weak disorder in the double exchange model. We solve this problem using the SCR scheme and uncover a window of phase coexistence. We study the cluster pattern for varying electron density, disorder, and temperature. We also track the magnetic structure, obtain the density of states, with its 'pseudogap' features, compute the transport properties in this strongly inhomogeneous system, and demonstrate a singular low field response. Our results are probably the first fully microscopic estimate of the resistivity in the phase coexistence regime. Some of the results here appear in our paper Phys. Rev. Lett. **92**, 126602 (2004).

6.1 Introduction

The issue of multiphase coexistence in transition metal oxides has been brought to the fore [1, 2] by a set of remarkable recent experiments [3, 4, 5, 6] on the manganites These experiments probe the atomic scale magnetic correlations, structural features, or 'conducting' properties, *i.e* tunneling density of states, through local spectroscopy. The bulk thermodynamic and transport properties of these systems, including the 'colossal magnetoresistance' (CMR) seem to have a correlation with the physics of electronic phase coexistence as visualised in these nanoscale experiments.

Establishing a *first principles theoretical connection* between cluster coexistence and 'anomalous' transport, however, has been difficult. Only real space Monte Carlo (MC) techniques [7] allow access to the cluster phase, and accessible sizes are too small to study transport or quantify the effect of disorder. The approach in current use [8] is phenomenological, using classical resistor networks to model the data within a 'percolation scenario'. While 'percolation' probably plays an important role in transport, *standard* percolation theory [9] is inadequate [10] to explain the data. More fundamentally, such an approach does not explain the temperature and field dependent resistance of the 'building blocks', or correlations and hysteresis in the cluster distribution, or the dependence of bulk resistance on 'spin overlap' between clusters. In this chapter we address these questions within a 'spin-fermion' model employing the SCR approach to the DE model, studying coexistence effects in two dimensional (2d) systems upto $\sim 32 \times 32$. This allows us to probe the regime $L_S \gg \bar{L}_c \gg a_0$, where L_S, $\bar{L}_c$ and a_0 are system size, typical cluster size, and lattice spacing, respectively. We study the coexistence regime, obtain the typical cluster size, and calculate the spectral density and

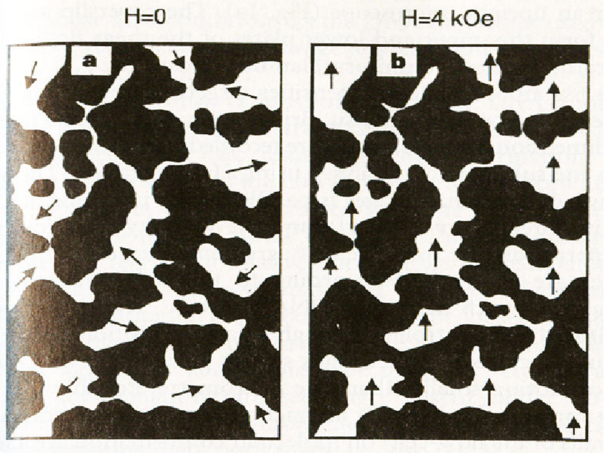

Figure 6.1: Schematic illustration of sub-micrometer scale coexistence of charge ordered insulating (dark area) and ferromagnetic metallic (white area) domains. The typical size of the domains is $0.5\mu m$. (a) At zero field the magnetisations of ferro domains are random, but all domains can be aligned by applying a field of order 4 KOe. The figure above is from M. Uehara *et al.*, Nature **399**, 560 (1999).

conductivity in the mixed phase. Our results are probably the first to clarify the connection between nanoscale phase coexistence and transport in a fully quantum mechanical itinerant electron problem.

6.1.1 Scenario

The coexistence of two phases with distinct electronic, magnetic, and possibly structural, properties is best conceived at $T = 0$ in a *clean system*. For a specified chemical potential, μ, the ground state configuration of the spin and lattice variables, $\{X_i\}$ say, assumed classical, is determined by $\delta\mathcal{E}/\delta X_i = 0$, where $\mathcal{E}\{X_i;\mu\}$ is the energy of the system in the $\{X_i\}$ background. The minimum, $\mathcal{E}_{min}(\mu)$, usually occurs for a unique $\{X_i\}$ at each μ, and in this background the electron density $n(\mu)$ is also unique. However, in the presence of competing interactions, two *distinct* $\{X_i\}$ configurations could be degenerate minima of $\mathcal{E}$ at some μ. The corresponding $\mu = \mu_c$ marks a *first order phase boundary*, and the two 'endpoint' densities, n_1 and n_2 bracket a region of coexistence. There is no homogeneous phase with density between n_1 and n_2. In this regime the system breaks up into two macroscopic domains, with density n_1 and n_2.

The effect of disorder is to convert this regime of macroscopic phase separation to mesoscale or nanoscale cluster coexistence of the two phases. Cluster coexistence can lead to an insulator-metal transition (IMT) when the ferromagnetic 'metallic' clusters percolate, generating a conducting pathway through the system. Conversely, with increasing temperature, the ferromagnetic clusters can fragment due to spin disorder, leading to a rapid rise in resistance due to disruption of the conducting backbone. An applied field can also have a remarkable effect in the poorly conducting low temperature phase, if the system is near the critical density for the IMT. The magnetic field can polarise the large but 'uncorrelated' cluster moments, enhance inter cluster tunneling in these half-metallic systems, and enormously enhance the conductance. This is believed to be the origin of the large low field magnetoresistance (MR) in the low T_c manganites. Overall, there is a fascinating variety of IMT's driven by varying density, temperature, or applying a magnetic field. The 'real' model of manganites involve coupled electronic, spin, lattice and orbital degrees of freedom, but the essence of phase coexistence and the insulator-metal transitions described above can be accessed even in a simple model of coupled electronic and spin degrees of freedom.

6.1.2 Microscopic approach

While the cluster coexistence scenario is attractive and plausible, and provides a conceptual framework for analysing the transport data, first principles calculations on the underlying disordered interacting models have proved to be rather difficult. Even assuming that the spin (or phonon) degrees of freedom that couple to the electrons can be treated classically, the 'real space' approach required in this inhomogeneous problem requires computational effort that rapidly scales with system size, with N limited to ~ 100. Results on such systems, mostly in two dimension, suggest the validity of the coexistence argument, in terms of the emerging spatial structures, but cannot quantify the effect of disorder on the cluster distribution. More seriously, given the large finite size gaps in small lattices, it is impossible to access the d.c conductivity and analyse metal-insulator transitions.

Due to the difficulty in accessing transport properties from microscopic calculations, there have been attempts to construct a 'resistor network' theory, replacing the coexisting clusters by 'metallic' or 'insulating' resistors, and computing the overall resistance of the network. The results that emerge bear some resemblance to the experimental data, but are strongly dependent on the phenomenological input for their success. The specific limitations of this approach are: (i) the 'resistance' of the network elements have to be inferred from experiments depending on the endpoint compositions in the coexistence regime, (ii) the quantum character of electron transmission between clusters, and possible quantum interference effects, are lost out in a Ohm-Kirchhoff law formulation, (iii) the sensitivity of intergrain transmission to core spin orientation (and the resulting low field MR) cannot be captured.

Since a frontal attack on the problem comes up against a computational barrier, the issues above suggest the need for controlled approximations to bridge the gap between 'exact' simulations and the phenomenology. This is where the SCR approach allows a breakthrough. We use it to solve this problem, first comparing our results in detail with exact simulations on small lattices, and then extending the study to large lattices to examine transport and spatial patterns. We provide detailed results on the spatial structures, the electronic density of states (DOS), the resistivity, and the full optical response. We also describe the evolution of these properties in response to a magnetic field, and the origin of colossal 'tunneling magnetoresistance' (TMR) in the model.

6.2 Model and method

Our model is $H = H_{el} + H_{AF} + H_{mag}$ in 2d, with:

$$H_{el} = \sum_{\langle ij\rangle,\sigma} t_{ij} c^{\dagger}_{i\sigma} c_{j\sigma} + \sum_{i} (\epsilon_i - \mu) n_i - J_H \sum_{i} \mathbf{S}_i . \vec{\sigma}_i \tag{6.1}$$

and $H_{AF} = J_S \sum_{\langle ij\rangle} \mathbf{S}_i . \mathbf{S}_j$, and $H_{mag} = -h \sum_i S_{iz}$. The hopping $t_{ij} = -t$ for nearest neighbours, and ϵ_i is a random on site potential uniformly distributed between $\pm\Delta/2$. We assume $J_H/t \to \infty$, and set the reference scale $t = 1$, We choose to work with $\Delta = 1.0$ and $J_{AF} = 0.05$, and study electronic properties for n in the vicinity of 0.1. We vary μ as needed to keep n constant. We use $|\mathbf{S}_i| = 1$. All our energies, temperature and frequency are measured in units of t.

As in the previous chapters, the limit $J_H/t \to \infty$, leads to a spinless fermion model, and the SCR approximation leads to the following effective spin Hamiltonian:

$$\begin{aligned} H_{eff}\{\mathbf{S}_i\} &= -(1/\beta)\log \mathrm{Tr} e^{-\beta(H_{el}+H_{AF})} \\ &\approx -\sum_{\langle ij \rangle} D_{ij} f_{ij} + J_S \sum_{\langle ij \rangle} \mathbf{S}_i.\mathbf{S}_j \end{aligned} \tag{6.2}$$

D_{ij} is determined self consistently as the average of $\hat{\Gamma}_{ij} = (e^{i\Phi_{ij}}\gamma_i^{\dagger}\gamma_j + h.c)$ (see chapter 3.) over the assumed equilibrium distribution.

Although the D_{ij} enter as 'nearest neighbour' exchange, they arise from a solution of the *full quantum statistical problem in the disordered finite temperature system.* In the presence of competing interactions and quenched disorder, this leads to a set of strongly inhomogeneous, spatially correlated, and temperature dependent 'exchange' D_{ij}.

We work at specified mean density, fixing μ through iteration. At consistency, fermionic properties are computed and averaged over equilibrium spin configurations. Transport properties are computed using the Kubo formula employing sizes $\sim 24 \times 24$ to 32×32 and averaged typically over 30 realisations of disorder with averaging over ~ 50 equilibrium spin configurations at each T for each realisation of $\{\epsilon_i\}$. The conductivity results are in units of $(\pi e^2)/\hbar$.

Our principal results are:

- The direct visual evidence of cluster coexistence, and dependence of cluster size on temperature, disorder and electron density.
- The temperature and disorder dependence of spectral density, recovering the pseudogap feature.
- A microscopic estimate of the resistivity, and its correlation with the spatial structures.
- The strong low field response in magnetisation and conductivity, due to alignment of 'cluster moments', inaccessible in a percolative framework.

In what follows we first discuss the benchmarking of SCR results against ED-MC for the coexistence problem and then present our results, first at zero field and then in the presence of a magnetic field.

6.3 Benchmarking H_{eff} against ED-MC

Let us start with the validity of our effective Hamiltonian, and its ability to capture the correct physics at coexistence. Since the parameter space is large, the checks are focused on $n = 0.1$ and $\Delta = 1.0$, tracking results across disorder realisations and with varying temperature.

Fig.2 compares the variation of carrier density with chemical potential obtained within the two schemes at low temperature. The discontinuity at $\Delta = 0$, between the undoped AF state and the ferromagnetic metal signifies a first order transition, and the instability of homogeneous phases for $0 < n \lesssim 0.25$. There is only a slight difference in the 'critical' μ at which the transition occurs, obtained within the two schemes. Disorder $\Delta = 1.0$ smears

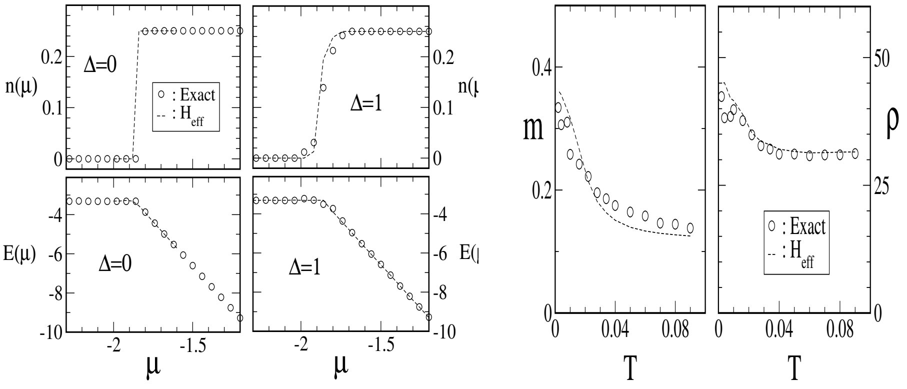

Figure 6.2: Comparing thermodynamic and transport results between ED-MC and H_{eff}. on 8×8 lattice. Symbols for ED-MC results and dashed lines for H_{eff}

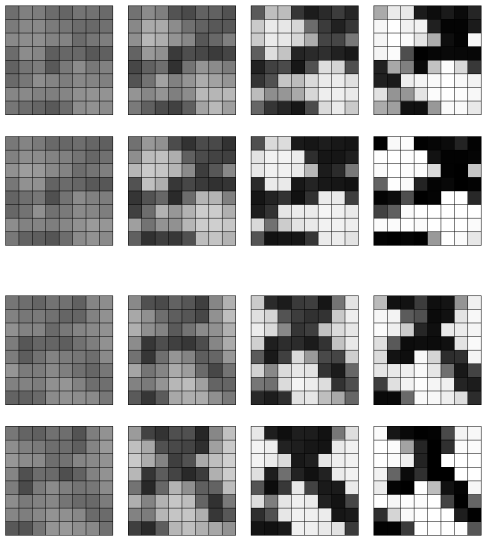

Figure 6.3: Comparing cluster patterns in ED-MC with H_{eff} for two different realisations of disorder.Temperature values along a row are $T = 2T_c, T_c^+, T_c^-$ and $0.1T_c$

out the discontinuity (on these small lattices) and 'allows' stable mean densities between $n = [0, 0.25]$. The disorder averaged $n - \mu$ data is almost identical between ED+MC and H_{eff}.

The 'density field' which emerges is of course *not* homogeneous and involves coexisting regions of FMM and AFI. While the detailed cluster pattern and correlation length can only be studied by using H_{eff} on large lattices, we want to emphasize the ability of H_{eff} to capture the *same spatially resolved patterns* as ED-MC for a specific realisation of $\{\epsilon_i\}$.

In Fig.3 we show the 'cluster pattern', as encoded in the nearest neighbour spin correlation, for both H_{eff} and ED-MC for two realisations of disorder. The first pair of rows belong to one realisation of $\{\epsilon_i\}$ and the next pair to another. Within a pair, the top row tracks the result with ED, the bottom row with H_{eff}. Temperature varies along the row, from $\sim 2T_c$ to $T = 0$ (left to right). As the results indicate both schemes lead to the same 'fingerprint' of the underlying disorder. Careful scrutiny reveals that H_{eff} slightly overestimates the local ferromagnetic tendency (dark patches), something we have noticed in the clean DE model as well. The basic reason that H_{eff} reproduces such detailed features faithfully is that it actually solves the same Schrodinger equation as ED-MC, albeit fewer times, in the same disordered background.

Now the transport, fig.2. extreme right. We discuss the transport calculation method further on, for the moment we note that our resistivity is the inverse of the (thermal and disorder averaged) optical conductivity $\sigma(\omega)$ at the scale of mean level spacing in the system ($\omega = \omega_L = \alpha W/L^2, W = 8t, \alpha \sim 5$). The 'resistivity' so computed is compared between ED-MC and H_{eff} in the next figure. We also show the associated magnetisation.

There are two features to note: (i) transport properties match reasonably between the two schemes, and (ii) the small size (and hence large ω_L) 'resistivity' *does not show the crucial turnaround feature* that would signify low temperature metallicity (and shows up only on larger systems). It is crucial to break the size barrier and access transport at lower frequency.

6.4 Results at zero field

Having established the credibility of the SCR scheme in this context we now discuss results obtained using this method on large lattices, $\sim 24 \times 24$ to 32×32.

At low electron density, the competetion in the DE+SE model is between a $\{\pi, \pi\}$ AF phase and a ferromagnet (FM). We set $J_S = 0.05$ and scanned in μ to locate the μ_c for the first order boundary. The density changes from $n = 0$ to $n \sim 0.20$ at the discontinuity. Moderate disorder smooths out the discontinuity in $n(\mu)$ converting it to a sharp crossover.

We fixed $J_S = 0.05$ and probed the coexistence regime, $n \sim 0 - 0.2$, with varying electron density, temperature (T), and $\Delta = 0.2$ and $\Delta = 1.0$. All the results are obtained by cooling the system from the high T paramagnetic, approximately homogeneous, phase.

6.4.1 Spatial structures and cluster size

The two panels in Fig.4 show the thermally averaged nearest-neighbour spin correlation. The mean density n in these figures vary from $0.06 - 0.15$ from the top row to bottom the row in each panel, straddling the coexistence region, the disorder is $\Delta = 0.2$ (left panels) and $\Delta = 1.0$, (right panels), and the data is obtained in a cooling sequence. Along each row the temperature varies as $T = 2T_c, 1.2T_c, 0.8T_c, 0.1T_c$ for both panels, as one moves from left to right.

The figure provides direct visual evidence of 'clustering'. At fixed density and temperature, the cluster pattern for stronger disorder ($\Delta = 1.0$) is more fragmented than for $\Delta = 0.2$.

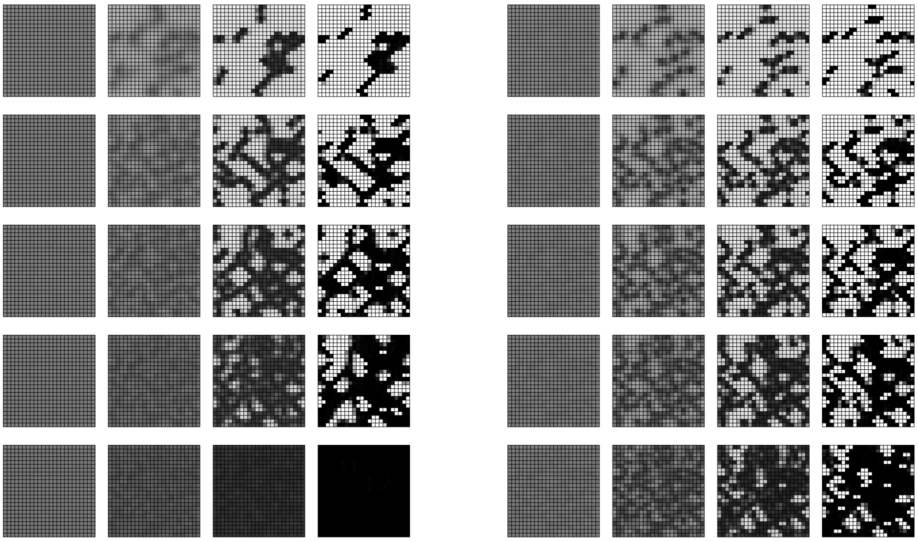

Figure 6.4: Cluster pattern with varying density, temperature and disorder. Left Panel: $\Delta = 0.2$, Right Panel: $\Delta = 1.0$. Electron density $n = 0.06, 0.08, 0.10, 0.12 and 0.15$ from top to bottom and temperatures $T = 2T_c, T_c^+, T_c^-$ and $0.1T_c$ from left to right in each panel.

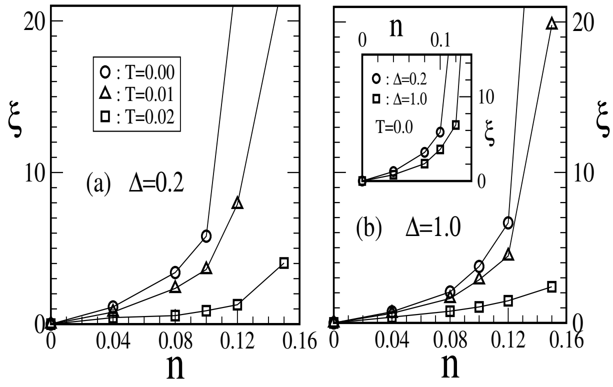

Figure 6.5: Ferromagnetic correlation length inferred by fitting Lorentzians through the spin structure factor data.

The contrast reduces with increasing T, as the spins in the AF regions fluctuate out of antiparallel alignment.The large density regions sustain a finite local magnetisation whereas, the empty regions give rise to local AFM.

Fig.5. shows the typical size of FMM clusters, inferred from a Lorentzian fit to the magnetic structure factor, *i.e*, $S_{\mathbf{q}} \sim (q^2 + \xi^{-2})^{-1}$. The resulting correlation length depends on n, Δ and T, decreasing with increasing disorder and T, and increasing with increasing density. The main panels, (a) and (b), highlight the n dependence at different T and Δ, while the inset replots the same data to highlight the dependence on disorder. To completely understand the variation of cluster sizes with temperature, density and disorder one would have to solve the problem on even larger lattices.The dependences, overall, are intuitive, and correlate well with the transport data that we discuss further on.

6.4.2 Magnetic properties

Fig.6 shows the magnetisation, $m(T)$, and the AF peak in the magnetic structure factor $S_{\mathbf{q}}$ at $\mathbf{q} = \{\pi, \pi\}$ to illustrate the evolution from the AF to the FM phase with increasing n. Panel $(a) - (b)$ are at $\Delta = 0.2$ and panel $(c) - (d)$ at $\Delta = 1.0$. The 'extremal' densities are either strongly AF or FM, while for $n \sim 0.08 - 0.12$ *both FM and AF reflections have finite weight*. Panel (e) tracks the 'characteristic temperature', $T_{ch}(n, \Delta)$, identified from the maximum in $\partial^2 O/\partial T^2$ where O is the appropriate order parameter (of the FM or AF phase). In the shaded region, $0.10 \lesssim n \lesssim 0.14$, it is difficult to resolve the T_{ch} accurately. Panel (f) shows the change in 'saturation magnetisation' $m(T = 0)$ with increasing n and changing disorder. The small moment regime, $m \lesssim 0.1$, for $n \lesssim 0.1$ is a 'ferro-insulator' phase, as we will discover from the transport data. In this regime the moments in different clusters are only weakly correlated. It would be very interesting to see the effect of a magnetic field on these weakly coupled FM regions. We will discuss these effects later in this chapter.

6.4.3 Spectral features

Fig.7 shows the low energy density of states (DOS) for $n = 0.1$. Even at weak disorder, panel (a), there is a 'pseudogap' in the system averaged DOS, at the lowest temperature, $T \sim 0.01$. However, the pseudogap rapidly fills up with increasing T, and the DOS tends towards the universal profile of the spin disordered 2d DE model. At stronger disorder, panel (b), the 'dip' in the DOS at μ is deeper. Due to stronger pinning, the clusters, and the gap feature, survives to higher T, and only for $T \gg T_{ch}$ tends to the asymptotic form. The actual form of this 'dip' feature in the DOS can be different in the real systems due to the electron-electron interaction effects. While this data focuses on the system averaged DOS, which can be probed by photoemission spectroscopy (PES), it would be very interesting to compute local density of states on this system , which can be studied by tunneling spectroscopy in the experiments. Since the finite density regions have the DE mechanism operative, the local density of states there should be metallic. The empty regions would show a gap in the local DOS.

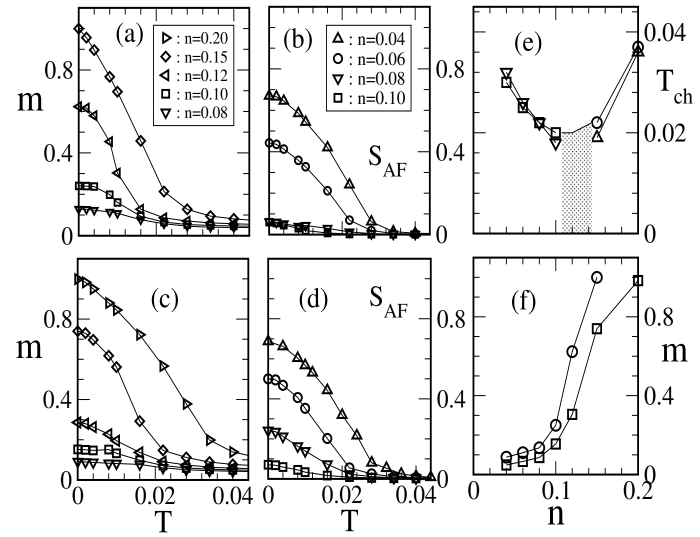

Figure 6.6: Magnetisation, $m(T)$, and structure factor, $S_{\mathbf{q}}(T)$ at $\mathbf{q} = \{\pi, \pi\}$. Panel $(a)-(b)$: data for $\Delta = 0.2$, panel $(c) - (d)$: data for $\Delta = 1.0$. The legends are common to panels $(a) - (d)$. Panel (e): The characteristic temperature (see text), $T_{ch}(n, \Delta)$: triangle down: AF at $\Delta = 1.0$, square: AF at $\Delta = 0.2$, triangle up: FM at $\Delta = 1.0$, circles: FM at $\Delta = 0.2$. Panel (f): $m(T = 0)$ with varying n, circles: $\Delta = 0.2$, squares: $\Delta = 1.0$. System size: 24 × 24.

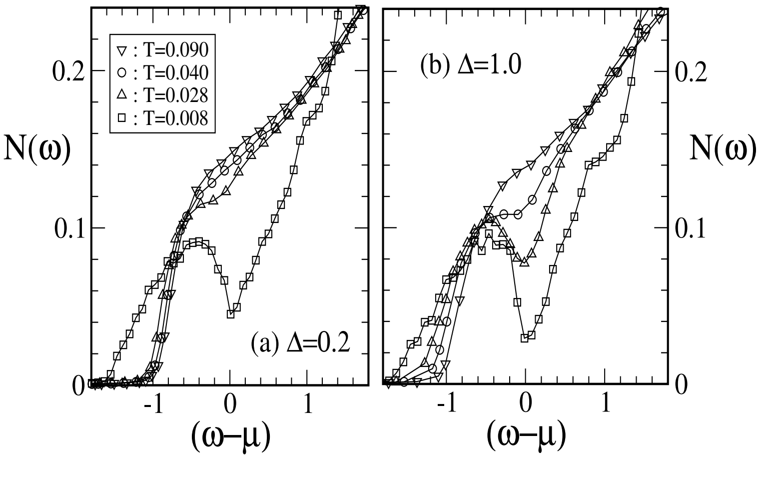

Figure 6.7: Low energy density of states, at $n = 0.10$. Panel (a): data at $\Delta = 0.2$, panel (b): data at $\Delta = 1.0$. The DOS is plotted with respect to $\omega - \mu(T)$, incorporating the T dependent shift in μ. Lorentzian broadening of δ functions to 0.03. Data averaged over 30 copies.

6.4.4 Results on Transport

Fig.8 shows resistivity, $\rho(T)$, with varying n and disorder. The comparison of panel (a), $\Delta = 0.2$, and panel (b), $\Delta = 1.0$, indicates that $\rho(T)$ for stronger disorder is systematically larger. The *trends*, however, are similar in the two cases and allows a tentative classification of the 'global' aspects of transport. At both $\Delta = 0.2$ and $\Delta = 1.0$ there is a critical density, $n_c(\Delta)$, below which $\rho(T = 0)$ diverges, indicating the absence of any connected 'conducting path'. The inset to panel (b) shows the trend in the $T = 0$ conductivity with increasing FM cluster area, a_{FM}.

We suggest the following qualitative picture of transport in the coexistence regime based on the data in Fig.8.

- At low T, and for $n > n_c(\Delta)$, there is, by definition, some connected 'metallic path' through the sample. It is reasonable to assume that at least in this connected region the spins are aligned due to DE. Since cluster dimension and electron wavelength are comparable in our system a large fraction of the resistance arises from the non trivial geometry of the current path. This scattering is quantum mechanical, and the low T metallic phase corresponds to a *quantum percolative regime* [13], for roughly $0.15 \gtrsim n \gtrsim 0.08$ at $\Delta = 1.0$.

- With increasing T, the resistance of the conducting network increases due to DE spin fluctuations and, till the network is disrupted, there is a regime $d\rho/dT > 0$. This 'metallic' behaviour occurs despite the very large residual resistivity. This is a regime of *weak magnetic scattering on the conducting network.* If $n \gg n_c$, *e.g*, $n = 0.20$ in Fig.8.(b), so that inhomogeneities are weak, $\rho(T)$ will smoothly increase to the $T \gg T_{ch}$ asymptotic value.

- With further increase in T, in the $n \gtrsim n_c$ regime, the spin disorder can destroy some of the 'weak links', disrupting the conducting network and leading to a sharp increase in $\rho(T)$ see, *e.g*, $n = 0.1$ in Fig.8.(b). This correlates well with reduction in typical cluster size with increasing T, discussed in the next paragraph. Depending on n and the extent of disorder (and system size, in a simulation) there could be a rapid rise or a 'first order' metal-insulator transition (MIT). This is *spin disorder induced breakup of clusters driving a MIT.*

- Beyond this 'MIT' the conduction is through the 'insulating' regions, with isolated patches contributing to nominally activated transport, as visible in Fig.8.(b) for $n \lesssim 0.12$. For $T \gg T_{ch}$, as the structures disappear, Fig.2, and the system becomes homogeneous, $\rho(T)$ is dominated by spin disorder scattering. This is a *diffusive regime with saturated spin disorder scattering*, visible for $T \gtrsim 0.08$ at all densities.

- For $n < n_c$, the regime of low density isolated clusters, $\rho(T)$ falls monotonically, and the response is typical of *low density ferromagnetic polarons in a AF background.* This occurs for $n \lesssim 0.08$ at $\Delta = 1.0$, and at lower n at $\Delta = 0.20$.

The variation in the FMM cluster size, discussed earlier, is broadly consistent with the above description and strengthens the proposed transport scenario.

Controls in transport calculation

Since the present problem involves transport calculation in a complex two dimensional system, let us discuss the checks that we have made.

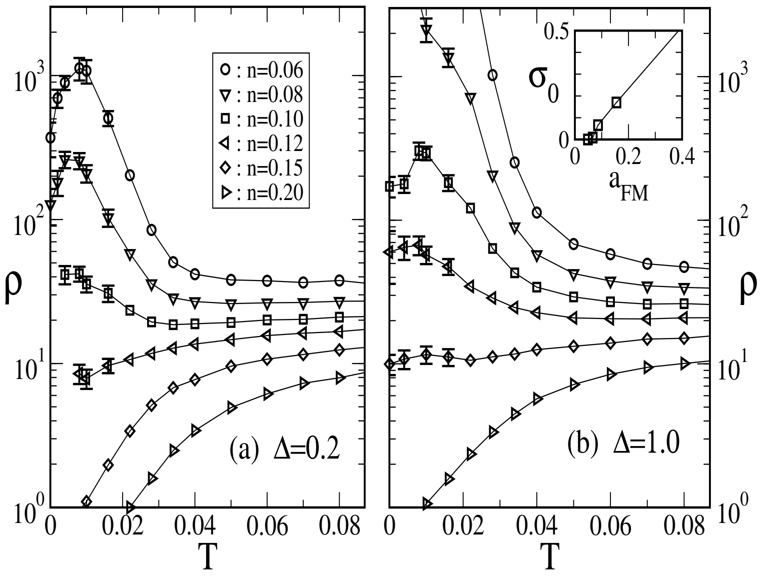

Figure 6.8: Resistivity, $\rho(T)$, with varying n. Panel (a): $\Delta = 0.2$, panel (b): $\Delta = 1.0$. Results obtained on 'cooling'. System size 24×24, data obtained by inverting the 'mean conductivity'. Average over $20-50$ copies of $\{\epsilon_i\}$ (error bars comparable to symbol size, unless otherwise indicated). Results on size 32×32 are similar. Inset, panel (b): Normalised $T = 0$ conductivity, at $\Delta = 1$, -vs- FMM surface area.

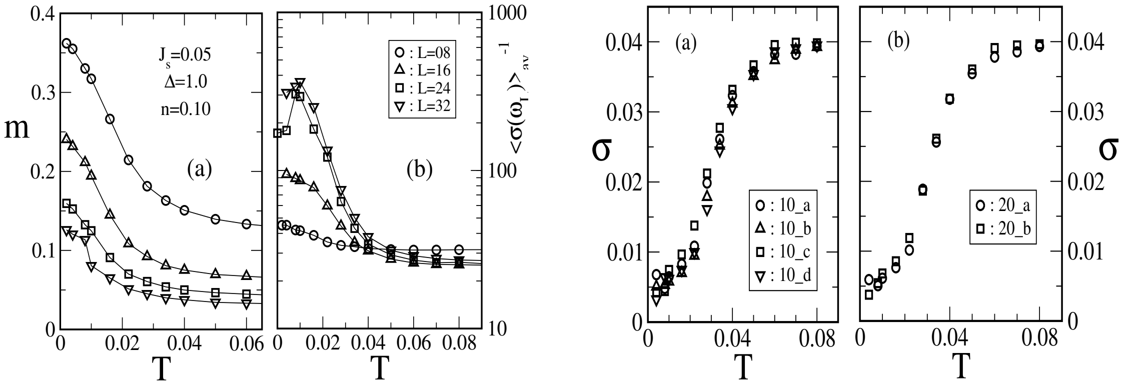

Figure 6.9: Left panels: Size dependence of (a) the magnetisation (b) the conductivity. Right panels: Disorder averaged conductivity for (a) the four independent sets of 10 disorder copies each (b) two independent sets of 20 disorder copies each.

Kubo formula based calculation are known to be numerically difficult due to the discrete spectrum of any finite system. This implies that the conductivity cannot be reliably computed below a scale comparable to the typical finite size gap in a system. This gap, Δ_L, is roughly W/L^2 in a 2d system, with W being the bare bandwidth and L the linear dimension of the system. This immediately indicates that the true 'd.c conductivity' cannot be computed in a finite system, and we can only hope to compute the finite frequency ('optical') conductivity at a frequency $\omega \sim \Delta_L$. Given this complication, and the need for disorder averaging in this strongly inhomogeneous system, we focus on the qualitative stability of our results with respect to size variation and disorder average.

Let us recapitulate the arguments put forward in chapter 2. The d.c conductivity involves matrix elements between essentially degenerate states and cannot be directly computed on a finite system due to the finite size gaps in the spectrum. However, the *optical conductivity* can be computed down to frequencies comparable to the finite size gap ($\sim W/L^2$, $W = 8t$ in our case). To be on the safe side we use $\omega_L = 5W/L^2$. At $L = 8$ this is $\omega = 0.625t$, which is quite large, while at $L = 32$ this allows us to access $\omega = 0.04t$.

Our results are averaged over 30 copies of disorder, which typically would not be enough if this were purely a quenched disorder system. However, for each of these thirty copies *there is thermal average over 50 equilibrium spin configurations at each temperature*, so the effective averaging is more extensive than simple disorder average implies. We check the adequacy of averaging the following way.

The resistivity, ρ, defined by us, arises from:

$$\rho^{-1} = \frac{1}{N_{dis}} \sum_{dis} \{ \frac{1}{N_{sp}} \sum_{sp} \sigma(\omega_L; \mathbf{S}, \epsilon_i) \}$$

The N_{sp} indicates internal thermal average over spin configurations ($\mathbf{S}$), while the N_{dis} is for averaging over realisations of quenched disorder (ϵ_i). The resistivity is calculated as the *inverse of the thermal and disorder averaged optical response at* $\omega = \omega_L$. Fig.9. right panels shows $\sigma(\omega_L, T)$ itself, rather than the inverse. Right panel(a) shows data over four sets of 10 copies each (of ϵ_i) and except at the lowest temperature the 10 copy averages look like one another. Right panel(b) plots the 20 + 20 data and even the low T correspondence improves.

Now the size dependence. Increasing L allows us to access progressively lower frequency in $\sigma(\omega)$, so that at large enough L the $\sigma(\omega_L)$ obtained is representative of $\sigma(0)$. The left panels in fig.9. tracks the magnetisation (left (a)) and 'resistivity' (left(b)) as a function of T with increasing L^2. While there is significant variation in $\langle\sigma\rangle^{-1}$ between the smaller sizes, the variation is much weaker between $L = 24$ and $L = 32$. It is possible that in the present model, the $L \rightarrow \infty$ system would be localised at any disorder, whatever be the pattern of percolating metallic paths. Even if that were true (and confirming that would require computational effort beyond present resources) the qualitative lessons regarding transport at cluster coexistence would still be valid, and physically relevant in the 3d context.

The ferromagnetism, left panel(a), weakens with increasing L because of partial cancellation between differently oriented moments in weakly connected clusters. However, by the time $L = 24$ the response is reasonably stable.

6.5 Response to a magnetic field

The effect of a magnetic field and temperature can be studied through a host of physical indicators, *e.g*, the density-density correlation function $D_{nn}(\mathbf{q})$, the spin-spin correlation function $D_{ss}(\mathbf{q})$, the density of states at Fermi level $N(\epsilon_F)$, the magnetisation $m(h, T)$ and of course the resistivity $\rho(h, T)$.

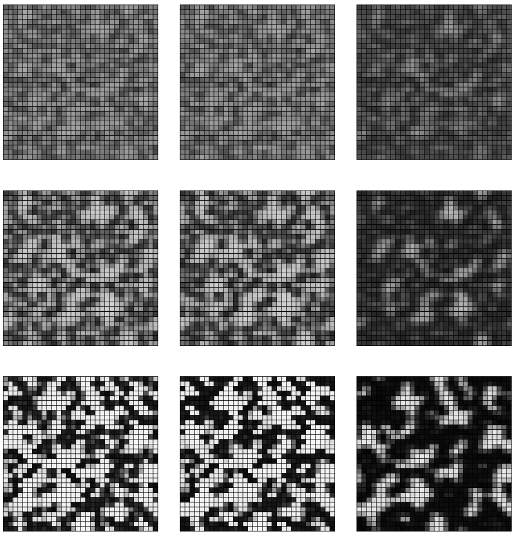

Figure 6.10: Nearest neighbour spin correlation $f_2^s = \langle \mathbf{S}_i.\mathbf{S}_{1+\delta} \rangle$ at $n = 0.1$, $\Delta = 1.0$. System size 32×32. Field variation along the row: $h = 0.0, 0.01, 0.10$, and temperature, up the column, $T = 0.06, 0.03, 0.01$.

6.5.1 Effect on spatial structures

The pattern for the nearest neighbour spin correlation $f_2^s(\mathbf{R}_i) = \langle \mathbf{S}_i.\mathbf{S}_{1+\delta} \rangle$ is shown in Fig.10 for three temperatures and for three fields, $h = 0$, $h = 0.01$ (central column) and $h = 0.10$ (right column). The first row shows the high T paramagnetic phase where f_2^s is small on all links since the thermal scale is much larger than both the exchange and field scales. It is only at at $h = 0.10$ that we see signs of magnetisation. The contrast improves with cooling (left column) but the field response is similar at the lower temperatures as well, *i.e* $h = 0$ and $h = 0.01$ are virtually indistinguishable.

For the $n = 0.1$ case at $\Delta = 1.0$, where the low T cluster pattern is rather fragmented, and the $h = 0$ magnetisation is rather low, $\lesssim 0.1$, the immediate effect of an applied field is to orient the 'cluster moments' parallel to the field. Since the clusters typically have $\gtrsim 10$ spins coupled together even a weak field have a large effect on $m(h, T)$. Although this does not change the 'local electronic structure' and $N(\epsilon_F)$ is mostly unaffected, the parallel moments allow enhanced tunneling between the FMM domains leading to large low field MR. Since the cluster pattern does not change (at low fields) the correlation length associated with D_{nn} is unaffected. Overall, the main low field effect at low T is alignment of the large 'cluster moments' in the direction of the field and a consequent increase in electron mobility.

At larger fields two other effects come into play. The FMM phase grows in volume, and residual spin disorder (due to finite temperature) within the domains gets suppressed. The system now behaves like a canonical 'clean' DE ferromagnet, with a large DOS at ϵ_F. The bulk magnetisation nears saturation.

6.5.2 Magnetism and transport

While the cluster pattern is insensitive to a weak magnetic field, both the resistivity and magnetisation respond dramatically. There is essentially a 'two stage' response to an applied

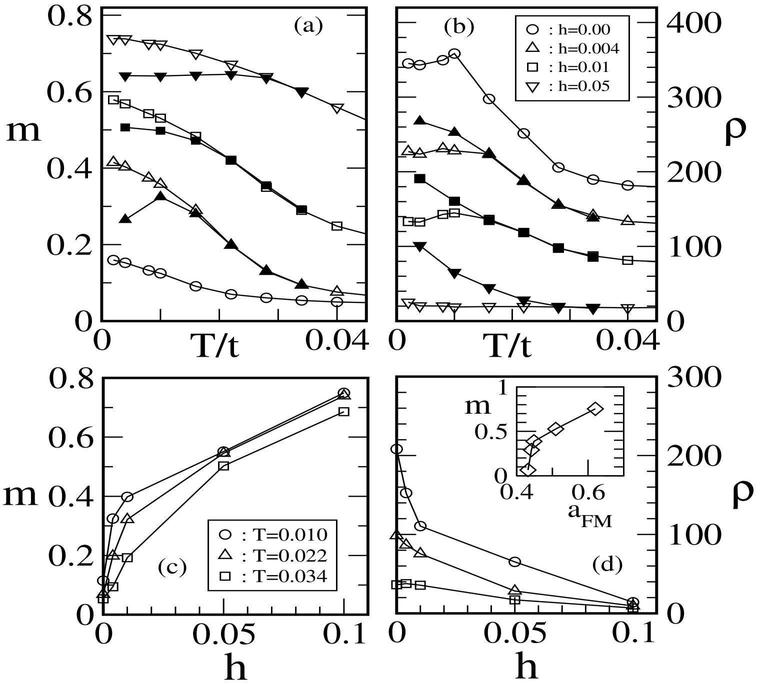

Figure 6.11: Magnetism and magnetotransport at (a), (b) constant magnetic fields and at (c), (d) constant temperatures. The inset to (d) shows the variation of magnetisation with the total area of the ferromagnetic region. $\Delta = 1.0$ and $n = 0.1$

field (particularly at low temperature) in the coexistence regime. A weak field aligns the large 'cluster moments' parallel to the field, without significantly changing the FMM volume fraction. This enhances the tunneling between FMM domains, which may have been supressed earlier due to random orientation of the cluster moments. The magnetisation rises sharply and there is an attendant sharp drop in resistivity. At larger field, the FMM volume fraction itself increases and the transport phenomena can probably be described by a volume fraction dependent percolative effect.

6.6 Connection with manganites

Our results on coexistence share several generic features with the manganites [3, 4, 5, 6], but there are key differences too. Apart from the difference between 2d and 3d, these are (i) the important regime of coexistence in manganites is between FMM and charge ordered insulator (COI), and crucially involves the Jahn-Teller (JT) phonons. This requires enlarging our model. (ii) It is supposed that the FMM and COI regions are nominally of *equal density*, which is why such domains can survive over μm scale. Our clusters are 'charged' due to the density difference between FMM and AFI. In any real system Coulomb effects [14] would have to be considered in such a case, which we plan to study separately.

6.7 Conclusions

In this chapter we have presented microscopic results on quantum transport across a regime of phase coexistence in an itinerant fermion model, and correlated it with thermal evolution of the spatial structures. This sheds light on several qualitative issues that arise in interpreting transport data and spatial structures on the manganites. A more quantitative comparison with manganite data requires inclusion of the lattice and orbital degrees of freedom, which we are currently engaged in.

Bibliography

[1] N. Mathur and P. B. Littlewood, Solid. State. Commun. **119**, 271 (2001).

[2] E. Dagotto, T. Hotta and A. Moreo, Phys. Repts. **344**, 1 (2001).

[3] L. Zhang, C. Israel, A. Biswas, R. L. Greene and A. de Lozanne, Science, **298**, 805 (2002).

[4] M. Uehara, S. Mori, C. H. Chen and S. -W. Cheong, Nature, **399**, 560 (1999).

[5] Ch. Renner, G. Aeppli, B. G. Kim, Y. Soh and S. -W. Cheong, Nature, **416**, 518 (2002).

[6] M. Fath, S. Freisem, A. A. Menovsky, Y. Tomioka, J. Aarts and J. A. Mydosh, Science, **285**, 1540 (1999).

[7] A. Moreo, M. Mayr, A. Feiguin, S. Yunoki and E. Dagotto, Phys. Rev. Lett. **84**, 5568 (2000).

[8] M. Mayr, A. Moreo, J. A. Verges, J. Arispe, A. Feiguin and E. Dagotto, Phys. Rev. Lett. **86**, 135 (2000).

[9] D. Stauffer and A. Aharony, *Introduction to Percolation Theory*, Taylor & Francis, London (1991).

[10] J. Burgy, E. Dagotto and M. Mayr, Phys. Rev. **B 67**, 014410-1 (2003).

[11] Sanjeev Kumar and Pinaki Majumdar, Phys. Rev. Lett. **92**, 126602 (2004)

[12] S. Kumar and P. Majumdar, cond-mat 0305345.

[13] A quantum 'random bond' model, with 'metallic' and 'insulating' links, in 2d, is expected to be insulating, see Y. Avishai and J. M. Luck, Phys. Rev. **B 45**, 1074 (1992), but we do not know of any exact results in the context of 'correlated bonds' as relevant here.

[14] K. Yang, Phys. Rev. **B 67**, 092201-1 (2003).

Chapter 7

Thesis Summary

In this thesis we have studied magnetism and transport in a variety of disordered interacting systems. All the models share the common feature of involving (quadratic) fermions coupled to annealed classical degrees of freedom. This 'adiabatic' approximation allows us to exploit the nominally non interacting character of the quantum problem and provide detailed solutions to a variety of models.

The adiabatic limit, however, by itself does not allow detailed solution of the correlation models that we have studied, in the absence of further approximations to break the severe finite size constraint of the standard Monte Carlo technique. We also needed a controlled method for calculating electronic response functions, *e.g* conductivity, once the annealing problem for the classical variables is solved.

In chapter 2 we formulate the linear response based conductivity calculation employing the Kubo formula, and study several transport problems involving *quenched* disorder. Our strategy involves a calculation of the integral of the low frequency optical conductivity and its systematic size dependence (and inversion) to obtain the d.c response. We tested out our method on the standard Anderson localisation problem, comparing with available results, and also obtained several new results in the context of magnetic scattering and the combined effects of structural and magnetic disorder.

Chapter 3 takes up the annealing problem for strong coupling between fermions and classical spins. We proposed a scheme for constructing classical spin Hamiltonians from Hunds coupled spin-fermion models in the limit $J_H/t \to \infty$. The strong coupling between fermions and the core spins requires self-consistent renormalisation (SCR) of the effective 'exchange' in the model, either in the presence of inhomogeneities or with increasing temperature. The method was tested out in detail against the exact Monte Carlo method, found to be accurate, and used to study magnetism and transport on large lattices in the clean DE problem.

Chapter 4 considers the "Anderson-Mott" transition in amorphous GdSi, involving coupled fermion-spin-phonon degrees of freedom in the presence of strong disorder. The material exhibits an insulator-metal transition with varying carrier density, a spin glass phase at low temperature, and colossal magnetoresistance. In addition to the unusual magnetotransport, electron-electron interactions lead to characteristic features in the density of states and conductivity close to the insulator-metal transition. We solved this strong disorder strong coupling problem by successively constructing approximate effective Hamiltonians for the spin and phonon degrees of freedom and finally solving for electronic transport in the appropriate spin-phonon background. Our calculations highlight (i) how the transport and magnetoresistance arise from the interplay of structural disorder, lattice polaron effects and electron-spin coupling, and, (ii) how the spin glass phase arises from strong randomness in the magnetic bonds, J_{ij}, due to disorder in the electron system.

Chapter 5 considers an application of the SCR scheme, involving the strongly disordered double exchange (DDE) model. The SCR scheme compares very well with ED-MC in the disordered case. We mapped out the various magnetic and transport phases of the problem, including a detailed study of the (thermal) spin disorder driven Anderson transition. We could also locate a thermally driven coherent to incoherent response in the optical response, as seen in the disordered wide bandwidth manganites. This study is probably one of the few numerically exact solutions in a disordered strongly interacting system.

Finally, chapter 6 studies the experimentally vital problem of nanoscale cluster coexistence and the associated electronic transport. A wide variety of probes have demonstrated the spatial coexistence of ferromagnetic metallic (FMM) and antiferromagnetic (charge ordered) insulating (AFI) clusters in the low T_c manganites. It is believed that the remarkable metal-insulator transition and colossal magnetoresistance in (at least) the low T_c manganites is related to phase competetion between FMM and AFI. We studied a minimal model of such phenomena, considering competing double exchange and antiferromagnetic superexchange in 2d in the presence of weak disorder. The SCR method was benchmarked in detail against ED-MC in this model, found to be accurate, and used on large lattices to clarify the spatial structures and associated transport. Our method allowed a fully microscopic estimate of the resistivity in the coexistence regime, and mapped out the various metal-insulator transitions in this model. These results are probably the most important in this thesis. We could also study the singular low field response in the model, which bears striking similarity to the huge tunneling magnetoconductance observed in the low T_c manganites.

In summary, the thesis allows some methodological advance in terms of transport in disordered systems, and magnetism in double exchange based models, and provides detailed solutions to three disordered interacting electron problems. Our more recent work, beyond this thesis, allows us to handle newer (phonon) degrees of freedom as well, allowing access to a wide range of materials issues.